Computer Simulation of Zeolites: Adsorption, Diffusion and Dealumination

---

Computer Simulaties van Zeolieten: Adsorptie, Diffusie en Dealuminering

(met een samenvatting in het Nederlands)

Proefschrift

ter verkrijging van de graad van doctor aan de Universiteit Utrecht op gezag van de rector magnificus, prof. dr. J.C. Stoof, ingevolge het besluit van het college voor promoties in het openbaar te verdedigen op maandag 2 november 2009 des middags te 12.45 uur

door

Shuai Ban

geboren op 29 juni 1980 te Henan, China.

Promotoren:	Prof. dr. J.P.J.M. van der Eerden
	Prof. dr. ir. K.P. de Jong
Co-promotor:	Dr. ir. T.J.H. Vlugt

Contents

1

Introduction

1.1 Zeolites

1.1.1 Structure

Zeolites are microporous crystalline solids with a well-defined structure. The micropores of zeolites can consist of channels or cages which may be interconnected to form a multidimensional porous system. Zeolites have the capability to selectively adsorb molecules based their size. Therefore, zeolites are also called molecular sieves. The maximum size of guest molecules that can enter the pores of a zeolite is controlled by the dimensions of the micropores.

The zeolite framework consists of connected TO_4 tetrahedra, where the T atoms are usually silicon and aluminum. The all-silica form of a zeolite has a Si/O ratio of 2 : 1 with a chemical formula $(SiO_2)_n$, and its structure is charge neutral like Quartz. However, in zeolites some of the framework Si may be replaced by trivalent Al, resulting in a net negative charge that needs to be balanced by non-framework cations such as H^+, Na^+, K^+, Ca^{2+} and Mg^{2+}.

There are several types of building units present in zeolite frameworks. The primary building unit (PBU) is the tetrahedral unit, while the secondary building units (SBU) are the molecular complexes which are formed by the PBU elements. The SBUs consist of single and double rings of tetrahedra, which can be further assembled in different types of structural units, the so-called Composite Building Units (CBU), see Fig. 1.1. The CBUs, e.g. double 6-ring, cancrinite cage, alpha cavity, are useful in characterizing similarities between framework types.

At present, over 190 different zeolite frameworks are known [1]. Among these zeolites, only a few are single crystals sufficiently large for the structural characterization using traditional crystallographic methods. In Fig. 1.2, scanning electron microscopy images shows MFI-type zeolite with a size of 50 μm, and MOR-type zeolite of 40 μm, respectively.

1.1.2 Catalytic properties

Zeolites have been widely used as active and selective catalysts in the petrochemical industry [2–9]. Zeolite activity originates from either Brønsted acid sites or active metal non-framework atoms that may be present in the zeolite [10–14]. The Brønsted proton site acts as a strong acid in zeolite catalysts. Compared to silanol groups, the acidity of the proton is much stronger (see Fig. 1.3). The concentration of the acid sites is directly related to the number of framework Al atoms. However, the acidity of the Brønsted acid sites may decrease for large Al concentrations as nearby protons may hinder the activities of each other. Zeolites can also serve as oxidation or reduction catalysts, often after small non-framework metal nanoparticles are introduced into the framework. Examples are the use of titanium containing ZSM-5 in the production of caprolactam [15], and copper containing zeolites in NO_x decomposition [16].

The selectivity of zeolites is attributed to their microporous structure, which control the accessibility of reactants and products [7, 17–20]. For molecular adsorption, the ability to preferentially adsorb certain molecules, while excluding others, has opened up a wide range of molecular sieving applications for zeolites [21–24]. In some cases, the different diffusion behavior of guest molecules

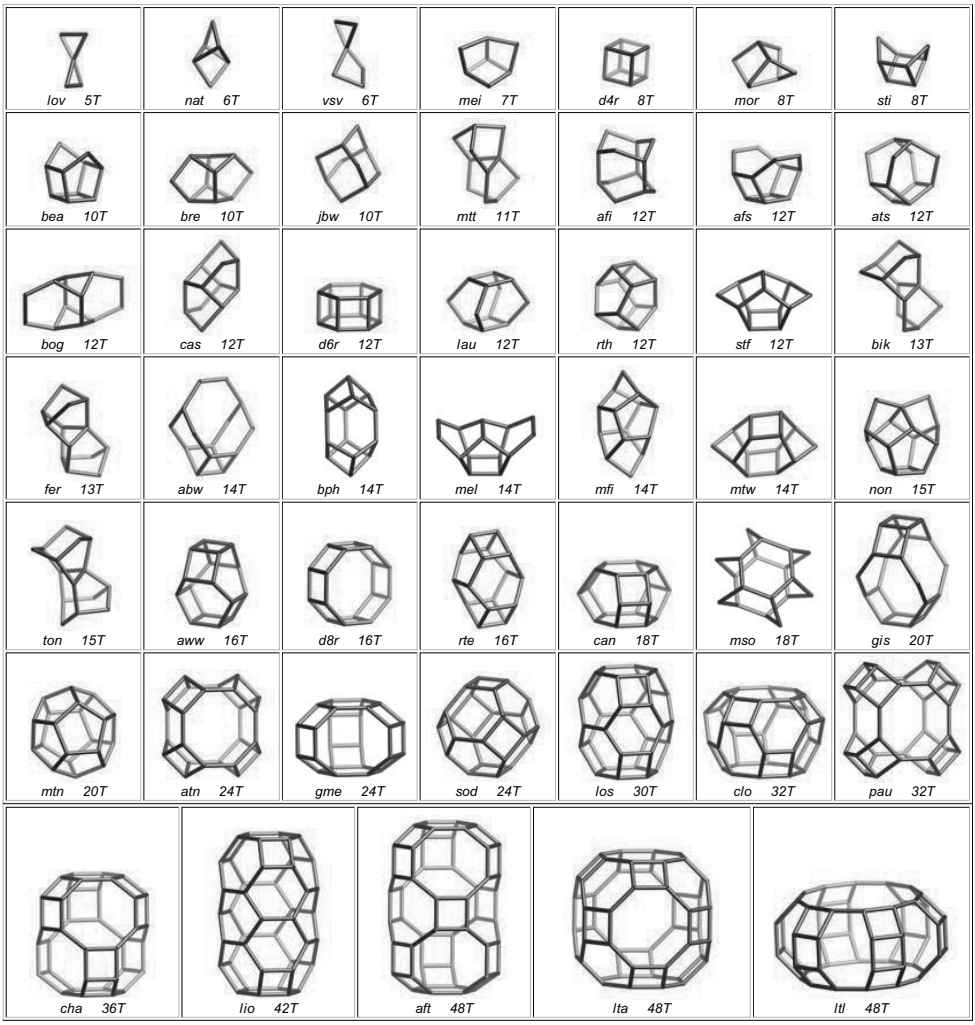

Figure 1.1: Composite Building Units (CBU) of zeolites classified by the number of T atoms in the unit. This figure is taken from the zeolite database with permission of the International Zeolite Association [1]. For each unit, an three-letter code is provided according to the definition of International Zeolite Association.

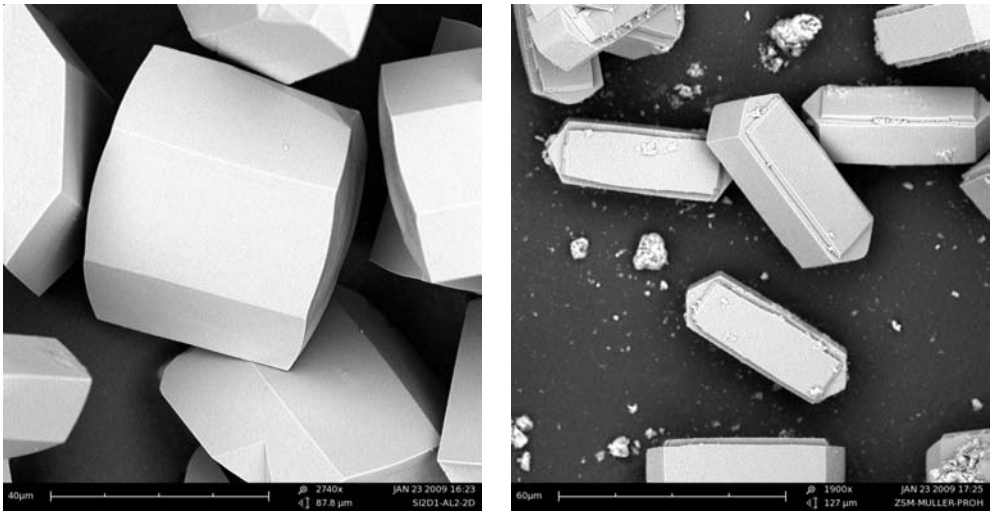

Figure 1.2: SEM images of synthetic zeolite crystals. (left) Mordenite crystals of a few μm and (right) ZSM-5 crystals. The SEM images were provided by Dr. Zhang from the group of Inorganic Chemistry and Catalysis in Utrecht University.

in a zeolite may also result in selectivity as some guest molecules diffuse much faster than others. One example is the purification of p-xylene using silicalite where the diffusion of p-xylene is faster than its isomers due to differences in the molecular size. The selectivity may also be caused by non-framework cations. Guest molecules that strongly interact with non-framework cations will have a low diffusivity. In this way, zeolites are capable of separating guest molecules according to their different interaction strength with non-framework cations. Therefore, zeolites containing non-framework cations are extensively used as desiccants due to their high affinity for water, and are also used for gas separations [25–27].

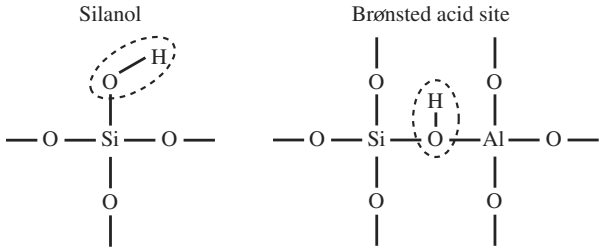

Figure 1.3: Schematic representation of silanol and Brønsted sites present in zeolite frameworks.

1.1.3 Applications

Zeolites are useful catalysts for organic reactions like cracking, isomerization and hydrocarbon synthesis [2–5]. Zeolites can promote a diverse range of catalytic reactions such as acid-base and metal induced reactions. The main industrial application areas are petroleum refining, synfuels production, and petrochemical production of organic molecules [7].

Zeolites are widely used as ion-exchangers for water purification and softening [28]. Natural zeolites are excellent ion exchangers for the removal and recovery of heavy metal cations from

drinking and waste-water [29]. This is because hydrated cations in zeolite pores can be readily exchanged with other cations present in an aqueous solution.

Zeolites have been also used in nuclear industry [30]. Zeolites are capable of efficiently removing and trapping many fission products from nuclear waste. Their alumina-silicate structure is extremely durable and resistant to radiation. Once zeolites are loaded with fission products, they can be pressed into an extremely durable ceramic form, closing the pores and trapping the waste inside a solid stone block. This greatly reduces the nuclear hazard compared to conventional reprocessing systems [31].

Natural zeolite can be used to prepare lightweight concrete for building construction [32]. The lightweight concrete can be formed by adding zeolite powders into the liquid cement as the porous structure of zeolites provides a very high volume per tonne with similar hardness and strength. In addition, the micropores of zeolites contain moisture, which facilitates a more rapid curing (curing is the process of controlling the rate of moisture loss from concrete during cement hydration) and results in the desirable strength and durability of concrete.

1.1.4 Dealumination

The diffusion behavior of hydrocarbons in zeolites has been studied for decades [17, 33–39]. An important condition for zeolite catalysis is that the size of micropores needs to match the adsorbate molecules. In this way, guest molecules can diffuse inside the confined environment imposed by the micropores of the zeolites. However, micropores often limit the catalytic performance by restricting molecular transport inside zeolite crystals. The diffusion coefficients in micropores are typically ranging from 10^{-8} to 10^{-20} m^2/s, while the diffusivity in meso/macropores of zeolites has a value close to the molecular and Knudsen diffusion, ranging from 10^{-4} to 10^{-8} m^2/s [34].

In most cases, the low diffusivity of adsorbates in zeolite crystals limits the reaction rates. One solution to minimize this transport limitation is the reduction of the intracrystalline diffusion path. It has been demonstrated that decreasing the zeolite crystal size and reducing the intracrystalline diffusion path can effectively improve the catalytic performance of Mordenite (MOR) [40], zeolite Y [41], ZSM-5 [42], zeolite beta [43], etc. The advantages of decreasing the crystal size of zeolites are twofold: *(1)* The reaction products diffuse out of zeolites more easily. In this way, side reactions such as coking and cracking can be suppressed. *(2)* The surface area increases for small zeolite crystals. This leads to an significant increase of the accessibility and activity.

In experiments, hydrothermal treatments with steaming are often used to enhance molecular diffusion by creating mesopores inside zeolite crystals [45, 46]. Even though thermal treatment without steaming is able to create defect domains in zeolites, steaming is preferred in most cases as it can mobilize the framework Al and Si atoms to a large extent [47]. The hydrolysis of Si-O-Al bonds takes place during steaming, especially at high temperatures [44]. The extraction of one framework Al atom generates a framework vacancy containing four silanol groups, often referred to as a silanol nest. Some zeolites contain certain amounts of stacking fault domains caused by the the mismatch of zeolite building units during synthesis [48]. These domains were identified as instable regions which are preferentially amorphized during steaming [49]. The amorphous material generated in stacking fault domains is a source of mobile Si atoms, which can heal silanol nests present in the zeolite framework. In this way, some of the framework vacancies can be recovered while others may transform into large micropores or mesopores. A schematic drawing of the dealumination mechanism is shown in Fig. 1.4. This figure shows the structural changes of the zeolite framework upon dealumination [44]. The dealumination process starts with the removal of framework Al, and the amorphization preferentially takes place at the stacking fault domains and the crystal surfaces. Part of the silanol nests will be healed by the non-framework Si released from the amorphous regions. The other silanol nests will eventually form mesopores [44]. Note that the debris created during dealumination may partially block the micropores, resulting in a lower accessibility of the zeolite.

After steaming, mesopores are usually filled with debris generated from the partial amorphization of the zeolite framework. Steaming causes an increase of the framework Si/Al ratio while leaving the bulk Si/Al ratio unchanged. The non-framework material in both micro- and mesopores can be removed by mild acid leaching [50, 51]. Inorganic acids like diluted nitric acid or

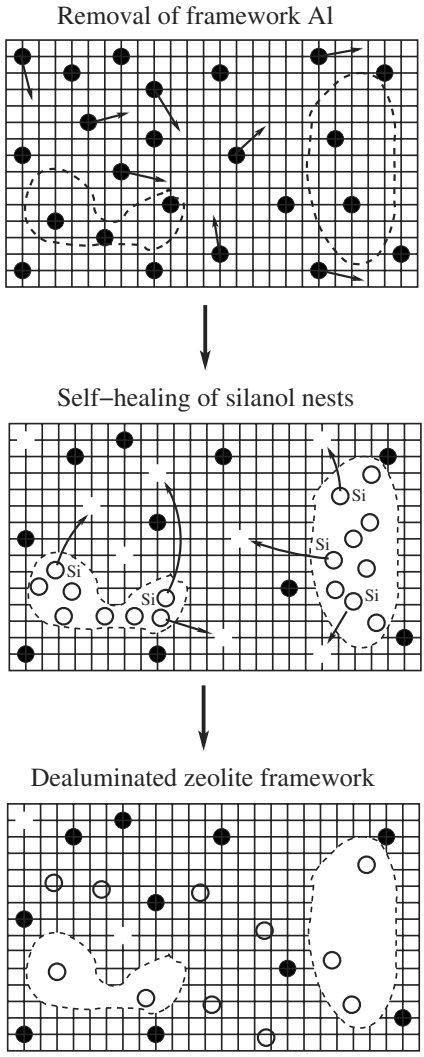

Figure 1.4: Schematic representation of the dealumination mechanism of zeolites as proposed by Marcilly *et al*. [44]. The dealumination process starts with the removal of framework Al, and the amorphization of zeolite framework at the stacking fault domains. Some of the generated silanol nests will be healed by non-framework Si generated in the amorphous domains. The remaining silanol nests will eventually form mesopores. The symbols are defined as follows: the grid points denote the zeolite framework; the dashed lines are the boundaries of mesopores; the filled dots are the framework Al atoms; the open dots are the non-framework Al atoms extracted from the framework and the migrating Si atoms. from the zeolite framework.

organic acids like oxalic acid can be used for acid leaching. The debris in mesopores formed during steaming can be removed, resulting in a higher mesopore volume after acid leaching. Direct acid leaching can also create mesopores in zeolites [52]. Treatment with strong inorganic acids results in the removal of the framework Al which causes an increase of the Si/Al ratio.

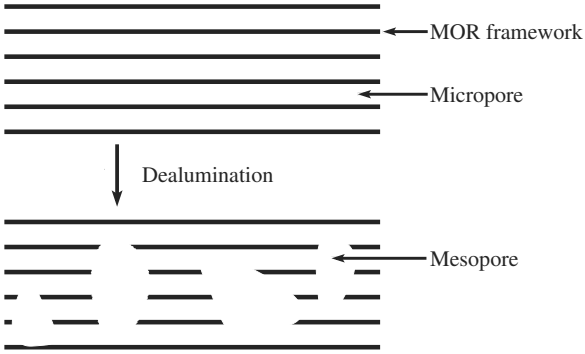

Figure 1.5: Schematic representation of the transformation of MOR-type zeolite from a one-dimensional to a three-dimensional porous system by the creation of intracrystalline mesopores. The starting structure has a one-dimensional structure consisting of main channels. After dealumination, the main channels are connected by the created mesopores forming a three-dimensional structure. The lines denote the walls of the main channels in MOR-type zeolite.

Dealumination has been used to improve the catalytic performance of zeolites in industrial applications. For instance, Dow Chemical developed a MOR-type zeolite catalysts to produce cumene based on the acid-catalyzed alkylation of benzene with propene [53, 54]. The current process uses dealuminated Mordenite with a high Si/Al ratio which is obtained by acid leaching and steaming treatments [55]. The high catalytic activity of dealuminated Mordenite is attributed to several factors: *(1)* It is known that the concentration of the framework Al influences the acidity of the Brønsted acid sites [56]. During dealumination, the extraction of framework Al atoms deceases the number of the acid sites, while the acid strength of the remaining Brønsted acid sites is enhanced as the number of Al-O-Si-O-Al linkages in the zeolite framework is minimized [57]. *(2)* The removal of amorphous material in the zeolite micropores enhances the diffusivity of the reactants and products. *(3)* Dealumination introduces mesopores which enhance the molecular diffusivity and preventing rapid deactivation of the MOR catalyst, see Fig. 1.5. As the size of the micropores is not strongly affected by dealumination, the selectivity maintains large in MOR frameworks [58, 59].

1.1.5 Synthesis of cumene

Production processes of bulk chemicals are often operated with a large excess of one reactant fed into the reactor in order to suppress side reactions. This requires a high recycle rate and an additional separation step, resulting in both large energy consumption and high capital investment. Alkylation processes are an important example in which reactive alkenes are coupled to much less reactive alkanes or aromatics. For instance, cumene, i.e. isopropylbenzene, is synthesized by the alkylation of benzene and propene. The production of cumene suffers from a large excess of benzene as high benzene to propene ratios are applied to suppress side reactions, such as alkene oligomerization. As shown in Fig. 1.6, cumene is produced by alkylation of benzene with propene using an acid catalyst which can be either a solid acid, aluminium chloride or protonated zeolites [55, 60–62]. Typical process conditions for the solid acid catalyzed process are $30 \sim 40$ bar, $180 \sim 230^{\circ}$C, benzene/propene ratio in the reactor feed: $\mathrm{B/P} = 5 \sim 7$ and a low space velocity [55, 62]. Recent developments are aiming to replace the solid phosphoric acid by zeolite-based catalysts [53, 54, 63]. The lower operating temperature ($< 150^{\circ}$C) largely prevents the formation of

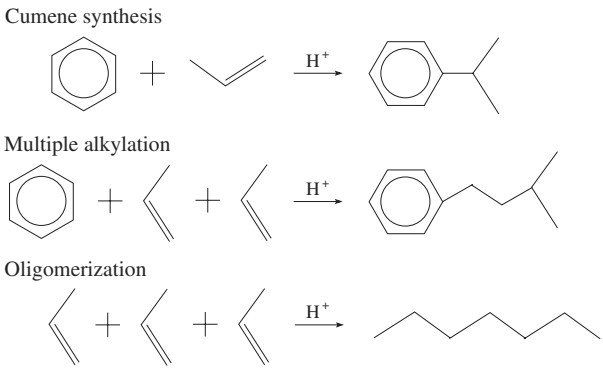

Figure 1.6: Cumene synthesis from benzene and propene. The major side reactions are *(1)* the multiple alkylation of benzene and propene and *(2)* propene oligomerization. This reaction is catalyzed by Brønsted acid sites in protonated zeolites.

n-propylbenzene in zeolites, which will lead to considerable yield loss when using older processes based on the solid phosphoric acid [55, 62]. However, an important research target that remains is to lower the B/P ratio in the feed as close as possible to one.

MOR-type zeolite has been proved an effective catalysts for cumene production [53–55, 63]. The advantage of MOR catalysts is the high adsorption selectivity of benzene in benzene/propene mixtures due to the unique porous structure. MOR consists of twelve-membered main channels that connect to side pockets that are accessible through eight-membered rings. The eight-membered channel that connects the twelve-membered channels is tortuous and most hydrocarbon molecules cannot pass through. Therefore, MOR is considered as a one-dimensional structure. As the heat of adsorption of aromatics is much larger than for propene in the main channels, the adsorption selectivity of benzene is high enough to prevent propene oligomerization and multiple alkylation in main channels. However, the one-dimensional structure hinders the accessibility

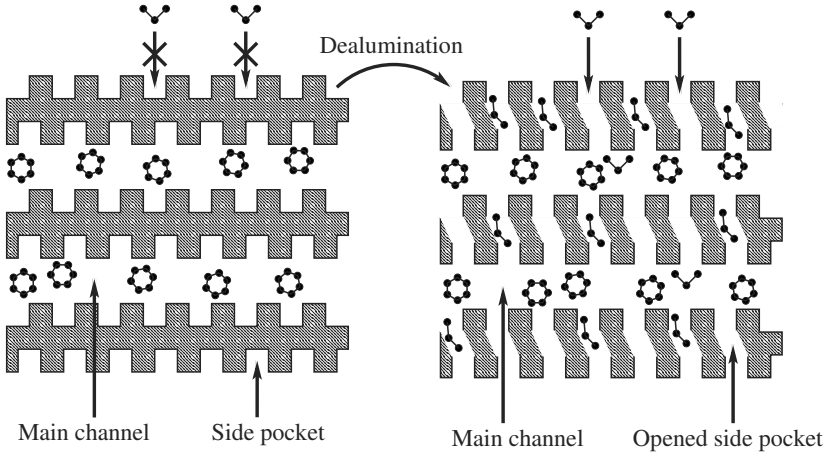

Figure 1.7: Schematic representation of the possible molecule traffic control mechanism for a mixture of benzene and propene in MOR-type zeolite. After dealumination, the side pockets are expected to be opened, and thus propene is able to diffuse through the connected side pockets. This speculative concept will be evaluated by further studies.

and transport of guest molecules inside MOR. Dealumination is often applied to modify the MOR framework into a three-dimensional porous system. Evidence exists that with highly dealuminated MOR the eight-membered windows and side pockets do not contain Al atoms [64–66]. In other words, the acid sites are exclusively located in the main channels. Furthermore, studies by researchers from Dow Chemical [63, 67, 68] have shown that dealumination significantly modifies the pore topology of MOR. In addition to to mesopores that shorten the effective diffusion length of the main channels, also the nature of the micropores has changed as has been deduced from low-pressure nitrogen physisorption studies. It is speculated that a three-dimensional framework of MOR comprises a modified eight-membered channel system that allows propene to pass from one main channel to another. In such a MOR crystal the diffusion of reactants could take place in two directions, i.e. benzene/cumene exclusively via the main channels and propene largely via the eight-membered channel system, see Fig. 1.7. This diffusion behavior corresponds to the hypothesis of molecular traffic control [69, 70]. This concept suggests a simultaneously feed of two types of reactants into zeolites via well-defined channels of different size without counter-diffusion. The feasibility to adopt this speculative concept for cumene production is worth studying further.

1.2 Molecular simulation

1.2.1 Zeolite models

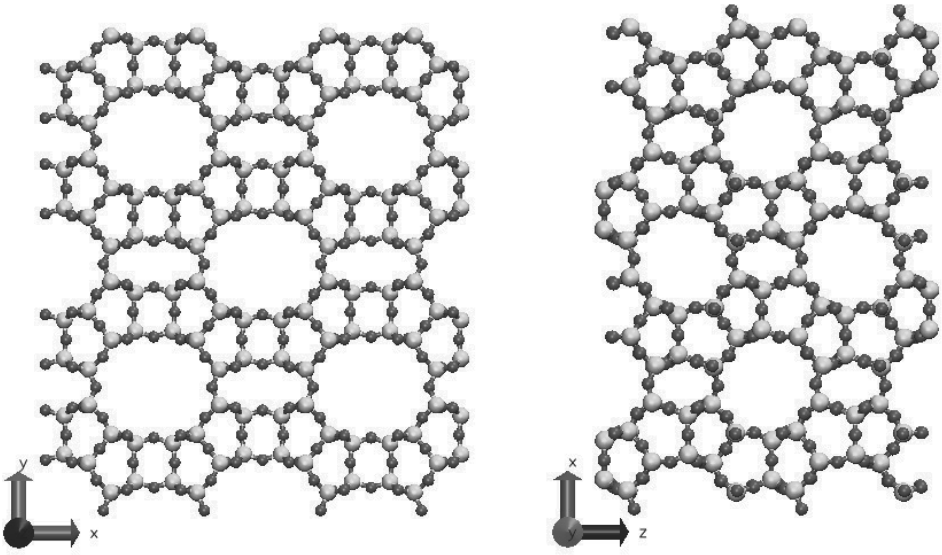

Figure 1.8: Zeolite frameworks. (left) MOR-type zeolite and (right) MFI-type zeolite. The figure shows a MOR lattice consisting of $2 \times 2 \times 4$ unit cells oriented along the z crystallographic axis, and a MFI lattice consisting of $2 \times 2 \times 2$ unit cells oriented along the y crystallographic axis. MOR-type zeolite consists of large main channels (7 Å) oriented in the z crystallographic axis connected by small side pockets (3.4×4.8 Å). MFI-type zeolite consists of straight channels (5.3×5.6 Å) in the y crystallographic axis intersected by zigzag channels (5.1×5.5 Å) along the x crystallographic axis. Silicon atoms are represented by yellow spheres. Oxygen atoms are denoted by red spheres.

As discussed in section 1.1.1, the zeolite lattice consists of TO_4 tetrahedra, where the T atom can be either Al or Si (see Fig. 1.8). In particular, the bond length of Al-O is shorter than that of Si-O, which is often observed in X-ray diffraction experiments [46, 71]. The distribution of the framework Al obeys the Löwenstein rule, namely that the Al-O-Al linkage is prohibited. Five

possible Si-Al connectivities exist, i.e. Si(0Al), Si(1Al), Si(2Al), Si(3Al) and Si(4Al), which denotes the number of next nearest Al neighbors around a Si atom.

In molecular simulations, it is often assumed that the zeolite is rigid. In this case, the positions of the framework atoms are fixed during simulations. For adsorption of alkanes, the flexibility of zeolite frameworks does not influence the adsorption isotherms (the number of adsorbed guest molecules as a function of the pressure at constant temperature) [72]. In this way, the computation of the interaction between the zeolite framework and the guest molecules can be considerately simplified by using grid interpolation techniques [73–75]. However, the flexibility of zeolite frameworks may be of importance in same cases. For instance, the framework flexibility influences the diffusion of guest molecules, especially for tight-fitting molecules [76].

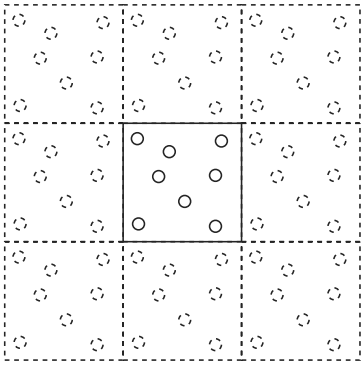

Figure 1.9: Schematic illustration of periodic boundary conditions. The central simulation box is surrounded by identical copies. The particles in all images move in exactly same way as in the central box. When a molecule leaves the central box, it will enter the central box from the opposite side.

The zeolite framework is often modeled using the periodic boundary conditions (see Fig. 1.9). The original simulation box is replicated throughout space. During the simulation, the molecules in all periodic images move in the same way as the ones in the central box. If a molecule leaves the central box, it will enter the central box from the opposite side. It is convenient to use the minimum-image convention, which means that an atom i may only interact with the nearest image of atom j [77].

1.2.2 Molecular models

In the classical approach, polyatomic molecules can be described by either the all-atom model or the united-atom model. In the all-atom model, each atom is considered as an interaction site. In the united-atom model, a group of atoms are represented by a single interaction site. For example, the united-atom model is often used for CH_2, CH_3 and CH_4 groups of alkanes where the hydrogen atoms are usually not modeled as separate interaction sites. The interaction parameters for groups containing a different number of hydrogen atoms are usually different [78]. The all-atom approach takes into account the molecular geometry and structure more realistically. However, as the number of interaction sites is much larger than that of the united-atom model, simulations using the all-atom model will be computationally more expensive [79, 80].

1.2.3 Interaction potentials

The term force field refers to the functional form and parametrization used to describe the potential energy U of a system of interacting molecules. Force fields are usually derived from experiments and quantum mechanical calculations [81, 82]. A classical force field contains bonded and non-bonded potentials, i.e. U^{bonded} and $U^{\text{non-bonded}}$, respectively. The total energy U^{total} can often be

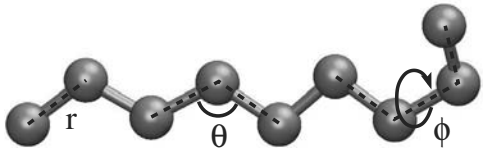

Figure 1.10: United-atom representation of n-nonane. For some bonded interactions, the bond length r, bending angle θ and torsion angle ϕ are shown.

expressed by

$$U^{\text{total}} = U^{\text{bonded}} + U^{\text{non-bonded}} \tag{1.1}$$
$$U^{\text{bonded}} = U^{\text{bond}} + U^{\text{bend}} + U^{\text{torsion}} \tag{1.2}$$
$$U^{\text{non-bonded}} = U^{\text{LJ}} + U^{\text{elec}} \tag{1.3}$$

The typical bonded potentials are the bond-stretching potential U^{bond}, the bond-bending potential U^{bend} and the torsional potential U^{torsion}. The interaction parameters for bonded interactions are usually derived from quantum mechanical calculations [83, 84]. The non-bonded potentials generally consist of a Lennard-Jones (LJ) potential U^{LJ} and a long-range Coulombic potential U^{elec}. The non-bonded potentials are often pair potentials that only depend on the distance between two interacting atoms. To calculate the total energy U^{total} of a molecular system, one has to add the contributions from all bonded and non-bonded interactions in the system.

Bond-stretching potential The bond-stretching potential U^{bond} is the potential energy of two neighboring atoms in a molecule. There are many functional forms for the bond-stretching potentials, e.g. the Morse potential, the Quartic potential, the Buckingham potential, etc. The often used harmonic bond-stretching potential is defined as

$$U^{\text{bond}} = \frac{1}{2} k_r (r - r_0)^2 \tag{1.4}$$

where k_r is the stiffness of the bond, r is the distance between two neighboring atoms, and r_0 is the equilibrium bond length, see Fig. 1.10. In simulations, many molecules like CO_2, N_2 and benzene can be modeled with fixed bond lengths.

Bond-bending potential The bond-bending potential U^{bend} is the potential energy associated with the angle θ between two successive bonds of three neighboring atoms in a molecule. There are many functional forms for the bond-bending potentials like the Harmonic cosine potential, the Quartic potential, the Cosine potential, the MM3 stretch-bend potential, etc. The often used harmonic form of the bond-bending potential is defined as

$$U^{\text{bend}} = \frac{1}{2} k_\theta (\theta - \theta_0)^2 \tag{1.5}$$

where θ_0 is the equilibrium angle and k_θ is the bond-bending constant, see Fig. 1.10. Both parameters can be obtained from the quantum mechanical calculation or infrared spectroscopy [85]. For the sp^3 hybridization of alkanes, the tetrahedral symmetry results in the average angle $\theta_0 \approx 110^\circ$. The very stiff molecule is often modeled with a fixed bond-bending angle. For instance, CO_2 molecules are often modeled as a rigid molecule by fixing the bond-bending angle of O-C-O at 180°.

Torsional potential The torsional potential U^{torsion} is related to the dihedral angle ϕ of four successive atoms in a molecule, see Fig. 1.10. There are many functional forms for the torsional potentials like the Cosine potential, the Harmonic potential, the OPLS angle potential, etc. The often used Ryckaert-Bellemans potential defined as

$$U^{\text{torsion}} = \sum_{i=0}^{5} a_i \cos^i(\phi) \tag{1.6}$$

where the factors a_i can be derived from the quantum mechanical calculations. This torsional potential often has several minima and maxima, which corresponds to the various conformations of the molecule.

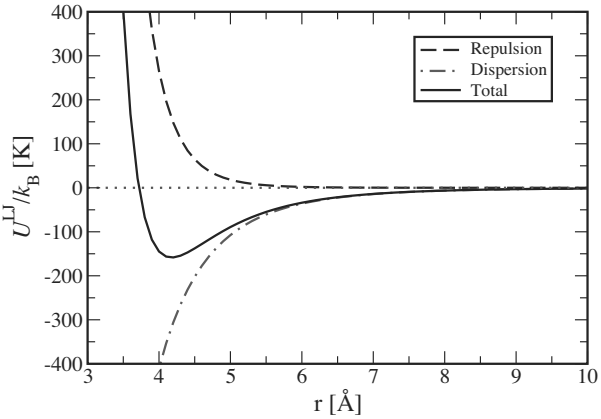

Figure 1.11: Lennard-Jones potential of methane with interaction parameters $\sigma = 3.72$ Å and $\varepsilon/k_{\text{B}} = 158.5$ K. The total Lennard-Jones potential has a minimum of $-\varepsilon$ at $r_{\text{min}} = 2^{1/6}\sigma \approx 4.2$ Å.

LJ interaction The LJ potential is a widely used potential to describe short-range interactions. The LJ potential is a pair potential depending on the distance between two atoms of different molecules, as well as between two atoms in the same molecule. Usually, only intramolecular LJ interactions between atoms separated by more than three bonds are taken into account [84]. In this way, intramolecular overlaps are avoided. The LJ potential between two interacting atoms is defined as

$$U^{\text{LJ}}_{\text{pair}} = U^{\text{repuls}} + U^{\text{disper}} = 4\varepsilon \left[\left(\frac{\sigma}{r_{ij}} \right)^{12} - \left(\frac{\sigma}{r_{ij}} \right)^{6} \right] \tag{1.7}$$

where σ is the LJ size parameter, and ε is the potential well depth at a separation distance of $r_{\text{min}} = 2^{1/6}\sigma$, so $U(r_{\text{min}}) = -\varepsilon$. The parameter ε is often given in units of ε/k_{B} with a dimension of temperature. In Eq. 1.7, the attractive r^{-6} part of the LJ potential corresponds to dispersive van der Waals interactions, while the repulsive part r^{-12} represents the repulsion of two atoms at short distances (see Fig. 1.11).

As the LJ potential quickly vanished at long distances, it is convenient to truncate and shift this interactions at the so-called cut-off radius r_{c}. This will significantly increase the computational efficiency. The truncated and shifted LJ potential is defined as

$$U^{\text{ts}}(r_{ij}) = \begin{cases} U^{\text{LJ}}_{\text{pair}}(r_{ij}) - U^{\text{LJ}}_{\text{pair}}(r_{\text{c}}) & \text{r} \leq \text{r}_{\text{c}} \\ 0 & \text{r} > \text{r}_{\text{c}} \end{cases} \tag{1.8}$$

where $U^{\text{ts}}(r_{ij})$ denotes the truncated and shifted LJ potential and r_{c} is the cut-off distance. The typical cut-off distance of the LJ potential is usually chosen as $r_{\text{c}} \geq 2.5\sigma$. According to the nearest

image conversion in section 1.2.1, the length of the simulation box needs to be at least twice as large as the cut-off distance.

The value of the LJ parameters σ and ε are often fitted from experimental data such as the critical temperature and density [86]. For interactions with zeolites, LJ parameters are fitted to experimental adsorption data [81]. The parameters of σ_{ij} and ε_{ij} between different atoms i and j can be estimated from the LJ parameters of σ_{ii} and ε_{ii} of identical atoms. The most common mixing rule is the Lorentz-Berthelot mixing rule [73]:

$$\sigma_{ij} = \frac{\sigma_{ii}+\sigma_{jj}}{2} \tag{1.9}$$

$$\varepsilon_{ij} = \sqrt{\varepsilon_{ii}\varepsilon_{jj}} \tag{1.10}$$

Electrostatic interaction The electrostatic potential is an important interaction that needs to be considered in many molecular simulations. For a pair of point charges in a continuous medium, the electrostatic potential is given by:

$$U_{\text{pair}}^{\text{elec}} = \frac{1}{4\pi\varepsilon_0\varepsilon_r}\frac{q_i q_j}{r_{ij}} \tag{1.11}$$

where ε_0 is the permittivity of vacuum, ε_r the relative dielectric constant of the medium, q_i the partial charge of atom i, and r_{ij} the distance between atoms i and j. As the polarization effects are often neglected, the partial charge on a certain atom is constant. The magnitude and distribution of the partial charges in a molecule are chosen such that the dipole or higher order moments of the molecule taken from quantum mechanical calculations are reproduced

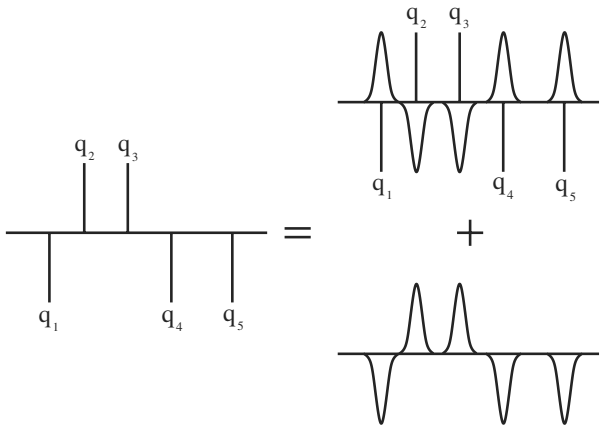

Figure 1.12: Schematic representation of the Ewald summation. Point charges (solid straight lines, denoted by q_i) are screened by a Gaussian charge distribution (solid curve) of opposite sign, making the electrostatic interactions short-range. This can be corrected by computing the interaction energy of the added Gaussian charge distribution with the same sign as the point charges.

Compared to the LJ potential (r^{-6}), the range of the electrostatic interaction (r^{-1}) is much larger. Due to the long-ranged nature of electrostatic interactions, simple truncation cannot be used [87]. Instead, the Ewald summation is often applied to accurately calculate the long-range interaction in simulation systems with periodic boundary conditions [88]. In the Ewald summation, the total Coulombic energy of the system can be written as the sum of three contributions (see Fig. 1.12):

- The real-space part, which is given by

$$U_{\text{real}} = \frac{1}{4\pi\varepsilon_0\varepsilon_r}\sum_{i<j}\frac{q_i q_j \text{erfc}(\alpha r_{ij})}{r_{ij}} \tag{1.12}$$

in which erfc(x) is the complementary error function. r_{ij} is the distance between particles i and j. q_i and q_j are the charges on particles i and j respectively and α is a constant damping factor. The summation $\sum_{i<j}$ is in principle a summation over all periodic images of i and j. However, it is convenient to choose α in such a way that only the nearest images have to be considered (as erfc(x) is close to zero for large x). This requires a value of α that is not too small. The real-space part of the Ewald summation and the conventional Lennard-Jones interactions can be calculated simultaneously using the same cut-off radius.

- The self energy

$$U_{\text{self}} = -\frac{1}{4\pi\varepsilon_0\varepsilon_r}\frac{\alpha}{\sqrt{\pi}}\sum_{i=1}^{N} q_i^2 \tag{1.13}$$

which does not depend on the positions of charged atoms in the system.

- The Fourier part of the energy, which follows from

$$U_{\text{Fourier}} = \frac{1}{4\pi\varepsilon_0\varepsilon_r}\frac{1}{2V}\sum_{\mathbf{k}\neq 0}^{\infty}\frac{\exp(-k^2/4\alpha^2)}{k^2}|\sum_{j=1}^{N} q_j \exp(-i\mathbf{k}\cdot\mathbf{r}_j)|^2 \tag{1.14}$$

in which V is the volume of the system and the vectors $\mathbf{k}$ are linear combinations of the reciprocal basis vectors of the system.

The Ewald method is a very accurate method to calculate the electrostatic potential in the system with periodic boundary conditions [77]. However, a considerable computation time is consumed in calculating the Fourier-space part of the Ewald summation. To speed up the calculation for large systems, the so-called Wolf method has been introduced recently as a pairwise alternative for the Ewald summation [89]. In this method, the Coulombic interactions are damped using a complementary error function that is truncated and shifted at a cut-off distance r_{cut} resulting in the following pair potential

$$U_{\text{Wolf}}(r_{ij}) = \begin{cases} \frac{q_i q_j}{4\pi\varepsilon_0\varepsilon_r}\left[\frac{\text{erfc}(\alpha r_{ij})}{r_{ij}} - \frac{\text{erfc}(\alpha r_{cut})}{r_{cut}}\right] & r_{ij} \leq r_{cut} \\ 0 & r_{ij} > r_{cut} \end{cases} \tag{1.15}$$

In this thesis, the feasibility of using the Wolf method to compute Coulombic interactions will be discussed in chapter 3.

1.3 Monte Carlo methods

1.3.1 Statistical mechanics

In statistical mechanics, the partition function is the central important quantity. All the thermodynamic variables of the system, such as the total energy, free energy, entropy, pressure, etc., can be directly calculated from the partition function. The classical expression of the partition function Q for a N-particle system is defined as

$$Q = \frac{1}{N!h^{3N}}\int \exp[-\beta\mathscr{H}(r^N, p^N)]dr^N dp^N \tag{1.16}$$

where r^N and p^N denote the positions and momenta, respectively, and h is Planck's constant [77]. The function $\mathscr{H}(r^N, p^N)$ is the Hamiltonian of the system, which is the total energy as a function of the coordinates and momenta of the particles. For a system with a constant number of particles N, volume V and temperature T, the free energy F is given by

$$F(N,V,T) = -k_{\text{B}}T\ln Q(N,V,T) \tag{1.17}$$

where k_B is Boltzmann constant.

Except for a few trivial systems like the ideal gas, it is impossible to compute the partition function directly. The reasons for this are twofold: *(1)* the number of points in configuration space at which the integrand in Eq. 1.16 must be evaluated is extremely large. *(2)* For most of these points, the integrand is zero. However, the often interested quantity is not the partition function itself but averages of the type

$$\langle A \rangle = \frac{\int \exp[-\beta U(r^N)] A(r^N) dr^N}{\int \exp[-\beta U(r^N)] dr^N} = \frac{\int \exp[-\beta U(r^N)] A(r^N) dr^N}{Z} \tag{1.18}$$

where $\beta = 1/(k_B T)$ with k_B being Boltzmann constant, and $U(r^N)$ is the potential energy of the system with positions r^N. The configurational part of the partition function is denoted by Z. The value of $\exp[-\beta U(r^N)]/Z$ is the probability distribution that the system is in the system state r^N, which is defined as

$$\mathscr{N}(r^N) \equiv \frac{\exp[-\beta U(r^N)]}{Z} \tag{1.19}$$

In principle, one can generate system states at random, leading to

$$\langle A \rangle = \lim_{n \to \infty} \frac{\sum_{i=1}^{n} A_i \exp(-\beta U_i)}{\sum_{i=1}^{n} \exp(-\beta U_i)} \tag{1.20}$$

In practice, this expression leads to meaningless results as Boltzmann factors are nearly always zero for randomly generated states. This issue can be solved by the so-called Metropolis Monte Carlo method, which will be described in the next section.

1.3.2 Metropolis Monte Carlo

The Metropolis Monte Carlo Method [90, 91] is a process in which a random walk is constructed in such a way that the probability of visiting a particular system state is proportional to the Boltzmann factor $\exp[-\beta U_i]$. For such a sequence, the average in Eq. 1.20 becomes

$$\langle A \rangle = \lim_{n \to \infty} \frac{\sum_{i=1}^{n} A_i}{n} \tag{1.21}$$

Consider a N-particle system in the state denoted by o with the energy $U(o)$. The system can jump to a new state n, by, for example, giving one of the particles a random displacement. This new state n is either accepted or rejected in such a way that states are visited with a probability proportional to $\mathscr{N}$. It turns out that a sufficient condition for this is that the equilibrium distribution $\mathscr{N}$ is not destroyed by the way that states are accepted or rejected. To be specific, from the state old o, m different new state n are accessible. The probability of leaving state o must be equal to that of entering state o. This leads to the balance equation

$$\mathscr{N}(o) \sum_m [\alpha(o \to n) P_{acc}(o \to n)] = \sum_m [\mathscr{N}(n) \alpha(n \to o) P_{acc}(n \to o)] \tag{1.22}$$

where $\mathscr{N}(o)$ is the probability of the configuration in the state o, which is proportional to the Boltzmann factor $\exp(-\beta U_i)$, $\alpha(o \to n)$ the probability to select the move from the old state o to the new state n, and $P_{acc}(o \to n)$ is the probability of accepting the trial move from the state o to the state n. It is convenient to impose a much stronger condition that in equilibrium the average number of accepted moves from the old state to any other new state should be exactly canceled by the number of reverse moves. This is the so-called detailed balance condition:

$$\mathscr{N}(o) \alpha(o \to n) P_{acc}(o \to n) = \mathscr{N}(n) \alpha(n \to o) P_{acc}(n \to o) \tag{1.23}$$

In the Metropolis Method, α is chosen to be a symmetric matrix, namely $\alpha(o \to n) = \alpha(n \to o)$. As a result, the acceptance rule follows

$$\frac{P_{acc}(o \to n)}{P_{acc}(n \to o)} = \frac{\mathscr{N}(n)}{\mathscr{N}(o)} = \exp\{-\beta[U(n) - U(o)]\} = \exp(-\beta \Delta U) \tag{1.24}$$

Metropolis suggested the following choice for $P_{acc}(o \rightarrow n)$:

$$P_{acc}(o \rightarrow n) = \min(1, \exp(-\beta \Delta U)) \tag{1.25}$$

The Metropolis Method works as follows:

1. Start from an initial configuration. For example, random positions can be generated for all N particles in the system.
2. Compute the total energy $U(o)$ of the old state.
3. Make a trial move to a new configuration n by, for example, displacing one of the particles at random.
4. Compute the total energy $U(n)$ of the new state.
5. Accept this trial move with the probability in Eq. 1.25.
6. Sample ensemble averages according to Eq. 1.21.
7. Repeat this procedure from step 2 many times until the system reaches equilibrium.

For more details on the Monte Carlo methods, we refer the reader to specialized text books [77, 87, 92].

1.3.3 Configurational-Bias Monte Carlo

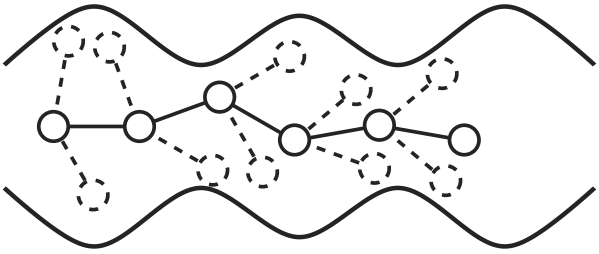

Figure 1.13: Schematic representation of the growth of a chain molecule in a zeolite micropore using Configurational-Bias Monte Carlo. A chain molecule of six beads is grown segment by segment from left to right. For the insertion of each bead, three trial directions are generated according to Eq. 1.27. One of these is selected according to Eq. 1.28.

The sampling of equilibrium conformations of long chain molecules can be time-consuming. The reason for this is that the natural dynamics of chain molecules is slow [93–95]. As a solution, Configurational-Bias Monte Carlo (CBMC) is used to sample the internal degrees of freedom of chain molecules [96–99]. In CBMC, the total energy is split into two parts: *(1)* the bonded potential U^{bond}, including bond-stretching (Eq. 1.4), bond-bending (Eq. 1.5) and torsional interactions (Eq. 1.6). *(2)* The non-bonded (external) potential accounts for all intermolecular interactions and for all non-bonded intramolecular interactions. In CBMC, a chain molecule with l beads is constructed segment by segment (see Fig. 1.13) in the following way:

1. The first segment is inserted at a random position $\mathbf{r}_1$. Its external energy is $U_1^{\text{non-bonded}}(\mathbf{r}_1)$, and the Rosenbluth factor of the first bead is given by

$$w_1^{\text{non-bonded}}(n) = \exp[-\beta U_1^{\text{non-bonded}}(\mathbf{r}_1)] \tag{1.26}$$

2. For the other segment, k trial segments $\{\mathbf{s}\}_k = \{\mathbf{s}_1, \cdots, \mathbf{s}_k\}$ are generated with a probability

$$P_i^{\text{bond}}(\mathbf{s}) = \frac{\exp[-\beta U_i^{\text{bond}}(\mathbf{s})]}{\int \exp[-\beta U_i^{\text{bond}}(\mathbf{s})] d\mathbf{s}} = C \exp[-\beta U_i^{\text{bond}}(\mathbf{s})] \tag{1.27}$$

where i represents the ith trial segment.

3. For all k trial segments, we calculate the Boltzmann factor of the non-bonded interactions $\exp[-\beta U_i^{\text{non-bonded}}(\mathbf{s}_i)]$ and then select one segment n according to

$$P_i^{\text{non-bonded}}(\mathbf{s}_n) = \frac{\exp[-\beta U_i^{\text{non-bonded}}(\mathbf{s}_n)]}{\sum_{j=1}^{k} \exp[-\beta U_i^{\text{non-bonded}}(\mathbf{s}_j)]} = \frac{\exp[-\beta U_i^{\text{non-bonded}}(\mathbf{s}_n)]}{w_i^{\text{non-bonded}}(n)} \tag{1.28}$$

In this way, the selected segment n becomes the ith segment of the chain molecule.

4. This procedure is repeated until the whole chain is grown. For the new configuration, the Rosenbluth factor is defined by

$$W^{\text{non-bonded}}(n) = \prod_{i=1}^{l} w_i^{\text{non-bonded}}(n) \tag{1.29}$$

The same procedure is used to compute the Rosenbluth factor for the old conformation of the chain molecule:

1. A chain molecule is selected at random.

2. The non-bonded potential of the first bead of the chain molecule is calculated. We compute its Boltzmann factor

$$w_1^{\text{non-bonded}}(o) = \exp[-\beta U_1^{\text{non-bonded}}(o)] \tag{1.30}$$

3. For the other $l-1$ beads of the chain molecule, the function $w_i^{\text{non-bonded}}$ of the bead i is computed as follows. A set of $k-1$ trial segments are generated according to Eq. 1.27, while the kth segment is the old segment of the chain itself.

$$w_i^{\text{non-bonded}}(o) = \sum_{j=1}^{k} \exp[-\beta U_i^{\text{non-bonded}}(\mathbf{s}_j)] \tag{1.31}$$

4. The Rosenbluth factor of the old conformation is given by

$$W^{\text{non-bonded}}(o) = \prod_{i=1}^{l} w_i^{\text{non-bonded}}(o) \tag{1.32}$$

The trial move from the old state o to the new state n is accepted with a probability

$$P_{acc}(o \rightarrow n) = min(1, W^{\text{non-bonded}}(n)/W^{\text{non-bonded}}(o)) \tag{1.33}$$

In Refs. [97–99], it is shown that the acceptance rule of Eq. 1.33 obeys detailed balance. During the past few years, several improvements or modifications of CBMC method have been proposed [100–105]. For the application of CBMC to branched molecules, we refer the reader to Refs. [83, 84, 106].

1.3.4 Monte Carlo trial moves

Monte Carlo (MC) trial moves can be used for MC simulations in various ensembles. The typical ensembles involved in this thesis are the canonical (NVT) ensemble, the grand-canonical (μVT) ensemble and the Gibbs ensemble [77]. In the canonical ensemble, the number of particles, the temperature and the volume are constant. For studying the adsorption of guest molecules in porous materials, the grand-canonical ensemble (μVT) is often used to calculate the number of guest adsorbed molecules as a function of pressure and temperature. This is called the adsorption isotherm. In μVT ensemble, the temperature, volume and chemical potential are fixed. The system can exchange molecules with a reservoir of isolated chain molecules at a given chemical potential μ and temperature T. Using the equation of state for the guest molecules, the chemical potential can be converted to the pressure of the gas or liquid in the reservoir, see Fig. 1.14. The Gibbs ensemble is often used to study the phase equilibria, especially vapor-liquid equilibria [107, 108]. This requires that the pressure, temperature and chemical potential of the coexisting phases are equal. The simulation in Gibbs ensemble involves two simulations boxes. The particles in the two boxes do not interact. These boxes can exchange volume and particles during the simulation.

A typical Monte Carlo simulation may consist of the following trial moves, depending on the ensemble:

Translation The translation move is used to give a random displacement to a randomly selected molecule. The maximum displacement is set in such a way that the acceptance probability is on average 50%. The displacement is accepted according to the acceptance rule in Eq. 1.25.

Rotation The rotation move is used to rotate a randomly selected molecule. The maximum rotation angle is set in such a way that the acceptance probability is on average 50%. The rotation is accepted according to the acceptance rule in Eq. 1.25.

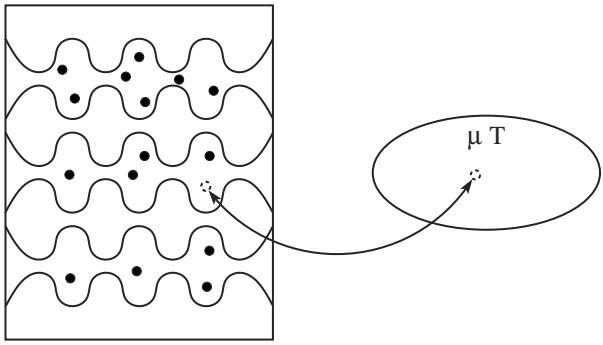

Figure 1.14: Schematic representation of the μVT ensemble. The zeolite is in contact with a particle reservoir at temperature T and chemical potential μ. Guest molecules are exchanged between the zeolite and the reservoir.

Insertion The insertion move is used to insert a molecule into the system at a random position [77]. For mixtures, component needs to be selected at random first. This move is only used in the grand-canonical ensemble, see Fig. 1.14. The insertion move is often performed using Configurational-Bias Monte Carlo which is able to successfully insert large chain molecules. The acceptance rule is equals to

$$P_{acc}(N \rightarrow N+1) = min\left(1, \frac{\beta V f}{N+1} \frac{W(n)}{\langle W_{IG} \rangle}\right) \tag{1.34}$$

The imposed chemical potential μ is related to the fugacity f by

$$\beta\mu = \beta\mu_{id} + \ln(\beta f) \tag{1.35}$$

where μ_{id} is the reference chemical potential. The pressure P is related to the fugacity f by $f = \phi P$ where ϕ is the fugacity coefficient computed directly from the equation of state [77]. $\langle W_{IG} \rangle$ is the average Rosenbluth factor of an isolated guest molecule.

Deletion The insertion move is used to remove a randomly selected molecule from the simulation box. For mixtures, component needs to be selected at random first. This move can be considered as the reverse process of the insertion move. The acceptance rule is given by

$$P_{acc}(N \to N-1) = min\left(1, \frac{N}{\beta V f}\frac{\langle W_{IG}\rangle}{W(o)}\right) \tag{1.36}$$

Regrowth The regrowth move is used to change the internal conformation and/or the position of a chain molecule. This move can be used to either fully regrow the molecule at a different position, or only regrow some segments of the molecule. The acceptance rule is given by

$$P_{acc}(o \to n) = min\left(1, \frac{W(n)}{W(o)}\right) \tag{1.37}$$

Identity change The identity change is used to change the identity of a molecule in the grand-canonical ensemble. For a mixture, one of the components is selected at random, having a identity A, and then a molecule with this identity is selected randomly. A trial move is generated by replacing this molecule with another one with a different identity B. The Rosenbluth factor $W(n)$ of the new trial configuration of the molecule B is calculated, while the old trial configuration of molecule A is retraced, leading to a Rosenbluth factor $W(o)$. The acceptance rule of the identity change is given by

$$P_{acc}(N_A, N_B \to N_A - 1, N_B + 1) = min\left(1, \frac{W(n) f_B \langle W_{IG}^A \rangle N_A}{W(o) f_A \langle W_{IG}^B \rangle (N_B + 1)}\right) \tag{1.38}$$

in which f_A, f_B are the fugacities of components A and B, and N_A, N_B are the number of molecules for each component in the system [109].

1.4 Kinetic Monte Carlo

The Kinetic Monte Carlo (KMC) method can be used to study the dynamics and time-evolution of systems based on the average rates of individual events [110]. This method is especially useful in a rare-event system. By definition, a rare-event system is a system where the dynamics is characterized by occasional transitions between states. In KMC, the events are assumed to be independent, which leads to a series of Poisson processes. This rejection-free residence-time procedure is often referred to as the n-fold way algorithm developed by Bortz *et al*. for ising spin systems [111].

The KMC method works as follows:

1. Set the time τ at $\tau = 0$
2. Construct a list of all possible events. Suppose that there are N events in total with the rate constants $r_1, \cdots, r_N$ in units of events per unit of time. It is assumed that these events are independent.
3. Select one of the events k with a probability

$$p_k = \frac{r_k}{\sum_{i=i}^{N} r_i} \tag{1.39}$$

4. Execute this event and advance the time for the next event $(k+1)$ by

$$\tau_{k+1} = \tau_k + \frac{|\ln(f)|}{\sum_{i=i}^{N} r_i} \tag{1.40}$$

where f is an uniformly distributed random number between 0 and 1.

5. Repeat this process, starting from step 2.

This method will be used to study the dealumination process of zeolites in chapter 6.

1.5 Molecular Dynamics

Molecular Dynamics (MD) is a method for computing equilibrium and transport properties of a classical many-body system. In MD, the time-evolution of a system is followed by integrating the Newton's laws of motion, i.e. $\mathbf{f} = m\mathbf{a}$ where $\mathbf{f}$ is the force acting on a particle, m the mass of a particle and $\mathbf{a}$ the acceleration, starting from initial positions and velocities of the particles [112]. Note that MD is used to generate representative trajectories for computing dynamic or thermal properties, rather than the actual trajectories which can be observed in reality [77]. The velocity Verlet algorithm is the most often used approach to integrate the equations of motion in MD. Using a Taylor expansion, the velocity Verlet algorithm can be easily derived:

$$\mathbf{r}(t+\Delta t) = \mathbf{r}(t) + \mathbf{v}(t)\Delta t + \frac{\mathbf{f}(t)}{2m}\Delta^2 t + \mathscr{O}(\Delta t^4) \tag{1.41}$$

$$\mathbf{v}(t+\Delta t) = \mathbf{v}(t) + \frac{\mathbf{f}(t) + \mathbf{f}(t+\Delta t)}{2m}\Delta t + \mathscr{O}(\Delta t^2) \tag{1.42}$$

where $\mathbf{r}(t)$ is the position of a particle at time t, m the mass of the particle, Δt the time step, and $\mathbf{v}(t)$ and $\mathbf{f}(t)$ are the velocity and force acting on that particle. The advantage of this algorithm is its simplicity. It is time reversible just as the Newton's equations of motion and having little energy drift for long time [87]. The time step Δt should be set in such a way that the energy of the total system (kinetic and potential energy) should be conserved. In NVE ensemble, the resulting energy drift ΔE should be sufficiently small after N integration steps.

$$\Delta E(\Delta t) = \frac{1}{N}\sum_{i=1}^{N}\left|\frac{E(\Delta t) - E(0)}{E(0)}\right| < 10^{-4} \tag{1.43}$$

The instantaneous temperature $T(t)$ is related to the total kinetic energy of the system:

$$T(t) = \sum_{i=1}^{N}\frac{m_i \mathbf{v}_i^2(t)}{k_B N_f} \tag{1.44}$$

where $\mathbf{v}$ the velocity and N_f the number of degrees of freedom ($N_f = 3N-3$ for a system containing N particles) at a fixed total moment. In Eq. 1.44, the equipartition of energy is used for all degrees of freedom, i.e. $1/2k_BT$ of energy per degree of freedom. The relative fluctuation of the instantaneous temperature is in the order of $1/\sqrt{N_f}$. For a system of the order of $10^2 \sim 10^3$ particles, the statistical fluctuation of the temperature is around $5 \sim 10\%$.

In the conventional NVE MD simulation, the total energy E, the total linear moment, the number of particles N and the volume V are kept constant. The ergodic hypothesis states the time averages obtained in a MD simulation are identical to ensemble averages computed in the microcanonical ensemble [113, 114]. A system is ergodic when every point in configuration space can be reached in a finite number of steps from any other point in the phase space. In practice, the ergodic hypothesis applies to systems with low free energy barriers. The general procedure for MD in the NVE ensemble is as follows

1. N molecules are randomly placed in the system. For zeolites, guest molecules can neither overlap with the zeolite framework, nor be placed inside the inaccessible regions.

2. Prior to the MD simulation, a MC simulation is performed in the NVT ensemble to generate a suitable initial configuration.

3. All molecules are assigned velocities from the Maxwell-Boltzmann distribution at the desirable temperature using Eq. 1.44. The total momentum of the system is set to zero. The NVE MD simulation is started to further equilibrate the system.

4. After equilibration, statistics are collected to compute dynamic or thermal properties of the system.

The MD method can be used to study the diffusion of guest molecules inside zeolites. In general, transport diffusion is the process in which an initial non-uniform concentration profile is smoothed by molecular motion. The typical diffusion coefficients calculated by equilibrium MD are the transport diffusivity and the self-diffusivity.

Self diffusion Self diffusion describes the diffusive motion of single molecules. The self-diffusion coefficient D_α^S in the direction α ($\alpha = x,y,z$) is computed by taking the slope of the mean square displacement over a long time.

$$D_\alpha^S = \frac{1}{2N} \lim_{\Delta t \to \infty} \frac{d}{dt} \left\langle \sum_{i=1}^{N} (r_{i,\alpha}(t+\Delta t) - r_{i,\alpha}(t))^2 \right\rangle \tag{1.45}$$

where N is the number of molecules. d is the dimensionality of the system, t is the time, and $r_{i,\alpha}$ is the center-of-mass of molecule i in the direction of α ($\alpha = x,y,z$).

Transport diffusion The transport diffusivity describes the transport of mass and the decay of concentration fluctuations. Two diffusion coefficients commonly used to describe the transport in zeolites are the collective or Maxwell-Stefan (MS) and Fickian diffusivities. For the single component adsorbed in a zeolite, the collective diffusion coefficient D_α^C in the direction α ($\alpha = x,y,z$) is given by

$$D_\alpha^C = \frac{1}{2N} \lim_{\Delta t \to \infty} \frac{d}{dt} \left\langle \left(\sum_{i=1}^{N} (r_{i,\alpha}(t+\Delta t) - r_{i,\alpha}(t)) \right)^2 \right\rangle \tag{1.46}$$

From Eqs. 1.45 and 1.46, one can see that the difference between the self and collective diffusivities is that the self diffusion considers the displacement for each single molecule while the collective calculate the displacement for all molecules as a whole. In an infinite dilute system ($N \to 0$) it follows $D^S = D^C$, while in most cases $D^S < D^C$ due to the reduced back-correlations [115].

MS diffusion for mixtures Before deriving the transport diffusion equations for mixtures, it is worthwhile to explain the fluxes and driving forces for transport diffusion in porous materials under non-equilibrium conditions. In general, there are three formulations of diffusion: the Fickian formulation, the Onsager formulation and the Maxwell-Stefan formulation.

In the Fickian formulation, the flux $\mathscr{N}$ of components in a mixture is proportional to the gradients of the loadings θ of all n components:

$$(\mathscr{N}) = -\rho [D^T](\nabla \theta) \tag{1.47}$$

where $\mathscr{N}$ is the molecular flux of an n-component mixture (in units of molecules per square meter per second), ρ the framework density in units of the number of unit cells per cubic meter, θ_i the loading of component i in molecules per unit cell, and D^T is the n by n matrix of Fick diffusivities in units of square meter per second.

In the Onsager approach, fluxes are expressed as a linear combination of the driving forces $\nabla\mu$:

$$(\mathscr{N}) = -\frac{\rho}{k_B T}[L](\nabla\mu) \tag{1.48}$$

The Onsager matrix $[L]$ is a square matrix with elements L_{ij}. As the Onsager reciprocal relations demand that the matrix $[L]$ is symmetric [35, 116], it is convenient to define a modified Onsager matrix $[\Delta]$, in which the fluxes follow from

$$(\mathscr{N}) = -\frac{\rho}{k_B T}[\Delta][\theta](\nabla\mu) \tag{1.49}$$

The diagonal elements of the n by n matrix $[\theta]$ are θ_1, θ_2, $\cdots$, θ_n while all off-diagonal elements equal zero. The Onsager matrix $[\Delta]$ can be directly calculated from the mean squared displacement via the following relation [35, 116]:

$$\Delta_{ij}^{\alpha} = \frac{1}{2N_j}\lim_{t\to\infty}\frac{d}{dt}\left\langle\left(\sum_{k=1}^{N_i}(\mathbf{r}_{k,i}^{\alpha}(t+\Delta t)-\mathbf{r}_{k,i}^{\alpha}(t))\right)\left(\sum_{l=1}^{N_j}(\mathbf{r}_{l,j}^{\alpha}(t+\Delta t)-\mathbf{r}_{l,j}^{\alpha}(t))\right)\right\rangle \tag{1.50}$$

where N_i and N_j represent the number of molecules of components i and j, respectively, $\mathbf{r}_{k,i}(t)$ the position of molecule k of the component i at any time t, and Δ_{ij}^{α} the Onsager coefficient of components components i and j in the direction of α ($\alpha = x,y,z$). In Eq. 1.48, the gradient in chemical potential is the driving force for diffusion. This driving force can be formulated in terms of the gradients in the occupation by introducing a matrix of thermodynamic factors Γ [35, 116]

$$\frac{\theta_i}{k_B T}\nabla\mu_i \equiv \sum_{j=1}^{n}\Gamma_{ij}\nabla\theta_j \quad \text{with} \quad \nabla_{ij} = \frac{\theta_i}{\theta_j}\frac{\partial \ln f_i}{\partial \ln \theta_j} \tag{1.51}$$

where f_i represents the fugacity of component i in the bulk phase. The terms ∇_{ij} can be calculated from the adsorption isotherms for n components [35, 116]. Using the Maxwell-Stefan theory, the following expression can be derived for diffusion of n components in a porous material:

$$-\rho\frac{\theta_i}{k_B T}\nabla\mu_i = \sum_{j=1,j\neq i}^{n}\frac{\theta_j\mathscr{N}_i - \theta_i\mathscr{N}_j}{\theta_j^s D_{ij}^{MS}} + \frac{\mathscr{N}_i}{D_i^{MS}} \tag{1.52}$$

where ρ the zeolite density in units of number of unit cells per cubic meter, θ_i the loading in molecules per unit cell, θ_i^s denoting the saturation loading of species i in the zeolite, n is the total number of diffusing species, $\nabla\mu_i$ the driving force acting on species i and k_B is the Boltzmann constant. In general, the left side of Eq. 1.52 represents the driving force for diffusion of component i while the right side stands for the friction experienced by component i. In Eq. 1.52, two types of MS diffusivities are defined, namely D_i^{MS} and D_{ij}^{MS}. For a single component, D_i^{MS} is identical to the corrected diffusivity in Eq. 1.46. For mixtures, the binary exchange coefficients D_{ij}^{MS} reflect correlation effects in zeolites, which can usually be neglected [35, 116]. The MS diffusivities can be rewritten into the Fickian formulation by

$$(\mathscr{N}) = -\rho[B]^{-1}[\Gamma](\nabla\theta) \tag{1.53}$$

where the elements of the matrix $[B]$ are

$$B_{ii} = \frac{1}{D_i^{MS}} + \sum_{j=1,j\neq i}^{n}\frac{\theta_j}{\theta_j^s D_{ij}^{MS}} \tag{1.54}$$

$$B_{ij} = -\frac{1}{\theta_j^s}\frac{\theta_i}{D_{ij}^{MS}} \tag{1.55}$$

Note that from Eqs. 1.49, 1.51 and 1.53, it follows that

$$[B]^{-1} = [\Delta] \tag{1.56}$$

This equation leads to the following expressions for the MS and binary exchange diffusion coefficients [35, 116]:

$$D_{ij}^{MS} = -\frac{1}{\theta_j^s}\frac{\theta_i}{B_{ij}} \tag{1.57}$$

$$D_i^{MS} = \frac{1}{B_{ii} - \sum_{j=1, j\neq i}^{n} \theta_j / (\theta_j^s D_{ij}^{MS})} \tag{1.58}$$

The directionally averaged diffusion coefficients are given by

$$D = \frac{D_x + D_y + D_z}{3} \tag{1.59}$$

The calculation of diffusion coefficients requires much memory and CPU power. The order-n algorithm [77, 117] allows us to calculate the mean square displacement at a low computational cost by using adjustable sampling frequencies. The order-n scheme is equally accurate as the conventional scheme but it saves memory use and CPU time [77, 117].

1.6 Scope of this thesis

The scope of this thesis is to study molecular aspects that are important for understanding the benzene alkylation reaction using zeolite catalysts, especially H-MOR. The first step is to clarify the role of non-framework cations in the adsorption and diffusion of guest molecules inside the MOR channel system. In chapter 2, the effect of the Al distribution in MOR-type zeolite is studied. This information is then used to construct Na-MOR lattices containing various amount of the non-framework cations. Simulations have been performed to investigate the effect of cations on the adsorption and diffusion behavior of guest molecules. During the simulation, severe difficulties arise when calculating the heat of adsorption using the conventional methods for zeolites with non-framework cations present. This is attributed to the strong Coulombic interaction. In chapter 3, an alternative method to efficiently calculate the heat of adsorption is presented based on biased interactions of guest molecules. In addition, the feasibility of handling strong Coulombic interactions using the Wolf method instead of the often used Ewald summation is reviewed for simulating the adsorption of guest molecules in zeolites containing non-framework cations.

The shape selectivity of zeolites mainly originates from its microporous structure. For reactions of benzene alkylation, several zeolite catalysts have been developed in industry. In chapter 4, GCMC simulations are used to investigate the adsorption selectivity of benzene in the benzene/propene mixtures for zeolites MOR, beta, zeolite Y and MCM-22.

In order to understand the porous structures of zeolite in detail, a simulation method is developed to directly compute the pore volume and the pore size distribution. This is presented in chapter 5.

Zeolites are usually treated by dealumination in order to improve their accessibility and activity. Besides the creation of the mesopores, dealumination may modify the micropore structure. As the shape selectivity of zeolites strongly depends on their micropores, it is thus important to investigate the change of the micropores of MOR during dealumination. In chapter 6, the dealumination process is modeled using Kinetic Monte Carlo. The influence of dealumination is studied with respects of the Al distribution, MOR crystallinity and the micro- and mesoporosity. In particular, experiments are, for the first time, combined with simulations aiming at a deep understanding of the effect of dealumination on the zeolite porosity, especially microporosity. Based on the detailed analysis of the dealuminated MOR, other zeolites are proposed as potential candidates for benzene alkylation.

2

Adsorption and Diffusion of Alkanes in Na-MOR: Modeling the Effect of the Aluminum Distribution

We investigated the adsorption and diffusion of alkanes in the sodium-exchanged zeolite Mordenite (Na-MOR) using molecular simulations. MOR-type zeolite consists of main channels (6.5×7 Å) oriented along the z crystallographic axis that are connected to small side pockets (3.4×4.8 Å). It is well known that the adsorption of alkanes in Na-MOR strongly depends on the precise location of the framework Al atoms, either in the main channel or in the side pockets (Calero and co-workers, Angew. Chem. Int. Ed., 2007, **46**, 276). We found that this effect can be characterized by a single order parameter: the number of framework Al in the main channel divided by the number of framework Al in the side pocket (M/S ratio). For any M/S ratio, the adsorption isotherm follows from a linear interpolation between reference isotherms. This enabled us to predict adsorption isotherms for any distribution of the Al framework atoms, or to estimate the M/S ratio for a given isotherm. We found that the same model can predict the effect of the M/S ratio on the self-diffusion coefficient, the Maxwell-Stefan diffusion coefficient, and the accessible micropore volume.

S. Ban, T.J.H. Vlugt, submitted.

2.1 Introduction

Mordenite (MOR-type zeolite) is an important catalyst in the petrochemical industry as it is used for the acid-catalyzed isomerization of alkanes and aromatics [53, 118]. For example, Pt/H-MOR is a suitable catalyst for the hydro-isomerization of linear alkanes to branched ones, even though slow intracrystalline transport hinders the catalytic performance to some extent [119]. Therefore, it is important to understand the adsorption and transport of hydrocarbon molecules in this zeolite [120]. The framework of MOR-type zeolite consists of main channels formed by large 12-membered rings with an elliptical shape of 6.7×7.0 Å oriented along the z crystallographic axis. Small side pockets are connected to these main channels by 8-membered rings (3.4×4.8 Å) that are oriented along the y crystallographic axis [121]. It was found that methane is the only hydrocarbon that can be adsorbed in the side pockets [122, 123].

In general, the structure of zeolites consists of covalently bonded TO_4 units, in which the framework T-atom is usually a silicon (Si) or an aluminum (Al) atom. To obey charge neutrality, the substitution of a silicon atom by an aluminum atom requires the presence of a non-framework cation (usually Na^+ or K^+) or a proton (H^+). It is well known that the adsorption of guest molecules in Na-MOR is significantly enhanced by non-framework Na^+ cations [124]. The positions of the non-framework cations in MOR-type zeolite are coupled to the positions of the framework Al atoms [125]. The *average* distribution of framework Al over the various T sites (labeled $T_1,\ldots,T_4$) in Na-MOR was obtained experimentally by detecting Brønsted acid sites [125–128]. It was found that the majority of Al is located at the T_3 and T_4 sites close to the the side pockets. Knowledge on the distribution of Al among T sites alone is not sufficient to obtain the *exact* individual positions of all framework Al atoms. Recently, Calero and co-workers used an elegant reversed engineering approach to identify the positions of the framework Al atoms in zeolites [129, 130]. For a fixed Si/Al ratio, this approach considers all possible distributions of Al in the unit cell of the zeolite. It was found that this approach correctly predicts the Al distribution in Na-MOR. These authors also found that for some zeolites, e.g. LTA, FAU, MFI, the precise positions of the framework Al atoms do not influence adsorption, while for other zeolites, e.g. MOR, FER, TON, the adsorption strongly depends on the positions of the framework Al atoms. For MOR-type zeolite, this is because non-framework Na^+ cations in the side pocket only have a weak interaction with adsorbed guest molecules in the main channel, while this interaction is much stronger for cations located in the main channel.

Many experimental and simulation studies have investigated the effect of non-framework cations on the diffusivity of guest molecules, particularly in MFI-type zeolite [131–134]. Fan *et al*. [132] used molecular dynamics simulations to study the diffusion of ethene in MFI-type zeolite. These authors found that the diffusion of ethene was slowed down from 2.7×10^{-9} m^2/s in silicalite framework to 1.6×10^{-9} m^2/s in ZSM-5 with four Al per one unit cell. Masuda *et al*. [134] studied the influence of acid sites on the diffusion of aromatics in MFI-type zeolite. This study revealed that at low temperatures, the diffusivity significantly decreased with an increasing number of acid sites, while the diffusion of aromatics was hardly affected by the acid sites at high temperatures. Leroy *et al*. [131] combined the Quasi-elastic neutron scattering technique with molecular simulations to study the diffusion of alkanes in MFI. These authors found that the diffusivity of octane in silicalite is four time larger than that in Na-ZSM-5. This result agreed well with their molecular dynamics simulations for MFI-type zeolite with two Na^+ per unit cell. In summary, previous studies show that diffusion of hydrocarbons is slowed down by non-framework cations. Therefore, it is important to know the effect of the Al distribution on this.

In this work, computer simulations were used to investigate the influence of the positions of framework Al on the adsorption and diffusion properties of Na-MOR in a more coarse-grained way. In our simulations, the Al distribution was described by a single order parameter: the M/S ratio, which is the ratio of the number of framework Al in the main channels (M) and in the side-pockets (S) in MOR-type framework (M/S ratio). The reasons for using this order parameter were: *(1)* the adsorption of guest molecules is only sensitive to the framework Al located in either the main channels or the side pockets, rather than the exact positions of framework Al atoms. *(2)* The Al distribution is a more accessible parameter for experiments than the distribution of non-framework Na^+.

This paper is organized as follows. In section 2.2, we briefly describe the construction of a Na-MOR supercell, as well as the simulation methods for computing adsorption isotherms, diffusivities and the accessible micropore volume. In section 2.3.1, the computed Na^+ distribution in MOR is compared with experiments. In section 2.3.2 we present an interpolation model to predict isotherms in Na-MOR for any M/S ratio, using two reference isotherms with a known M/S ratio. In section 2.3.3, we show that non-framework Na^+ cations seriously hinder the diffusion of alkanes in Na-MOR at low temperature, and that this effect is correctly described by our model. We show that our model is also applicable for calculating the micropore volume of Na-MOR (section 2.3.4). Our findings are summarized in section 2.4.

2.2 Simulation methods

2.2.1 Constructing the Na-MOR lattice

Zeolite Na-MOR consists of Na, Si, Al and O atoms with the composition $Na_xAl_xSi_{48-x}O_{96}$. Natural Mordenite has a Si/Al ratio of approximately $4.3 \sim 6.0$, so $x \approx 8$ [126]. Demuth *et al.* [135] pointed out that the most common space group for MOR-type zeolite is *Cmcm* with the exception of dehydrated protonated MOR which has space group *Pbcn*. Macedonia *et al.* [136] showed that differences in adsorption isotherms between space groups *Cmcm* and *Pbcn* are negligible. Therefore, in this paper we restricted ourselves to the Na-MOR lattice with a *Cmcm* symmetry. The dimensions of the MOR unit cell are $18.094\text{Å} \times 20.516\text{Å} \times 7.524\text{Å}$ with $\alpha = \beta = \gamma = 90^\circ$. Each unit cell contains four different tetrahedral sites (T_1,...,T_4) for Si and Al framework atoms, and ten different oxygen sites (O_1,...,O_{10}) [1]. The T_3 sites are located in the side-pocket, while T_1, T_2 and T_4 are located in the main channel, see Fig 2.1(a). Alberti *et al.* [126] derived the Al distribution over the four T sites in natural Na-MOR from XRD measurements. This is also expected to be applicable to synthetic Na-MOR and H-MOR.

In this work, we constructed large supercells of MOR-type zeolite consisting of $2 \times 2 \times 4$ unit cells. Starting from an all-silica supercell, Si framework atoms are randomly substituted by Al in such a way that *(1)* the Löwenstein rule is obeyed, and *(2)* the relative Al content of each T site corresponds to the given M/S ratio. As a result, many Na-MOR supercells could be generated with the same Si/Al ratio, but with different positions of the framework Al. We will show that the properties of these supercells are nearly identical as the relative Al content of the T sites in the main channel and side pocket is identical for these supercells. Computed properties were then averaged over 5-10 supercells.

2.2.2 Computing adsorption isotherms

Adsorption isotherms were computed by using Configurational-Bias Monte Carlo [77, 99, 137] simulations in grand-canonical ensemble (GCMC) [77, 81, 84, 138]. Interactions between guest molecules, the zeolite framework and the non-framework cations were described by Lennard-Jones interactions. In addition, electrostatic interactions between the non-framework Na^+ cations and the framework were included. All force field parameters were taken from the work of Calero *et al.* [82]. The Ewald summation was used to compute electrostatic interactions. A typical simulation consisted of 3×10^6 Monte Carlo cycles. In each cycle, trial moves were chosen at random with a fixed probability: translation of a guest molecule or non-framework cation (15%), rotation of a guest molecule (15%), exchange of a guest molecule with a particle reservoir (55%), and partial regrowth of a guest molecule (15%). The number of trial moves in each cycle was equal to the number of adsorbed guest molecules with a minimum of 20. The number of Na^+ atoms in Na-MOR was constant during the simulations. For the simulation of adsorption, the zeolite framework was kept rigid and the non-framework cations were mobile. For the systems considered here, including framework flexibility usually results in a negligible deviation of adsorption isotherms [72]. For more details on these simulations, we refer the reader to Refs. [81, 82, 84].

2.2.3 Computing diffusivities of guest molecules

Molecular Dynamics simulations [112] were used to calculate the self- and Maxwell-Stefan diffusion coefficients of adsorbed guest molecules in MOR-type zeolite. We used the velocity Verlet algorithm [139] with a time step of 0.5 fs. The temperature was controlled by a Nosé-Hoover thermostat [77]. The initial configuration of guest molecules was taken from the final configuration of a Monte Carlo simulation in the NVT ensemble. To avoid single-file diffusion, each main channel of MOR-type zeolite contained only a single guest molecule. For simplicity, we used a rigid framework. Non-framework cations were allowed to move freely in the zeolite. The self- (D^{self}) and Maxwell-Stefan diffusion coefficients (D^{MS}) of a single component adsorbed in a zeolite were computed from particle displacements:

$$D_{\alpha}^{\text{self}} = \frac{1}{2n} \lim_{\Delta t \to \infty} \frac{1}{\Delta t} \left\langle \left(\sum_{i=1}^{n} (r_{i,\alpha}(t+\Delta t) - r_{i,\alpha}(t))^2 \right) \right\rangle \tag{2.1}$$

$$D_{\alpha}^{\text{MS}} = \frac{1}{2n} \lim_{\Delta t \to \infty} \frac{1}{\Delta t} \left\langle \left(\sum_{i=1}^{n} (r_{i,\alpha}(t+\Delta t) - r_{i,\alpha}(t)) \right)^2 \right\rangle \tag{2.2}$$

in which α is the direction of diffusion, n is the number of adsorbed guest molecules and $r_i(t)$ is the position of molecule i at time t [17, 35, 115]. For MOR-type zeolite, only diffusion in the main channel (z direction) was taken into account, i.e. $\alpha = z$. In practice, the mean square displacement in Eqs. 6.1,6.2 was computed using an order-n algorithm [77, 115, 117].

2.2.4 Pore size distribution

In this work, the pore size of a certain cavity or channel was defined as the maximum diameter of a sphere that can be located in there. This definition is applicable to pores with an arbitrary shape. For cylindrical or slit pores, our definition is identical to the IUPAC definition [140]. Using this definition, the pore size distribution was computed from the coordinates of the framework atoms using the following algorithm [141]: *(1)* a three-dimensional grid with a small spacing is constructed. We typically use a grid size of 0.1 Å (in each direction). *(2)* a spherical test particle is positioned at a random position in the zeolite. The radius of this particle is chosen as the minimum distance between the center of the particle and any of the zeolite framework atoms, minus the radius of the closest framework atom. The radius of an oxygen framework atom is 1.35 Å, and 0.99 Å for Na^+ [1]. Tetrahedral atoms, e.g. Si, Al, are not considered as for most zeolites they are well screened by adjacent oxygen atoms [142]. *(3)* The diameter of the test particle is recorded for all grid points that are inside the spherical particle. *(4)* This procedure is repeated many times. We found that the number of test spheres should be at least 100 times the number of grid points. For each grid point, the maximum recorded diameter is computed and this quantity is defined as the local pore size of a specific grid point. The simulation stops when the local pore size of all grid points is converged. *(5)* The fraction of pores with a diameter between r and $r+\Delta r$ (pore size distribution) is equal to the fraction of grid point with a maximum diameter between r and $r+\Delta r$. Using our calculated pore size distribution, the micropore volume was calculated by integrating the pore size distribution from 4.5 Å to 20 Å. For more details, we refer the reader to Ref. [141].

2.3 Results and discussion

2.3.1 Na^+ distribution

Non-framework Na^+ cations interact with the framework Al through Lennard-Jones and long range Coulombic interactions. As a consequence, Na^+ cations are not directly bonded to framework Al atoms. Experiments on dehydrated Na-MOR crystals [121, 143, 145, 147] identified three favorable locations for non-framework Na^+: in the center of eight-membered rings that run parallel to

Table 2.1: Comparison of the Na^+ occupancies between experiments and our simulations. [a]Schlenker *et al.* [121]. [b]Devautour *et al.* [143]. [c]Coughlan *et al.* [144, 145]. [d]Tyburce *et al.* [146]. The Na^+ occupancy was averaged over five supercells. Note that the differences in occupancy between the supercells were very small.

	Si/Al	site A	site D	site E
experiment[a]	5.7	43%	36%	21%
experiment[b]	5.7	53%	34%	13%
experiment[c]	5	49%	32%	19%
simulation[d]	5	50%	38%	12%
this work	5.0	40.2%	35.5%	20.9%
this work	5.5	40.1%	35.3%	20.9%

the main channels (site A), in the main channel at the entrance of the side pocket (site D), and in the main channel far away from the side pocket (site E), see Fig. 2.1(a). Our simulations showed the same adsorption sites for Na non-framework cations, see Fig. 2.1(b). The Na^+ occupancies at these sites have been computed for natural Na-MOR with Si/Al= 5 and 5.5, respectively. Table 2.1 shows that the computed Na^+ occupancies at these sites agree very well with the available experiments. For different supercells with an identical distribution of Al over the T sites, we found that the occupancy of Na^+ at the three sites is nearly identical. The corresponding radial distribution functions for Na^+-Na^+ interactions are very similar as they all show peaks at distances of 4.3 Å, 6.2 Å, 10.1 Å and 14 Å, see Fig. 2.2.

2.3.2 Prediction of adsorption isotherms

Na-MOR has two main adsorption sites for alkanes, the large main channels and the smaller side pockets. Methane is the only alkane that can access the side pockets [122, 123]. The side pockets are also accessible for non-framework Na^+ cations. It is natural to divide the non-framework

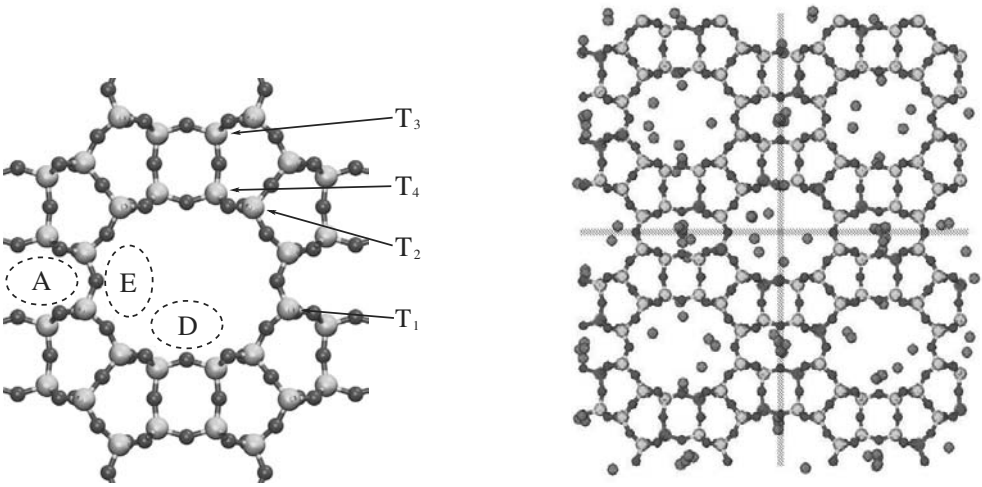

Figure 2.1: (a) The preferential sites A, D and E for non-framework Na^+ cations in Na-MOR. The colors are: red for O and yellow for Si and Al. The four T-sites T_1, T_2, T_3 and T_4 are shown as well. (b) Typical snapshot of Na-MOR with Si/Al= 5 for a supercell consisting of $2 \times 2 \times 4$ unit cells at 300 K. The colors are: red for O, cyan for Na^+, yellow for Si and black for Al.

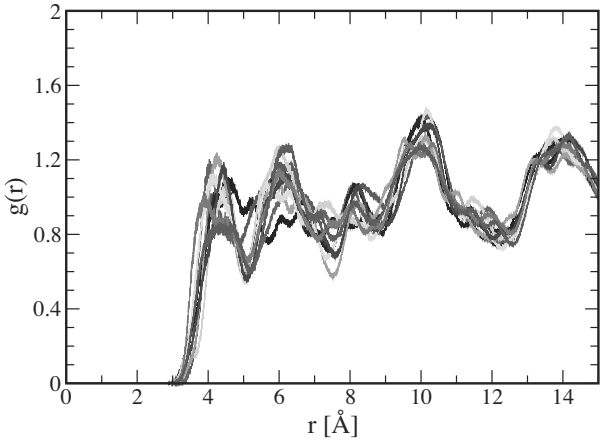

Figure 2.2: Radial distribution functions for Na^+-Na^+ interactions for ten supercells with the same Al distribution (Si/Al=5), see section 2.2.1.

Na^+ cations into two groups: Na^+ in the main channels (denoted by Na_M^+) and Na^+ in the side pockets (denoted by Na_S^+). Na_M^+ corresponds to the Na^+ cations at site D and at site E, while Na_S^+ corresponds to Na^+ at site A. The Na_M^+ cations interact more strongly with alkanes absorbed in the main channel, as they are more close by. A convenient order parameter to characterize the Na^+ distribution is the Al M/S ratio, which is the ratio of the number of the framework Al in main channels and in the side pockets. The reason for this is that due to the strong interactions between Al and Na^+, the distribution of the Na^+ cations approximately follows that of the framework Al. The difference of the adsorption properties between different Na-MOR supercells with the same Al M/S ratio was found to be small in our simulations. Al framework atoms at the crystallographic site T_3 are considered to be in the side pocket, while Al atoms at T_1, T_2 and T_4 are considered to be in the main channel, see Fig. 2.1(a). The same classification was previously used by IR spectroscopy experiments of probe molecules in MOR-type zeolite [148]. This technique is used to locate Brnsted acid sites in H-MOR. We expect that the Al distribution in Na-MOR is the same as in H-MOR, as H-MOR is usually obtained by exchanging Na^+ with H^+ [149].

To model the adsorption behavior of alkanes in Na-MOR as a function of the M/S ratio (Al content in the main channel divided by the Al content in the side pocket, here denoted by r) we constructed the following model. The total number of Al atoms per unit cell is denoted by n, while n_M and n_S are the number of Al atoms per unit cell in main channels and side pockets, respectively. Of course,

$$n = n_M + n_S \tag{2.3}$$

and we define the ratio r by

$$r = \frac{n_M}{n_S} \tag{2.4}$$

From this it directly follows that

$$n_M = n\frac{r}{r+1} \tag{2.5}$$

$$n_S = n\frac{1}{r+1} \tag{2.6}$$

Our key assumption is that the loading of guest molecules at pressure P (here denoted by $I(P)$) is a linear function of n_M and n_S

$$\begin{aligned} I(P) &= I_0(P) + \alpha_M(P) n_M + \alpha_S(P) n_S \\ &= I_0(P) + \frac{n}{r+1}\left[\alpha_M(P) r + \alpha_S(P)\right] \end{aligned} \tag{2.7}$$

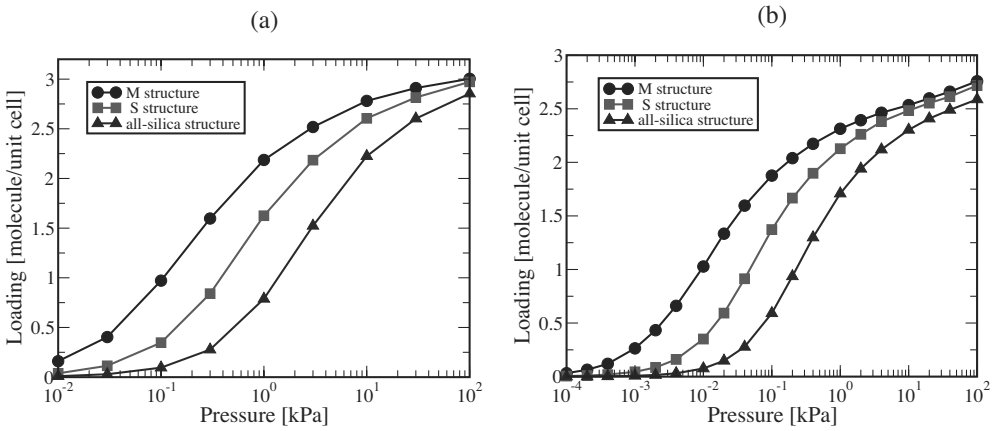

Figure 2.3: Adsorption isotherms of propane (a) and butane (b) in Na-MOR at 300 K for Si/Al= 11. The M and S structures are shown, as well as the isotherm for the all-silica structure. Each isotherm is the average over three supercells with the same M/S ratio. The error bars indicate the differences between these supercells. For each supercell, the error in the computed loading is much smaller than the symbol size.

where $\alpha_M(P)$ and $\alpha_S(P)$ are pressure-dependent constants and $I_0(P)$ is the loading of guest molecules for all-silica MOR at pressure P. The maximum number of Al at the T_3 sites is four Al atoms per unit cell ($n_S \leq 4$), which is much lower than the maximum possible number of Al in the main channel. For a given total content of framework Al atoms, there are two extreme situations: *(1)* the M structure, i.e. all Al is located in main channels ($n_S = 0$, $n_M = n$, the corresponding adsorption isotherm is denoted by $I_M(P)$) and *(2)* the S structure, where the side pockets are fully loaded with Al, and the remaining Al is located in the main channel (adsorption isotherm denoted by $I_S(P)$). This leads to

$$I_M(P) = I_0(P) + \alpha_M(P)n \tag{2.8}$$

and

$$I_S(P) = \begin{cases} I_0(P) + \alpha_S(P)n & \text{for } n \leq 4 \\ I_0(P) + 4\alpha_S(P) + (n-4)\alpha_M(P) & \text{for } n > 4 \end{cases} \tag{2.9}$$

By eliminating $\alpha_M(P)$ and $\alpha_S(P)$ we obtain

$$I(P) = \begin{cases} \frac{r}{r+1} I_M(P) + \frac{1}{r+1} I_S(P) & \text{for } n \leq 4 \\ \frac{4r-n+4}{4(r+1)} I_M(P) + \frac{n}{4(r+1)} I_S(P) & \text{for } n > 4 \end{cases} \tag{2.10}$$

When the Si/Al ratio is larger than 11 (i.e. $n \leq 4$), the weight factors of $I_M(P)$ and $I_S(P)$ in Eq. 2.10 are simply the fractions of framework Al at the sites M and S.

To test the prediction of Eq. 2.10, we computed adsorption isotherms of propane and butane in Na-MOR. These molecules are exclusively adsorbed in the main channels. Fig. 2.3 shows the computed adsorption isotherms I_M and I_S for Na-MOR with four Al per unit cell. Both isotherms significantly differ from the one for an all-silica structure. As expected, the adsorption isotherm strongly depends on the positions of the framework Al atoms and the differences between isotherms of different supercells are small. At a given pressure, the adsorbed amount for the S structure is always lower than that for the M structure due to the increased average distance between the guest molecules and the non-framework Na^+ cations.

Figs. 2.4 and 2.5 show that the prediction of Eq. 2.10 is excellent. This result is useful in two ways: First, the adsorption isotherm for an arbitrary M/S ratio can be predicted by linear interpolation between two reference isotherms (for which we know the M/S ratio). Second, the M/S ratio in

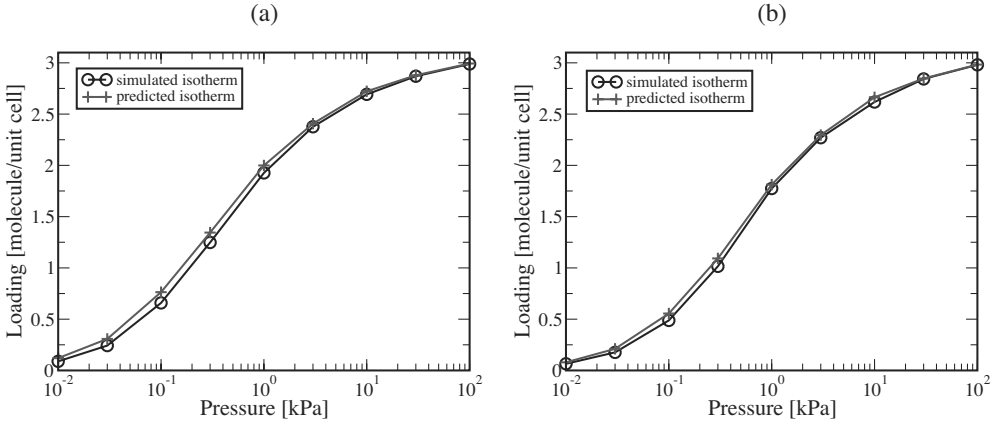

Figure 2.4: Linear interpolation of adsorption isotherms for propane in Na-MOR with Si/Al=11 at 300 K. The predicted isotherm using Eq. 2.10 was compared to the computed isotherm at the same Al M/S ratio. (a) Al M/S ratio 2 : 1, (b) Al M/S ratio 1 : 2.

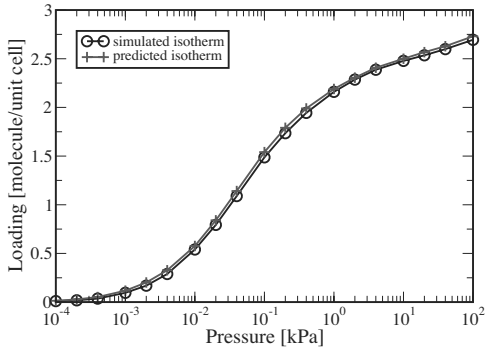

Figure 2.5: Linear interpolation of adsorption isotherms for butane in Na-MOR with Si/Al=11 at 300 K. The predicted isotherm using Eq. 2.10 was compared to the computed isotherm at the same Al M/S ratio 1 : 2.

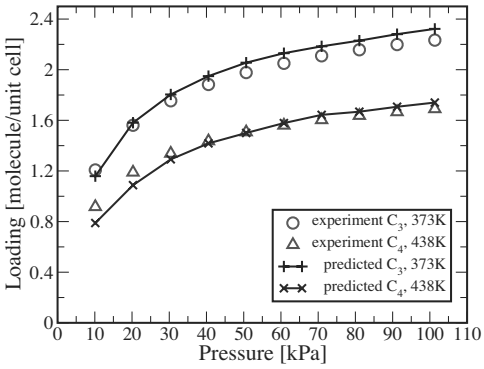

Figure 2.6: Comparison of the predicted isotherms (Eq. 2.10) with experimental data [123] for propane and butane in Na-MOR with Si/Al= 19.75 at 373 K and 438 K. The estimated Al M/S ratio was 3 : 1 for this system.

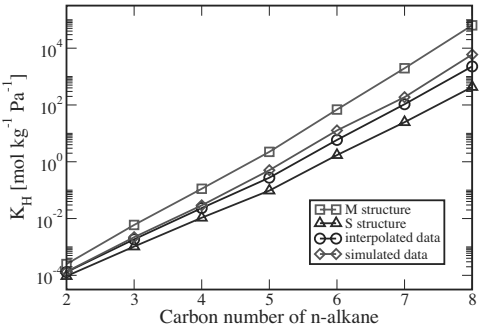

Figure 2.7: Linear interpolation of the Henry coefficients of n-alkanes in Na-MOR with Si/Al=11 at 300 K. The error bars are much smaller than the symbols.

a Na-MOR sample can be estimated by fitting a measured isotherm to two reference isotherms. As an example, we estimated an M/S ratio of 3 : 1 from experimental adsorption isotherms of propane and butane in Fig. 2.6. This estimated ratio is close to the ratio of 2 : 1 proposed by Alberti *et al.* [126].

In Fig. 2.7, it is shown that our interpolation model is able to accurately predict the Henry coefficients of n-alkanes with $2 \sim 5$ carbon atoms. For longer n-alkanes, small differences appeared between the computed and predicted Henry coefficients. The reason for this is that longer chains will have interactions with more Na^+ cations at the same time, leading to non-linear effects.

2.3.3 Prediction of diffusivities

The computed and predicted diffusivities of alkanes in Na-MOR for various Si/Al ratios are shown in Table 2.2. The simulations were performed for propane and hexane diffusing in the all-silica MOR and Na-MOR containing 2 or 8 Na^+ cations at 300K and 600K, respectively. As each main channel contains a single alkane molecule only, it is expected that the Maxwell-Stefan and self diffusivities do not differ very much. It can be seen from Table 2.2 that both the self- and Maxwell-Stefan diffusivities decrease as a function of the Na^+ concentration irrespective of the temperature and alkane chain length. This is in line with the results from Leroy *et al.* [131]. Note that the differences of the calculated diffusivities were about 15% for supercells with the same Al

Table 2.2: Self- and Maxwell-Stefan diffusion coefficients of propane and hexane in all-silica MOR and Na-MOR with Si/Al=5,23 at 300K and 600K. Each main channel contained a single alkane molecule. Self- and Maxwell-Stefan diffusivities are denoted by D^{self} and D^{MS} in units of 10^{-8} m^2/s, respectively. The diffusion coefficients in Na-MOR were obtained by averaging over ten supercells with the same M/S ratio. The differences between supercells are approximately 15%. For each supercell, the error in the computed diffusivity was around 20% for D^{MS} and 10% for D^{self}. For all-silica MOR, the error in the computed diffusion coefficients was smaller than 1%.

	Si/Al	C_3 at 300K	C_6 at 300K	C_3 at 600K	C_6 at 600K
D^{self}	∞	5.5	7.0	12.3	13.1
D^{self}	23	2.5	1.6	7.0	5.7
D^{self}	5	1.8	0.9	5.5	3.6
D^{MS}	∞	5.5	7.0	11.6	12.8
D^{MS}	23	2.3	1.4	6.9	5.5
D^{MS}	5	1.8	0.9	5.3	3.5

distribution. For each supercell, the simulation error is about 20% for D^{MS} and 10% for D^{self}. These errors are much smaller than the difference of the diffusivities for Na-MOR with different Si/Al ratios. Therefore we can conclude that the diffusion of alkanes is slowed down by the non-framework cations of Na-MOR.

The self- and Maxwell-Stefan diffusivities were computed for propane in Na-MOR with Si/Al= 11 at 300K and 600K at a loading of one propane per main channel, see Table 2.3. As the loading is quite low, the self- and Maxwell-Stefan diffusivities are almost equal. However, the diffusivity of propane in the S structure is more than twice as large as in the M structure. The reason for this is that because of the strong interactions between propane and Na^+, the Na^+ ions in the main channels will slow down the diffusion of propane significantly. Therefore, $D_M < D_{M/S=2:1} < D_{M/S=1:2} < D_S$. In the same spirit as Eq. 2.10, we predicted the self- and Maxwell-Stefan diffusivities for M/S=2:1 and M/S=1:2, based on the computed diffusivities D_M and D_S:

$$D = \begin{cases} \frac{r}{r+1} D_M + \frac{1}{r+1} D_S & \text{for } n \leq 4 \\ \frac{4r-n+4}{4(r+1)} D_M + \frac{n}{4(r+1)} D_S & \text{for } n > 4 \end{cases} \tag{2.11}$$

In this equation, D is the predicted isotherm and D_M and D_S are the two reference isotherms. The predicted diffusivities are very close to the computed ones. Differences of calculated diffusivities are about 12% for the supercells with the same Al M/S ratio. For each supercell, the simulation error is about 20% for D^{MS} and 5% for D^{self}. These errors are much smaller than the difference of the diffusivities for Na-MOR with different Al M/S ratios. Therefore we can conclude that the interpolation scheme is able to predict self- and Maxwell-Stefan diffusivities in Na-MOR.

2.3.4 Prediction of the micropore volume

The micropore volume of Na-MOR for different M/S ratios is shown in Table 6.11. As the micropore volume was calculated from pores in the range of $4.5 \sim 20$ Å, the main contribution to the micropore volume originates from the main channels. Therefore, when all the non-framework Na^+ is located in the main channel, the micropore volume decreases. This leads to the following prediction: $V_M < V_{M/S=2:1} < V_{M/S=1:2} < V_S$. For a given M/S ratio, the micropore volume can be computed using

$$V = \begin{cases} \frac{r}{r+1} V_M + \frac{1}{r+1} V_S & \text{for } n \leq 4 \\ \frac{4r-n+4}{4(r+1)} V_M + \frac{n}{4(r+1)} V_S & \text{for } n > 4 \end{cases} \tag{2.12}$$

Table 6.11 shows that the predicted micropore volumes are in good agreement with the computed ones. The differences in micropore volume are 0.5% for supercells with the same M/S ratio. The

Table 2.3: Interpolation of propane and hexane diffusivities in Na-MOR with Si/Al=11 at 300K and 600K respectively. Each main channel contained a single alkane molecule. Self- and Maxwell-Stefan diffusivities were denoted by D^{self} and D^{MS} in units of 10^{-8} m^2/s. D_M and D_S are the computed diffusivities for the M and S structure, see section 2.3.2. All reported values were obtained by averaging over ten supercells with the same M/S ratio. The differences between supercells are approximately 12%. For each supercell, the error in the estimated diffusivity was approximately 20% for D^{MS} and 5% for D^{self}.

C_3 (300 K)		D_M	D_S	$D_{M/S=1:2}$	$D_{M/S=2:1}$
simulated	D^{self}	1.4	2.8	2.0	1.6
predicted	D^{self}	n.a.	n.a.	2.3	1.9
simulated	D^{MS}	1.3	3.0	2.2	1.4
predicted	D^{MS}	n.a.	n.a.	2.4	1.9

C_6 (600 K)		D_M	D_S	$D_{M/S=1:2}$	$D_{M/S=2:1}$
simulated	D^{self}	3.1	5.1	4.5	3.7
predicted	D^{self}	n.a.	n.a.	4.4	3.8
simulated	D^{MS}	2.9	5.1	4.6	3.5
predicted	D^{MS}	n.a.	n.a.	4.4	3.6

Table 2.4: Interpolation of the micropore volume (V) of Na-MOR with Si/Al= 11 in units of ml/g. The notation is the same as in table 2.3. All values were obtained by averaging over ten supercells with the same Al M/S ratio. The differences of the micropore volumes were 0.5% for the ten supercells with the same Al M/S ratio. The simulation error of the micropore volume for each supercell was approximately 0.2%.

	V_M	V_S	$V_{M/S=1:2}$	$V_{M/S=2:1}$
simulated	0.1816	0.1934	0.1874	0.1855
predicted	n.a.	n.a.	0.1894	0.1855

error in the computed micropore volume for each supercell is about 0.2%. These errors are more than one order of magnitude smaller than the difference in the micropore volume between the M- and S structure. Therefore we can conclude that the interpolation scheme works also well for the prediction of the accessible micropore volume in Na-MOR.

2.4 Conclusions

We presented a simple interpolation model to predict the effect of the framework Al distribution on the adsorption isotherms and diffusivities of alkanes in Na-MOR, as well as the micropore volume. The key parameter is the Al M/S ratio, which is the ratio between the number of Al atoms in the side pockets (T_3 sites) and the main channels (T_1, T_2 and T_4 sites). Our model predictions match the computed values very well.

3

Computing the heat of adsorption using molecular simulations: the effect of strong Coulombic interactions

Molecular simulations are an important tool for the study of adsorption of hydrocarbons in nanoporous materials such as zeolites. The heat of adsorption is an important thermodynamic quantity that can be measured both in experiments and molecular simulations, and therefore it is often used to investigate the quality of a force field for a certain guest-host (*g*-*h*) system. In molecular simulations, the heat of adsorption in zeolites is often computed using either of the following methods: *(1)* using the Clausius-Clapeyron equation, which requires the partial derivative of the pressure with respect to temperature at constant loading, *(2)* using the energy difference between the host with and without a single guest molecule present, and *(3)* from energy/particle fluctuations in the grand-canonical ensemble. To calculate the heat of adsorption from experiments (besides direct calorimetry), only the first method is usually applicable. *Although the computation of the heat of adsorption is straightforward for all-silica zeolites, severe difficulties arise when applying the conventional methods to systems with non-framework cations present. The reason for this is that these non-framework cations have very strong Coulombic interactions with the zeolite*. We will present an alternative method based on biased interactions of guest molecules that suffers less from these difficulties. This method requires only a single simulation of the host structure. In addition, we will review some of the other important issues concerning the handling of these strong Coulombic interactions in simulating the adsorption of guest molecules. It turns out that the recently proposed Wolf method (*J. Chem. Phys. (1999), 110, 8254*) performs poorly for zeolites as a large cut-off radius is needed for convergence.

T.J.H. Vlugt, E. García-Pérez, D. Dubbeldam, S. Ban, S. Calero, *Journal of Chemical Theory and Computation* Volume 4 (2008), pages 1107-1118

3.1 Introduction

Zeolites are microporous crystalline materials with pores of about the same size of a small molecule like water or n-hexane. The structure of a zeolite consists of covalently bonded TO_4 units, in which the T-atom is usually a silicon (Si) or aluminum (Al) atom. To obey charge neutrality, the substitution of a silicon atom by an aluminum atom requires the presence of a non-framework cation (usually Na^+ or K^+) or a proton (H^+). There are approximately 170 different zeolite framework types that have been synthesized [1]. Zeolitic materials are widely used as water softener, selective adsorber and catalyst for hydrocarbon conversions (catalytic cracking and isomerization).

As molecular simulations can provide a fundamental understanding of processes and properties at the molecular scale, in the past few years this type of simulations have become an important tool for investigating the adsorption properties of small guest (g) molecules in zeolite hosts (h). As guest-host interactions are often dominated by the dispersive interactions of the oxygen atoms with the guest [150], classical force fields based on Lennard-Jones (LJ) interactions have become very popular in this field of research [78, 84, 151–156]. Recently, it has been shown that an optimal parametrization can lead to united atom force fields for alkanes that are transferable to many all-silica zeolite framework types [81, 157, 158]. This transferability is often tested by a comparison between simulations and experimental adsorption data that had not been used to calibrate the force field parameters [158].

When non-framework cations are present in the framework, strong electrostatic interactions between the non-framework cations and the framework atoms (Si, Al, O) have to be included for a correct description of the system. Although the Ewald summation with tin foil boundary conditions is often used [77], the so-called Wolf method has been introduced recently as a pairwise alternative [89, 159]. The strong interaction between the non-framework cations and hydrocarbons lead to an enormous effect on adsorption properties [82, 160–162].

In this work, we will consider the effect of strong electrostatic interactions between the framework and the non-framework cations or adsorbates on the computation of the heat of adsorption. This quantity describes the change in enthalpy when a molecule is transferred from the gas phase into the pores of a zeolite. In experiments, the heat of adsorption is usually computed using the Clausius-Clapeyron equation [163] or direct calorimetry experiments [164] while in molecular simulations this quantity is usually calculated directly from the total energy of the simulated system [78, 84, 165]. However, we will show that a direct computation using energy differences results in very inaccurate results for zeolites with strongly bound non-framework cations.

This paper is organized as follows. In section 3.2 we briefly review the various schemes to compute the heat of adsorption in molecular simulations and we will explain the advantages and disadvantages of each method. In particular, we will show that a direct calculation of the heat of adsorption using energy differences may lead to problems for systems with strongly interacting non-framework cations. We will introduce an alternative method based on biased insertions that does not suffer from these difficulties. Results of the various methods for a typical system (described in section 3.3) are presented in section 3.4. In section 3.5 we discuss some of the other important issues for handing the Coulombic interactions in these systems and show why the Ewald summation is here preferable over the recently proposed Wolf method. Our findings are summarized in section 3.6.

3.2 Calculating the heat of adsorption

In the remainder of this paper, we will denote the zeolite *and* the included non-framework cations as the "host" (h). The scaled positions of all the atoms that belong to the host are denoted by the vector $\mathbf{h}$. The adsorbate is denoted as "guest" (g) and its conformation is denoted by $\mathbf{g}$. In most of the derivations in this work, the heat of adsorption is calculated in molecular units, i.e. in J (or kJ) per molecule instead of the often used J per mol.

Following Wood, Panagiotopoulos and Rowlinson [163], the heat of adsorption q (or enthalpy

of adsorption -ΔH) *at loading* θ is defined using the famous Clausius-Clapeyron equation

$$-q = \Delta H = k_B \left(\frac{\partial \ln [P/P_0]}{\partial T^{-1}} \right)_{\theta=\text{constant}} = \left(\frac{\partial \ln [P/P_0]}{\partial \beta} \right)_{\theta=\text{constant}} \tag{3.1}$$

where P is the pressure, P_0 an arbitrary reference pressure, T the absolute temperature, θ the loading of guest molecules, $k_B = N_{\text{av}}/R$ is the Boltzmann constant, R is the gas constant, N_{av} is Avogadro's number, and $\beta = 1/(k_B T)$. For an in-depth review of the thermodynamic definition of the heat of adsorption we refer the reader to Ref. [166]. To compute the heat of adsorption at loading θ directly from this equation, one needs the adsorption isotherm $\theta(P)$ for various temperatures T. At sufficiently low loadings, the gas phase will behave as an ideal gas and the adsorption isotherm will become a linear function:

$$K_H = \frac{\theta}{VP} \tag{3.2}$$

in which V is the volume of the host and K_H is the so-called Henry coefficient (in units of molecules per unit of host volume per unit of pressure). The heat of adsorption *at low loading* then becomes

$$-q = \Delta H = -\frac{\partial \ln [K_H/K_{H0}]}{\partial \beta} \tag{3.3}$$

in which K_{H0} is an arbitrary constant (that has the same units as K_H). In molecular simulations, the most convenient way to calculate the Henry coefficient is using Widom's test particle method [77, 87, 104, 167]:

$$K_H = \beta \times \exp[-\beta \mu_{\text{ex}}] = \beta \times \frac{\langle \exp[-\beta u^+] \rangle_H}{\left\langle \exp[-\beta u^+_{IG}] \right\rangle_{EB}} \tag{3.4}$$

in which μ_{ex} is the excess chemical potential of the guest in the zeolite, u^+ is the energy of a test (guest) molecule inserted at a random position in the zeolite, and u^+_{IG} is the energy of a test (guest) molecule inserted at a random position in an empty box without the presence of the host (often referred to as an isolated chain). The brackets $\langle \cdots \rangle_H$ denote an average in the NVT ensemble over all conformations of the host (and positions of the test particle) and the brackets $\langle \cdots \rangle_{EB}$ denote an ensemble average for a test chain in an *empty* simulation box (ideal gas phase). For chain molecules like alkanes, it is well known that insertion of a test chain at a random position in the zeolite nearly always results in overlaps with zeolite atoms, and therefore the sampling statistics of the average $\langle \exp[-\beta u^+] \rangle_H$ will be extremely poor [165]. For chains that are not too long (< 50 monomers) it is convenient to use the Configurational-bias Monte Carlo (CBMC) method [77, 98, 99, 137, 168] to insert test chains. In this case, the Henry coefficient is computed from [165]

$$K_H = \beta \times \frac{\langle W \rangle_H}{\langle W_{IG} \rangle_{EB}} \tag{3.5}$$

in which $\langle W \rangle_H$ is the average Rosenbluth weight of a test chain in the host and $\langle W_{IG} \rangle_{EB}$ is the average Rosenbluth weight of an isolated test chain in an empty box.

Calculating the heat of adsorption *at low loading* directly using either Eq. 3.1 or Eqs. 3.3, 3.4 requires several simulations or adsorption experiments at different temperatures and the final answer must be computed by a numerical differentiation with respect to $1/T$. As the accuracy of such a numerical differentiation strongly depends on the accuracy of the individual simulations [169], many long simulations are required to obtain an accurate value for the heat of adsorption. Therefore, two alternative methods to compute the heat of adsorption are often used in molecular simulations:

- From energy differences computed in the canonical (NVT) ensemble [163, 165]

$$-q = \Delta H = \langle U_1 \rangle_1 - \langle U_0 \rangle_0 - \langle U_g \rangle - \frac{1}{\beta} \tag{3.6}$$

in which U_N is the total energy of a host with N guest molecules present, $\langle\cdots\rangle_X$ refers to an ensemble average at constant V,T and X guest molecules, and $\langle U_g\rangle$ is the average energy of an isolated guest molecule (without the host present). The average $\langle U_g\rangle$ for a certain guest molecule only depends on temperature and needs to be calculated only once. Later, we will see that for zeolites with non-framework cations, the difference $|\langle U_1\rangle_1 - \langle U_0\rangle_0|$ is very small compared to either $\langle U_0\rangle_0$ or $\langle U_1\rangle_1$. Therefore, a direct computation of both $\langle U_0\rangle_0$ and $\langle U_1\rangle_1$ can lead to a very inaccurate estimate of ΔH. *Note that Eq. 3.6 only applies to the heat of adsorption at zero coverage and that it assumes ideal gas behavior.*

- From energy/particle fluctuations in the grand-canonical (μVT) ensemble [166]. We can approximate the change in potential energy upon adsorption of a single guest molecule [166]:

$$\langle U_{N+1}\rangle_{N+1} - \langle U_N\rangle_N \approx \left(\frac{\partial \langle U\rangle_\mu}{\partial \langle N\rangle_\mu}\right)_\beta = \frac{\left(\frac{\partial \langle U\rangle_\mu}{\partial \mu}\right)_\beta}{\left(\frac{\partial \langle N\rangle_\mu}{\partial \mu}\right)_\beta} = \frac{\langle U\times N\rangle_\mu - \langle U\rangle_\mu \langle N\rangle_\mu}{\langle N^2\rangle_\mu - \langle N\rangle_\mu \langle N\rangle_\mu} \tag{3.7}$$

where the brackets $\langle\cdots\rangle_\mu$ denote an average in the grand-canonical ensemble, N is the number of guest molecules, and μ is the chemical potential of the guest molecules. This leads to [166]

$$-q = \Delta H = \frac{\langle U\times N\rangle_\mu - \langle U\rangle_\mu \langle N\rangle_\mu}{\langle N^2\rangle_\mu - \langle N\rangle_\mu \langle N\rangle_\mu} - \langle U_g\rangle - \frac{1}{\beta} \tag{3.8}$$

ΔH in Eq. 3.8 is usually defined as the *isosteric heat of adsorption* and it is often applied at non-zero loading [166]. Again, it is assumed here that the gas phase is ideal. The disadvantage of using this method in practice is that it relies on many particle insertions and removals in the grand-canonical ensemble. The fraction of accepted trial-moves in grand-canonical simulations however can be quite low, even if advanced insertion techniques are used [100, 101, 105]. In practice, long simulations in the grand-canonical ensemble are needed to obtain accurate statistics for the averages in Eq. 3.7, especially in the limit of low chemical potential where the number of guest molecules is either 0 or 1. Therefore, we will not consider the *direct* use of Eq. 3.8 in the remainder of this manuscript.

It is instructive to show that Eqs. 3.3, 3.6 should give the same value for ΔH *at low loading*. Our starting point is the observation that the Henry coefficient is related to the free energy of a guest molecule inside the host (Eq. 3.4). We will make use of the fact that partial derivatives of free energies can always be expressed as ensemble averages [77]. Consider the partial derivative

$$\frac{\partial \ln \langle \exp[-\beta u^+]\rangle_H}{\partial \beta} \tag{3.9}$$

and denote the scaled coordinates of the host (non-framework cations included) by $\mathbf{h}$ and the scaled coordinates of the guest molecules by $\mathbf{g}$. $U_0(\mathbf{h})$ is the energy of the host and $u^+(\mathbf{g},\mathbf{h}) = U_1(\mathbf{g},\mathbf{h}) - U_0(\mathbf{h})$ is the energy of a single guest molecule adsorbed in the host. For the canonical partition function of the host (without the guest) we can write

$$Q_0 = Q_{\text{zeolite without guest}} = \int d\mathbf{h} \exp[-\beta U_0(\mathbf{h})] \tag{3.10}$$

in which we have omitted the constant prefactor of the partition function [77]. For the zeolite with a single guest molecule we can write

$$Q_1 = Q_{\text{zeolite with single guest molecule}} = \int d\mathbf{h} \int d\mathbf{g} \exp[-\beta \left(U_0(\mathbf{h}) + u^+(\mathbf{g},\mathbf{h})\right)] \tag{3.11}$$

In this equation we separated the total energy of a zeolite with a single guest molecule into two contributions: the zeolite and the test particle. The ensemble average $\langle \exp[-\beta u^+] \rangle_H$ is therefore:

$$\begin{aligned} \langle \exp[-\beta u^+] \rangle_H &= \frac{\int d\mathbf{h} \int d\mathbf{g} \exp[-\beta (U_0(\mathbf{h}) + u^+(\mathbf{g},\mathbf{h}))]}{\int d\mathbf{h} \exp[-\beta U_0(\mathbf{h})]} \\ &= \frac{\int d\mathbf{h} [\exp[-\beta U_0(\mathbf{h})] \int d\mathbf{g} \exp[-\beta u^+(\mathbf{g},\mathbf{h})]]}{\int d\mathbf{h} \exp[-\beta U_0(\mathbf{h})]} \end{aligned} \tag{3.12}$$

Taking the partial derivative of its logarithm with respect to β we get

$$\begin{aligned} \frac{\partial \ln \langle \exp[-\beta u^+] \rangle_H}{\partial \beta} &= \frac{\partial}{\partial \beta} \left[\ln \left(\frac{\int d\mathbf{h} [\exp[-\beta U_0(\mathbf{h})] \int d\mathbf{g} \exp[-\beta u^+(\mathbf{g},\mathbf{h})]]}{\int d\mathbf{h} \exp[-\beta U_0(\mathbf{h})]} \right) \right] \\ &= -\frac{\int d\mathbf{h} \int d\mathbf{g} \exp[-\beta (U_0(\mathbf{h}) + u^+(\mathbf{g},\mathbf{h}))](U_0(\mathbf{h}) + u^+(\mathbf{g},\mathbf{h}))}{\int d\mathbf{h} \int d\mathbf{g} \exp[-\beta (U_0(\mathbf{h}) + u^+(\mathbf{g},\mathbf{h}))]} \\ &+ \frac{\int d\mathbf{h} \exp[-\beta U_0(\mathbf{h})] U_0(\mathbf{h})}{\int d\mathbf{h} \exp[-\beta U_0(\mathbf{h})]} \\ &= \langle U_0 \rangle_0 - \langle U_0 + u^+ \rangle_1 \\ &= \langle U_0 \rangle_0 - \langle U_1 \rangle_1 \end{aligned} \tag{3.13}$$

The same can be derived for the other term in Eq. 3.6 (corresponding to the isolated chain):

$$\begin{aligned} \frac{\partial \ln \langle \exp[-\beta u_{IG}^+] \rangle_{EB}}{\partial \beta} &= \langle U_{IG} \rangle_{\text{empty box no chain}} - \langle U_{IG} + u_{IG}^+ \rangle_{\text{empty box with single chain}} \\ &= -\langle u_{IG}^+ \rangle_{\text{empty box with single chain}} \\ &= -\langle U_g \rangle \end{aligned} \tag{3.14}$$

in which U_{IG} is the energy of an empty box (zero) and u_{IG}^+ is the energy of an isolated chain in this empty box. From Eqs. 3.3 and 3.4, we obtain:

$$\Delta H = -\frac{\partial \ln K_H}{\partial \beta} = -\frac{\partial}{\partial \beta} \left[\ln \beta + \ln \langle \exp[-\beta u^+] \rangle_H - \ln \langle \exp[-\beta u_{IG}^+] \rangle_{EB} \right] \tag{3.15}$$

and by substituting Eqs. 3.13 and 3.14 we end up with Eq. 3.6. This means that Eqs. 3.3 and 3.6 should give identical result for ΔH at low loading.

In this work, we propose to use Eq. 3.8 in such a way that $\langle U_{N+1} \rangle_{N+1}$ and $\langle U_N \rangle_N$ are computed in a *single simulation* in the NVT ensemble. This means that for the calculation of ΔH at a certain loading (N guest molecules present in the system), only a *single simulation* of the host structure is needed. This simulation is performed in the ensemble with N guest molecules present (denoted as $\langle \cdots \rangle_N$). Our starting point is

$$\begin{aligned} \langle U_{N+1} \rangle_{N+1} - \langle U_N \rangle_N &= \langle U_N + u^+ \rangle_{N+1} - \langle U_N \rangle_N \\ &= \frac{\langle (U_N + u^+) \exp[-\beta u^+] \rangle_N}{\langle \exp[-\beta u^+] \rangle_N} - \langle U_N \rangle_N \end{aligned} \tag{3.16}$$

in which $u^+ = U_{N+1} - U_N$ is the energy of a test (guest) chain. Note that the coordinates of the test chain are included in $\mathbf{h}$. For chain molecules, it is much more convenient to use the Rosenbluth algorithm [96] to generate a conformation of a test chain. In this case, it is trivial to show that

$$\langle \exp[-\beta u^+] \rangle_N = \langle W \rangle_N \tag{3.17}$$

$$\langle (U_N + u^+) \times \exp[-\beta u^+] \rangle_N = \langle (U_N + u^+) \times W \rangle_N \tag{3.18}$$

and therefore

$$\langle U_{N+1}\rangle_{N+1} - \langle U_N\rangle_N = \frac{\langle (U_N + u^+)\times W\rangle_N}{\langle W\rangle_N} - \langle U_N\rangle_N \tag{3.19}$$

In the Rosenbluth algorithm, it is often convenient to use only part of the non-bonded energy to select trial segments leading to a modified Rosenbluth weight $\langle W^*\rangle$. It can be shown that

$$\langle W\rangle_N = \langle W^* \exp[-\beta\delta]\rangle_N \tag{3.20}$$

$$\left\langle (U_N + u^+)\times W\right\rangle_N = \left\langle (U_N + u^+)\times W^* \exp[-\beta\delta]\right\rangle_N \tag{3.21}$$

in which δ is the energy difference between the total non-bonded part of the potential and the non-bonded part of the potential that was used to select trial segments [103, 104]. The final expression then becomes

$$-q = \Delta H = \frac{\langle (U_N + u^+)\times W^* \exp[-\beta\delta]\rangle_N}{\langle W^* \exp[-\beta\delta]\rangle_N} - \langle U_N\rangle_N - \left\langle U_g\right\rangle - \frac{1}{\beta} \tag{3.22}$$

The ensemble averages $\langle\cdots\rangle_N$ can be computed from the same simulation. Calculating $\left\langle U_g\right\rangle$ requires a simulation of an isolated guest molecule at the same temperature. It is important to note that Eq. 3.22 and Eq. 3.8 lead to identical results and both can be applied at non-zero loading (in contrast to Eqs. 3.3, 3.4, 3.5). At low loading ($N = 0$), Eq. 3.22 becomes identical to Eqs. 3.3, 3.6 and not only the heat of adsorption but also the Henry coefficient can be computed using a single simulation of the host structure (this in contrast to the conventional test particle method).

In principle, one could also perform simulations in the ensemble $\langle\cdots\rangle_N$ to compute averages in the ensemble $\langle\cdots\rangle_{N-1}$. This leads to

$$\langle U_{N-1}\rangle_{N-1} = \frac{\langle U_{N-1}\times \exp[\beta u^+]\rangle_N}{\langle \exp[\beta u^+]\rangle_N} \tag{3.23}$$

with $u^+ = U_N - U_{N-1}$. This would correspond to a real-particle version of Eq. 3.16. However, as this is equivalent to computing the chemical potential using a real particle formulation, this approach will be extremely inefficient [77].

3.3 Model and simulation details

To test the different methods to compute the heat of adsorption, we studied the adsorption of n-alkanes in zeolite LTA5A using the force field of Ref. [160]. We simulated a single unit cell with dimensions of $a = b = c = 24.555$ Å ($\alpha = \beta = \gamma = 90^\circ$) and with composition $Na_{32}Ca_{32}Al_{96}Si_{96}O_{384}$. Periodic boundary conditions are used. The unit cell of LTA consists of 8 cages that are interconnected by small windows, see Fig. 3.1. The crystallographic positions of the framework atoms (Al, Si, O) as well as the *initial* positions of the non-framework cations (Na^+, Ca^{2+}) are taken from the work of Pluth et al. [170]. Electrostatic interactions are handled using the Ewald summation with parameters $\alpha = 0.3$ Å^{-1} and $k = 9$ wave vectors in each reciprocal direction [77].

Simulations were performed in the NVT ensemble at 500K. In each Monte Carlo cycle, it is chosen at random with a fixed probability to displace, rotate, or regrow a hydrocarbon chain (if present in the system) at a random position. As it is well known that fixing the positions of the non-framework cations (Na^+, Ca^{2+}) may lead to erroneous results [82], trial moves to displace the non-framework cations are included. The number of trial moves in each cycle is equal to the number of non-framework cations. The positions of the framework atoms (Si, Al, O) are kept fixed. During the simulations, *test chains* are grown using the Rosenbluth algorithm from which data on the average Rosenbluth weight of the sorbate is collected, this is used to compute the heat of adsorption using Eq. 3.22. The number of test insertions per cycle is equal to the number of non-framework cations. In this way, the amount of CPU time per cycle is approximately equal for the methods to compute the heat of adsorption (Eqs. 3.6, 3.22).

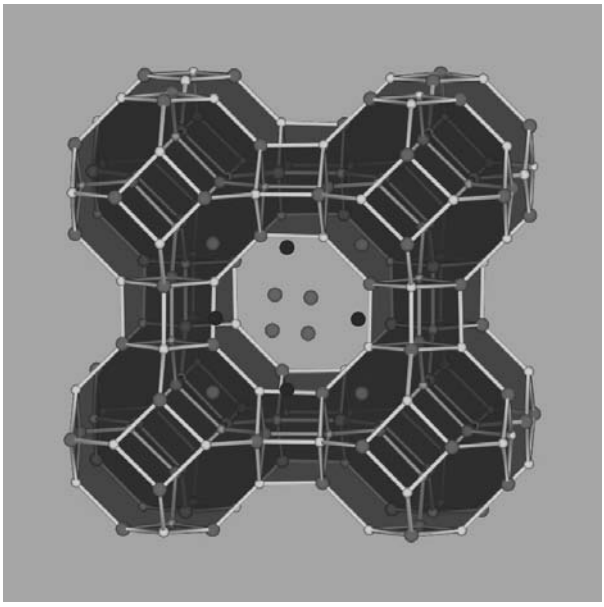

Figure 3.1: Schematic representation of framework type LTA.

3.4 Results

In Fig. 3.2, we have plotted the heat of adsorption of various n-alkanes at zero loading computed using various methods. Clearly, the new method (Eq. 3.22) produces exactly the same result as the

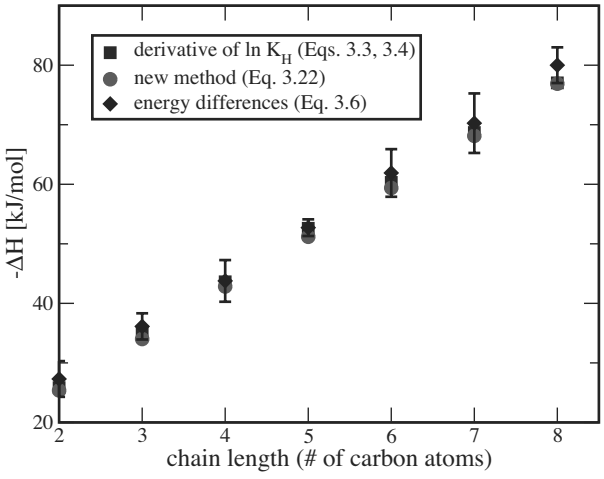

Figure 3.2: Heat of adsorption at zero loading for various n-alkanes in zeolite LTA5A computed using various methods. $T = 500$ K. We have included the error bars for the method based on energy differences. For the other two methods, we checked that the error bars are always smaller than the symbol size.

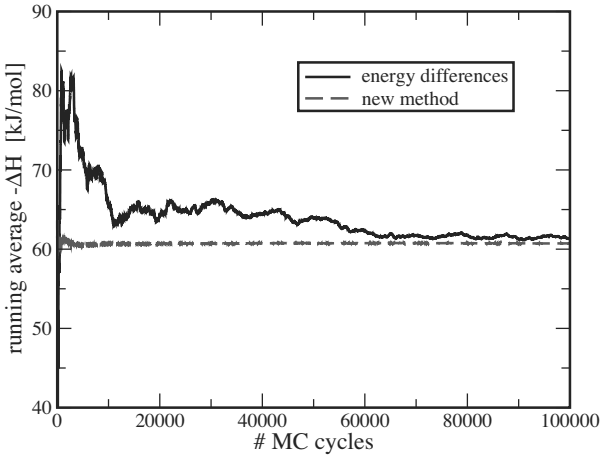

Figure 3.3: Running average of the heat of adsorption of n-hexane at zero loading as a function of the number of MC cycles for the method based on energy differences (Eq. 3.6) and our new method (Eq. 3.22). $T = 500$ K. Small displacements of the non-framework cations are allowed. Initial positions of the non-framework cations were taken from the crystallographic positions [170].

method using the temperature derivative of the Henry coefficient (Eqs. 3.3, 3.4) as well as with the method based on energy differences (Eq. 3.6) within the accuracy of the simulations.

In Fig. 3.3 we have plotted the running average of the heat of adsorption of n-hexane as a function of the number of MC cycles when small displacements of the non-framework cations are allowed. Here, the initial positions of the non-framework cations were taken from the crystallographic positions. The method based on energy differences requires two simulations of the zeolite, one with a single n-hexane chain and one without, while our new method requires only a single simulation of the host system. It turns out that each MC cycle takes approximately the same amount of CPU time for each method, and therefore it becomes clear from Fig. 3.3 that our new method converges much more quicker to the final answer. As the difference $|\langle U_1\rangle_1 - \langle U_0\rangle_0|$ is typically 10^4 times smaller than either $\langle U_1\rangle_1$ or $\langle U_0\rangle_0$, and slightly smaller than the typical fluctuations of either $\langle U_1\rangle_1$ or $\langle U_0\rangle_0$, it is not surprising that the method based on energy differences performs poorly.

In all previous simulations (Figs. 3.2, 3.3), the *initial* positions of the non-framework cations were taken from the known crystallographic positions of LTA5A [170]. For this zeolite, also the positions of the framework Al atoms are well known. Although the non-framework cations are allowed to move during the simulations, as expected their positions during the simulations do not significantly deviate from the crystallographic positions. However, in most cases, for a given zeolite the crystallographic positions of the non-framework cations or the framework Al atoms are *not* known from experiments. However, one could still be interested in computing the adsorption properties in this case. One should keep in mind that for some zeolites the adsorption properties strongly depend on the positions of the framework Al atoms, while for other zeolites this dependency is not present [161, 162].

It is instructive to study this usual senario further, i.e. the positions of the non-framework cations are not known. In this case, the only choice is to start from random initial positions of the non-framework cations and to use a long equilibration period of the system. Trial moves to put a non-framework cation at a *random* position in the zeolite will then significantly accelerate equilibration. It is important to note that this approach relies on the assumption that during the simulation the non-framework cations are able to find their equilibrium positions. This is a major cause for concern, as the interactions between the non-framework cations and the framework atoms are dominated by very strong electrostatic interactions, especially for multivalent ions like Ca.

To investigate the effect of possible rearrangements of the non-framework cations during the

simulation, we conducted a simulation starting from random initial positions for the non-framework cations that was equilibrated for 10^5 cycles. Trial moves to put the non-framework cations at a *random position* in the zeolite were used to accelerate equilibration. The final configuration of the non-framework cations was then used as a starting point to compute the heat of adsorption using Eqs. 3.6 and 3.22, see Fig. 3.4. Clearly, the method based on energy differences is extremely inaccurate as during the simulations, *the positions of the non-framework cations in the simulation with the n-hexane chain apparently deviate from those in the simulation without the n-hexane chain*, even though these simulations were started from the same initial non-framework cation positions. This difference in non-framework cation positions will have a huge effect on the total energies $\langle U_1 \rangle_1$ and $\langle U_0 \rangle_0$, and therefore it will dramatically effect the efficiency of any method to compute the heat of adsorption that requires more than one simulation of the host structure. In principle, the huge difference of Fig. 3.4 would eventually disappear if one would simulate much longer, so that all rearrangements of non-framework cations would be visited according to their statistical weight. Unfortunately, due to the very strong interactions of the non-framework cations with the framework this will take extremely long simulations, even at high temperature (500 K).

From Figs. 3.3 and 3.4 we can conclude that the method based on energy differences is very sensitive to the displacements of the non-framework cations, and far less sensitive to the adsorption energy of a hydrocarbon. Therefore, the use of this method is not recommended for zeolites with strongly interacting non-framework cations. Note that the heat of adsorption of n-hexane calculated using our new method is approximately 60.7 kJ/mol for the simulations of Fig. 3.3 and 62.7 kJ/mol for the simulations of Fig. 3.4. As this difference it very small, one can conclude that the positions of the non-framework cations only have a minor influence on the heat of adsorption for LTA5A. However, performing the simulations with (arbitrary) fixed non-framework cation positions is not a sensible option as this may introduce other artifacts (especially when the temperature or loading is varied) [82].

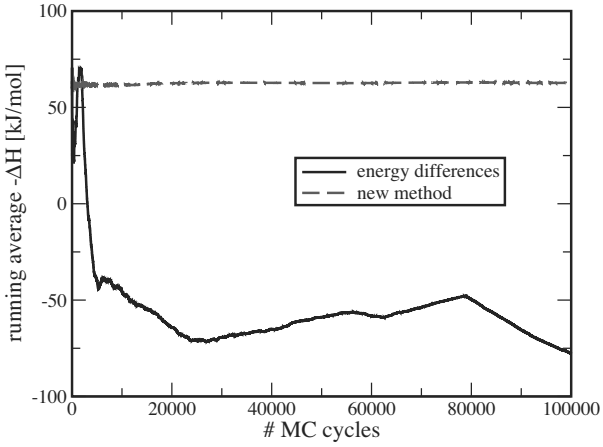

Figure 3.4: Running average of the heat of adsorption of n-hexane at zero loading as a function of the number of MC cycles for the method based on energy differences (Eq. 3.6) and our new method (Eq. 3.22), *not starting from the crystallographic positions of the non-framework cations*. $T = 500$ K. A simulation starting from random initial non-framework cation positions was conducted and a long equilibration period was used. The final configuration of this simulation was used here as the starting point to compute the heat of adsorption. Trial moves to put non-framework cations at random positions in the zeolite are included to accelerate equilibration of the positions of the non-framework cations.

3.5 Handling of Coulombic interactions in zeolites

In the previous section we have analyzed the difficulties introduced by strong electrostatic interactions in zeolites. Electrostatic interactions are very long-ranged due to their r^{-1} behavior. It is well known that simple truncation of these interactions may lead to incorrect simulation results [77, 171, 172]. Also, a direct summation of Coulombic pair interactions is conditionally convergent, i.e. the final result depends on the order of the summation. It is for this reason why the well-known Ewald summation [77, 87, 88] or equivalent method is currently the generally accepted method in molecular simulations. For the Ewald summation, the total Coulombic energy of the system can be written as the sum of three contributions (assuming tin foil boundary conditions):

- The real-space part, which is proportional to

$$E_{\text{real}} = \sum_{i<j} \frac{q_i q_j \text{erfc}(\alpha r_{ij})}{r_{ij}} \tag{3.24}$$

  in which $\text{erfc}(x)$ is the complementary error function, r_{ij} is the distance between particles i and j, q_i and q_j are the charges on particles i and j respectively and α is a constant damping factor. The summation $\sum_{i<j}$ is in principle a summation over all periodic images of i and j. However, it is convenient to choose α in such a way that only the nearest images have to be considered (as $\text{erfc}(x)$ is close to zero for large x). This requires a value of α that is not too small. The real-space part of the Ewald summation and the conventional Lennard-Jones interactions can be calculated simultaneously using the same cut-off radius.

- The self energy

$$E_{\text{self}} = -\frac{\alpha}{\sqrt{\pi}} \sum_{i=1}^{N} q_i^2 \tag{3.25}$$

  which does not depend on the positions of the ions in the system.

- The Fourier part of the energy, which is proportional to

$$E_{\text{Fourier}} = \frac{1}{2V} \sum_{\mathbf{k}\neq 0}^{\infty} \frac{\exp[-k^2/4\alpha^2]}{k^2} |\sum_{j=1}^{N} q_j \exp[-i\mathbf{k}\cdot\mathbf{r}_j]|^2 \tag{3.26}$$

  in which V is the volume of the system and the vectors $\mathbf{k}$ are linear combinations of the reciprocal basis vectors of the system. For larger systems ($> 10^4$ charges), it is more efficient to replace Eq. 3.26 by a grid-based computation like Particle Mesh Ewald[77].

The convergence of the total energy is controlled by the real-space cut-off r_{cut}, the value of α and the number of vectors in each reciprocal direction (k). Provided that only nearest images are used to calculate the real-space energy (Eq. 3.24), the total energy as a function of the number of k-vectors converges to the same value for a large number of k-vectors, independent of the value of α (provided that α is sufficiently large).

The Fourier part of the system clearly depends on the positions $\mathbf{r}_i$ (and charges q_i) of all N particles in the system. This may suggest that in a Monte Carlo simulation, in every trial move the positions of *all* particles in the system have to be considered for the calculation of the energy difference between the new and old configuration. Fortunately, it is possible to rewrite the Ewald summation in such a way that only the atoms with a different position have to be considered. The structure of Eq. 3.26 can be expressed as

$$E_{\text{Fourier}} \propto \sum_{\mathbf{k}\neq 0} |x(\mathbf{k}, \mathbf{r}^N, \mathbf{q}^N)|^2 = \sum_{\mathbf{k}\neq 0} \left[\mathscr{R}(x(\mathbf{k}))^2 + \mathscr{I}(x(\mathbf{k}))^2\right] \tag{3.27}$$

in which the complex numbers x depends on the positions ($\mathbf{r}^N$) and charges ($\mathbf{q}^N$) of all the atoms in the system. The real and imaginary component of this vector can be expressed as

$$\mathscr{R}(x(\mathbf{k})) = \sum_{i=1}^{N} q_i \cos(\mathbf{k}\cdot\mathbf{r}_i) \tag{3.28}$$

and

$$\mathscr{I}(x(\mathbf{k})) = \sum_{i=1}^{N} q_i \sin(\mathbf{k}\cdot\mathbf{r}_i) \tag{3.29}$$

As $\mathscr{R}(x(\mathbf{k}))$ and $\mathscr{I}(x(\mathbf{k}))$ can be expressed as a summation over all particles in the system, it is convenient to store $\mathscr{R}(x(\mathbf{k}))$ and $\mathscr{I}(x(\mathbf{k}))$ in the memory of the computer (one complex number for each $\mathbf{k}$). For particle displacements, rotations, regrows, (test) insertions, deletions and identity changes one can easily calculate the new values for $\mathscr{R}(x(\mathbf{k}))$ and $\mathscr{I}(x(\mathbf{k}))$ by subtracting the contributions of the old configuration and adding the contributions for the new configuration. This has to be done only for atoms that have a different position in the old and new configuration.

Recently, Wolf and co-workers [89] have proposed a pairwise alternative for the Ewald summation. In this method, the Coulombic interactions are damped using a complementary error function that is truncated and shifted at distance r_{cut} resulting in the following pair potential ($r_{ij} \leq r_{\text{cut}}$):

$$\phi_{\text{Wolf}}(r_{ij}) = q_i q_j \left[\frac{\text{erfc}(\alpha r_{ij})}{r_{ij}} - \frac{\text{erfc}(\alpha r_{\text{cut}})}{r_{\text{cut}}} \right] \tag{3.30}$$

Fennell and Gezelter [159] have developed slightly modified damping function ($r_{ij} \leq r_{\text{cut}}$)

$$\begin{aligned} \phi_{\text{FG}}(r_{ij}) &= q_i q_j \left[\frac{\text{erfc}(\alpha r_{ij})}{r_{ij}} - \frac{\text{erfc}(\alpha r_{\text{cut}})}{r_{\text{cut}}} \right] \\ &+ q_i q_j (r_{ij} - r_{\text{cut}}) \left[\frac{\text{erfc}(\alpha r_{\text{cut}})}{r_{\text{cut}}^2} + \frac{2\alpha \exp[-\alpha^2 r_{\text{cut}}^2]}{\sqrt{\pi} r_{\text{cut}}} \right] \end{aligned} \tag{3.31}$$

Compared to the Ewald summation, the long range Fourier part (Eq. 3.26) is omitted, which is only strictly correct in the limits $\alpha \to 0$ and $r_{\text{cut}} \to \infty$. To make a comparison between the results obtained from the Ewald summation and the Wolf method, one should not only consider the computationally efficiency of the methods, but also how the computed averages obtained from the methods depend on the control parameters (for the Wolf method, r_{cut}, α and for the Ewald summation r_{cut}, α and the number of k-vectors in each reciprocal direction k). As the cut-off radius is limited by the size of the simulation box (e.g. when the nearest image convention is used, r_{cut} is limited to half the boxsize [77]), a larger value of r_{cut} may imply that a zeolite consisting of more unit cells is required.

Although there have been several studies on the comparison between the Wolf method and the Ewald summation [159, 173–175], these studies mainly focus on reproducing the *total* energy of the simulation box at finite temperature, and not on the *energy change* when a polar molecule is inserted into a simulation box. We have tested the Ewald summation and the Wolf method for calculating the heat of adsorption of CO_2 at zero loading in all silica MFI-type zeolite using the recently proposed force field of Ref. [176] (calculated using Eq. 3.22). As our goal is to investigate the differences between the Wolf method and the Ewald summation, we have eliminated all Lennard-Jones interactions and all atoms in the system are modeled as hard spheres with a diameter of 3 Å. The partial charges of the atoms are taken as follows: $q_{\text{O(zeo)}} = -1.025e$, $q_{\text{Si(zeo)}} = +2.05e$, $q_{\text{C(CO}_2\text{)}} = +0.6512e$, $q_{\text{O(CO}_2\text{)}} = -0.3256e$. Grid interpolation techniques [75, 84] to compute pair potentials have not been used. As the self-interactions of the Wolf-method for CO_2 and the zeolite are constant and independent of the reference state, only pair interactions between CO_2 and the zeolite (Eqs. 3.30, 3.31) need to be considered for the Wolf method.

In Fig. 3.5, we have plotted the energy difference $\langle U_1 \rangle_1 - \langle U_0 \rangle_0 - \langle U_g \rangle$ calculated using Eq. 3.22 for both the Wolf method and the modification by Fennell and Gezelter (Eq. 3.31) as a function of α for various values of the cut-off radius r_{cut}. In the same figure, the result obtained from the Ewald summation is also included. Clearly, the result strongly depends on the precise value of α and r_{cut}, especially for small values of r_{cut}. The value of $\alpha = 0.2$ Å^{-1} as suggested by some authors [159, 174] leads to incorrect results for this system. At this point it is important to note that for practical usage of the Wolf method, the computed results should not depend too strongly on the precise values of r_{cut} and α. From Fig. 3.5 it becomes clear that that there is only a small range of α which leads to results consistent with the Ewald summation, and that a

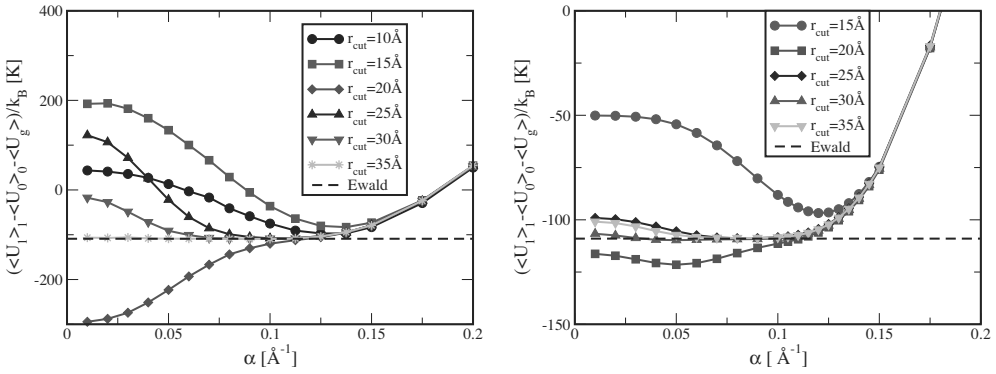

Figure 3.5: Average energy difference $\langle U_1 \rangle_1 - \langle U_0 \rangle_0 - \langle U_g \rangle$ for CO_2 in all silica MFI-type zeolite computed using the Wolf method (left) or using the modification by Fennell and Gezelter (right). The (unweighted) average is taken over all possible configurations of CO_2 that do not result in an overlap with zeolite atoms. The zeolite consists of $4 \times 4 \times 6$ unit cells. The size of the simulation box is therefore: $a = 80.088$ Å, $b = 79.596$ Å, $c = 80.298$ Å. In all simulations, 3×10^7 trial insertions are used (Eq. 3.22). The result obtained by the Ewald summation ($\alpha = 0.3$ Å^{-1}, $k = 20$, $r_{\text{cut}} = 12$ Å) is also included.

cut-off radius of at least 25 Å is required to avoid a large sensitivity for the precise values of α and r_{cut}. This hold for both the original Wolf method and the modification by Fennell and Gezelter. Although for some values of α and r_{cut} the average heat of adsorption computed using the Wolf method is identical to the one computed using the Ewald summation, this does not guarantee that the energy of *each individual configuration* of CO_2 computed using both methods is identical. In Fig. 3.6, we plotted the *average absolute energy difference* between the adsorption energy computed using the Ewald summation ($u_{\text{Ewald}}(\mathbf{g})$) and the adsorption energy computed using the Wolf method ($u_{\text{Wolf}}(\mathbf{g})$), calculated for the same configurations ($\mathbf{g}$) of CO_2, and averaged over all possible configurations of CO_2 that do not overlap with the zeolite. For the optimal value of α for $r_{\text{cut}} = 20$ Å, the *average absolute energy difference* between the Wolf method and the Ewald

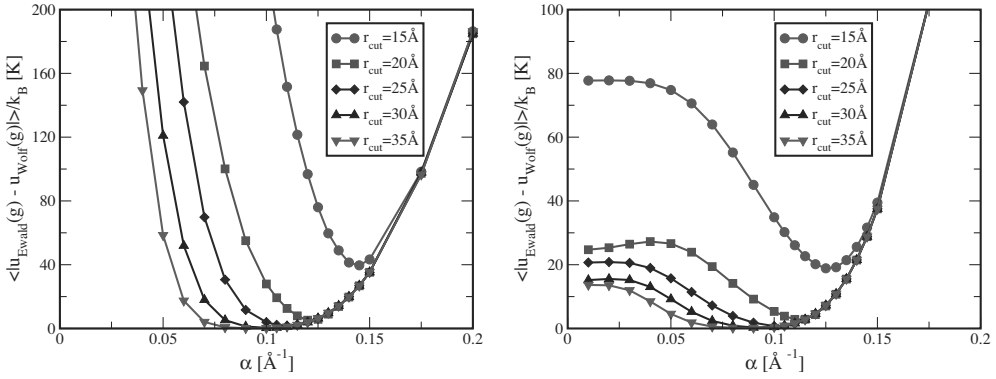

Figure 3.6: Absolute energy difference between the Ewald summation and the Wolf method for individual configurations of CO_2 (denoted as $\mathbf{g}$) in MFI-type zeolite, averaged over all possible configurations of CO_2 that do not overlap with the zeolite. Left: Original Wolf method (Eq. 3.30). Right: The modification by Fennell and Gezelter (Eq. 3.31). The zeolite consists of $4 \times 4 \times 6$ unit cells. The size of the simulation box is therefore: $a = 80.088$ Å, $b = 79.596$ Å, $c = 80.298$ Å. In all simulations, 3×10^7 trial insertions are used (Eq. 3.22).

# unit cells	α [Å^{-1}]	k	r_{cut} [Å]	$\left(\langle U_1\rangle_1 - \langle U_0\rangle_0 - \langle U_g\rangle\right)/k_B$ [K]
$4\times4\times6$	0.4	30	20	−110.4
$2\times2\times3$	0.3	15	12	−108.9
$2\times2\times3$	0.3	20	12	−109.8
$2\times2\times3$	0.3	30	12	−109.6
$2\times2\times3$	0.4	10	12	−110.6
$2\times2\times3$	0.4	20	12	−110.1
$2\times2\times3$	0.3	10	18	−109.2
$2\times2\times3$	0.3	20	18	−109.2
$2\times2\times3$	0.3	30	18	−109.2
$2\times2\times3$	0.5	20	18	−109.6

Table 3.1: Average energy difference $\langle U_1\rangle_1 - \langle U_0\rangle_0 - \langle U_g\rangle$ for CO_2 in all silica MFI-type zeolite computed using the Ewald summation. In all simulations, 3×10^7 trial insertions are used (Eq. 3.22).

summation *for a single configuration of CO_2* is on average 4%, while the difference in *average energy* is zero for the optimal value of α. This means that although the Wolf method may predict correct averages for the optimal α and r_{cut}, one should also test whether the *energy of individual configurations* is computed correctly (i.e. identical to the result obtained by the Ewald summation). If this is not the case, one can expect artifacts in the simulation results. From Figs. 3.5 and 3.6 it becomes clear that the Wolf method only converges to the correct energy for *each configuration* of CO_2 for *(1)* a cut-off radius of at least 25 Å and *(2)* a narrow range of α.

The results of the Ewald summation are not very sensitive to the precise values of α and r_{cut}, see table 3.1. It is well known that if only nearest images are used to compute the real-space part of the energy (Eq. 3.24), the total energy of the system as a function of k at constant α should always converge to the same value for large k, provided that α is large enough. The difference between the averages in table 3.1 is less than 1% which is approximately equal the error in any of the reported values in table 3.1. We verified that the energy of *each single configuration* of CO_2 is within 0.1 % for any of the values of α, r_{cut}, k reported in table 3.1. It is important to note that the finite-size effect is absent for our system when charges are handled using the Ewald summation and therefore one can use a small simulation box ($2\times2\times3$ unit cells). For the Wolf method however, this is not possible as a cut-off radius of at least 25 Å is needed. According to the nearest image convention the size of the simulation box needs to be at least twice the value of r_{cut}. Using such a large cut-off radius is inconvenient, as the usual sorbate-zeolite and sorbate-sorbate Lennard-Jones type interactions have a cut-off radius of typically 12 Å [81, 82, 157, 177]. We compared the CPU time required for the Wolf method for $\alpha = 0.1$ Å^{-1} and $r_{\text{cut}} = 25$ Å ($4\times4\times6$ unit cells) with the Ewald summation ($\alpha = 0.3$ Å^{-1}, $k = 15$, $r_{\text{cut}} = 12$ Å, $2\times2\times3$ unit cells) for the same number of trial insertions of CO_2. Although in this simulation using the Ewald method 88% of the CPU time is spent in calculating the Fourier energy (Eq. 3.26), the simulation using the Ewald method is still 7 times faster due to the fact that a smaller cut-off radius can be used.

While other studies found quite good agreement between the Wolf method and the Ewald summation for condensed phases [159, 173–175], our findings (Figs. 3.5, 3.6) show that convergence to the Ewald result is more difficult for zeolites. The reason is that the Wolf method critically depends on the screening of electrostatics around a central ion. Due to the screening the *effective range* of the potential will be reduced, and therefore a summation of pair interactions seems sufficient to describe effective interactions between ions. As a large part of the zeolite consists of empty pores (at low loading), the screening of Coulombic interactions is less efficient and a large cut-off radius is required.

It is instructive to test the convergence of the Wolf method for a worse-case scenario, i.e. a system that is highly disordered with large concentration gradients, even though the Wolf method was not designed for such a system. For molten NaCl *at high density*, it has been shown that the total energy computed by the Wolf method is in reasonable agreement with the Ewald summation [175]. Consider a system of 100 Na^+ ions and 100 Cl^- ions in a simulation box of $250\times250\times250$

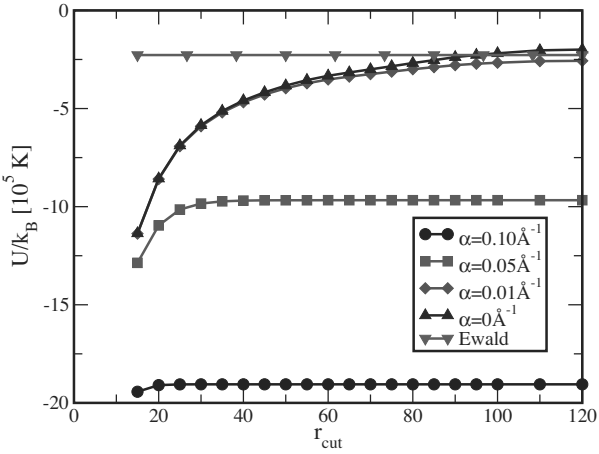

Figure 3.7: Total energy of a single configuration of 100 randomly placed Na^+ ions and 100 randomly placed Cl^- ions in a simulation box of $250 \times 250 \times 250$ Å, computed using the Ewald summation, the Wolf method, and a direct r^{-1} summation ($\alpha = 0$ Å^{-1}). Hard-core overlaps are avoided in this single configuration.

Å, the density of this system is extremely low. The ions are placed at random positions in the simulation box in such a way that hard-core overlaps (here: ion-ion distance smaller than 3 Å) are avoided. For a single configuration of the ions, we investigated the total energy computed using the Wolf method for various values of α [89]

$$E_{\text{Wolf}} = -\left(\frac{\alpha}{\sqrt{\pi}} + \frac{\text{erfc}(\alpha r_{\text{cut}})}{2r_{\text{cut}}}\right)\sum_{i=1}^{N} q_i^2 + \sum_{i<j}\phi_{\text{Wolf}}(r_{ij}) \tag{3.32}$$

The results are shown in Fig. 3.7. Clearly, for $\alpha = 0.1$ Å^{-1} and $\alpha = 0.05$ Å^{-1} the total energy of the Wolf method converges to an incorrect total energy. For $\alpha = 0.01$ Å^{-1}, the energy of the Wolf method converges to the result obtained by the Ewald summation. However, the convergence is just as slow as a direct r^{-1} summation of pair interactions ($\alpha = 0$ Å^{-1} in Eq. 3.30). This clearly shows that the Wolf method critically depends on the screening of electrostatic interactions and that for a given system one should always check whether such a screening is applicable.

It is well known that a direct r^{-1} summation only converges for very large values of the cut-off radius [77], for example more than 40 Å for neutral molecules. Damping the Coulombic potential reduces this range, although still a cut-off of at least 25 Å seems to be the minimum requirement, but at the cost of uncertainty in the damping constant α. Different values for α are recommended in the literature implying this damping is system specific and possibly dependent on the molecule type, framework topology, temperature, etc. The Ewald summation is able to compute the electrostatic energy exactly (to within any specified numerical precision) for a system of charges in an infinitely periodic structure at a cost less than quadratic with the number of particles ($N^{3/2}$ for Ewald). The energy and forces computed with the Ewald summation are well-defined and unique. They do not depend on a judicious choice of damping parameters and cut-off values, and Ewald type methods are at the same level of accuracy significantly cheaper.

3.6 Conclusions

We have introduced a new method to compute the heat of adsorption for adsorbates in framework structures with non-framework cations that requires only a *single* simulation of the host. The main difference with the conventional Widom's test particle method is that Widom's test particle method only provides the Henry coefficient at a certain temperature, and therefore, additional simulations at different temperatures and a numerical differentiation will be necessary to compute the heat of adsorption. The often used method based on energy differences is far more sensitive to the precise displacements of the non-framework cations than to the interactions with the adsorbate and therefore this method is unsuited for structures with non-framework cations. In addition, we have shown that for studying adsorption in zeolites, the Ewald summation is superior to the recently proposed Wolf method (and other direct summation methods), both in accuracy and speed. The Ewald method can be implemented very efficiently for Monte Carlo methods as only the change for moving atoms needs to be computed.

4

Adsorption selectivity of benzene/propene mixtures for various zeolites

The 9-site benzene model of Zhao *et al*. (J. Phys. Chem. B **2005**, 109, 5368-5374) has been used to systematically study the adsorption of benzene, propene, and benzene-propene mixtures in zeolites mordenite, Y, β, silicalite and MCM22. Interaction parameters for the benzene-zeolite interactions have been fitted to available adsorption experiments from literature. As an independent check of our force field, we have performed additional adsorption experiments using the TEOM technique and excellent agreement between simulations and TEOM experiments was found. High adsorption selectivities for benzene in benzene-propene mixtures were found in all zeolites, except for silicalite.

S. Ban, A.N.C. van Laak, P.E. de Jongh, J.P.J.M. van der Eerden, T.J.H. Vlugt, *Journal of Physical Chemistry C* Volume 111 (2007), 17241-17248

4.1 Introduction

Cumene (isopropylbenzene) is an important chemical intermediate used for the production of phenol and acetone [54]. The traditional cumene production is based on the alkylation of benzene and propene using a solid acid catalyst. This process requires a large excess of benzene (high benzene/propene (B/P) ratio) to suppress side reactions, e.g. alkene oligomerization and multiple alkylations of benzene. In alkylation processes, a high ratio of 'inert' reactant (e.g. benzene) versus reactive reactant molecules (e.g. alkenes) can be realized by a proper selection of the reactor type [178]. The large size of reactors, separation units and recycling streams of production plants due to the large excess of benzene brings about both large energy consumption and high capital investments [55].

There is a large interest to replace the solid acid catalyst for cumene production by protonated zeolites. This could have the following advantages: *(1)* a lower operating temperature, which results in less by-products and *(2)* the possibility to reduce the B/P ratio [178]. In the ideal situation, the B/P ratio is only very large at the active site inside the zeolite and close to one in the reactor feed. Promising results for the production of cumene have been found for the zeolites mordenite, Y, β and MCM22 [55].

To optimize such processes, understanding of the adsorption and diffusion of benzene and propene at the molecular scale is necessary. In this work, molecular simulations are used to investigate the location and the adsorption thermodynamics of propene and benzene in various zeolites. The adsorption of linear alkanes in zeolites has been well studied by experiments [38, 179–183] and Monte Carlo simulations [78, 81, 82, 84, 153, 154, 156, 184–187]. The adsorption and diffusion of alkenes is not well accessible through experiments due to their reactivity [186, 188]. The first Monte Carlo simulations of benzene in zeolites were performed by Snurr *et al.* [151] using an all-atom model with 12 charged sites (similar to the OPLS model for benzene [189]). This model has been used extensively [190–192]. Recently, it has been found that a correct representation of the quadrupole moment (originating from the π-system of benzene) is crucial for the reproduction of the structure of liquid and solid benzene [193, 194]. In particular, the orientation dependence of the interaction between benzene molecules (often a T-shaped structure [195–197]) strongly depends on the quadrupole moment [193, 194]. Note that the OPLS model for benzene has no quadrupole moment. Siepmann and co-workers have introduced a 9-site model for benzene [194, 198] in which the CH groups are modeled as chargeless united atoms and three additional charged interaction sites are added to reproduce the quadrupole moment caused by the π system. This model correctly reproduced the experimental vapor-liquid and vapor-solid phase coexistence as well as the sublimation and evaporation pressures. As the 9-site model contains only 3 partial charges it is computationally much more efficient than the 12 site model (12 partial charges).

In this work, we used this 9-site model to study the adsorption of benzene in various all-silica zeolites, i.e. mordenite, Y, β, silicalite and MCM22. We fitted the benzene-zeolite interactions to available experimental adsorption data (heats of adsorption and adsorption isotherms) from literature following the procedure of Dubbeldam *et al.* [81]. We have also performed adsorption experiments as an independent check that our force field is able to reproduce the adsorption behaviour of benzene. Our model is further used to calculate mixture isotherms and x-y diagrams for benzene and propene. In particular, we find a high adsorption selectivity of benzene for mordenite, β, MCM22, a slightly reduced selectivity for zeolite Y, and almost no selectivity for silicalite.

4.2 Methods

4.2.1 Simulation method

Adsorption isotherms are calculated using Configurational-bias Monte Carlo (CBMC) simulations in grand-canonical ensemble (GCMC) [77, 84, 138, 201]. In our simulations, Lennard-Jones (LJ) interactions are used to describe interactions between all adsorbates and zeolite atoms. The Ewald summation is used for Coulombic interactions between benzene and the zeolite. All other intermolecular interactions are truncated and shifted at 12 Å [81]. Periodic boundary conditions are

Framework[a]	Number of unit cells	Size of simulation box [Å]	Space Group
MOR	$2\times2\times5$	$36.188\times41.032\times37.620$	*Cmcm*
MFI	$2\times2\times3$	$40.044\times39.798\times40.149$	*Pnma* (*Ortho*)
MFI	$2\times2\times3$	$40.242\times39.640\times40.314$	$P2_12_12_1$ (*Para*)
FAU	$1\times1\times1$	$25.028\times25.028\times25.028$	$Fd-3m$
BEA	$2\times2\times1$	$25.322\times25.322\times26.406$	$P4_122$
MWW	$1\times2\times1$	$24.447\times28.228\times24.882$	$P6/mmm$

Table 4.1: Zeolites used in this study. [a]framework types: mordenite (MOR), silicalite (MFI), Y (FAU), β (BEA) and MCM22 (MWW). The coordinates of the atoms of *Para* MFI are taken from van Koningsveld *et al.* [199]. The atomic positions of the other frameworks have been taken from Ref. [200].

applied. In our simulations, the pressure varies from 1.0 Pa to 1.0 bar, and temperatures are in the range from 373 K to 523 K. Under these conditions pure benzene and propene are in the gas phase.

A typical simulation consists of at least 10^6 cycles. In each cycle, trial moves are attempted to translate, rotate or (partially) regrow a molecule, to exchange a molecule with the reservoir, and to change the identity of a molecule (only for mixtures) [84]. The number of trial moves per cycle is equal to the number of molecules with a minimum of 20. Parameters for the benzene-zeolite interactions were obtained using the procedure outlined by Dubbeldam *et al.* [81] using experimental isotherms for loadings up to the inflection point of benzene. Heats of adsorption are determined from isotherms using the Clausius-Clapeyron equation [163]

$$Q=-R\left(\frac{\partial \ln P/P_0}{\partial T^{-1}}\right)_{q=\text{constant}} \tag{4.1}$$

where P is the pressure, P_0 an arbitrary reference pressure, T the absolute temperature, q the loading, and R the gas constant.

The zeolites listed in Table 4.1 are studied as potential catalysts for cumene synthesis by computing the adsorption properties of propene and benzene. For silicalite, two frameworks with different space groups (*Ortho* and *Para*) are considered. In experiments, the transition from *Ortho* to *Para* is caused by the enlargement of the micropores during the adsorption of bulky aromatic molecules (see Ref. [191] for a discussion on this topic). In our simulations, this transition was not considered and either the *Ortho* or *Para* structure was simulated. We use a rigid approximation of zeolites which is justified by the fact that flexibility only results in very small deviations of adsorption properties such as adsorption isotherms and Henry coefficients [72].

Molecule	Atom Type	σ [Å]	ε/k_B [K]
propene	CH_3-CH_3	3.76	108.0
	CH_2(sp2)-CH_2(sp2)	3.68	92.5
	CH(sp2)-CH(sp2)	3.73	52.0
	CH_3-O	3.48	93.0
	CH_2(sp2)-O	3.50	82.6
	CH(sp2)-O	3.43	69.0
benzene	$CH_{benzene}$-$CH_{benzene}$	3.74	53.5
	$CH_{benzene}$-O	3.38	73.0

Table 4.2: Lennard-Jones parameters for guest-guest and guest-host interactions. LJ interactions between Si and CH_x are not taken into account. Interaction parameters for non-identical hydrocarbon groups are calculated using the Jorgensen mixing rules [202].

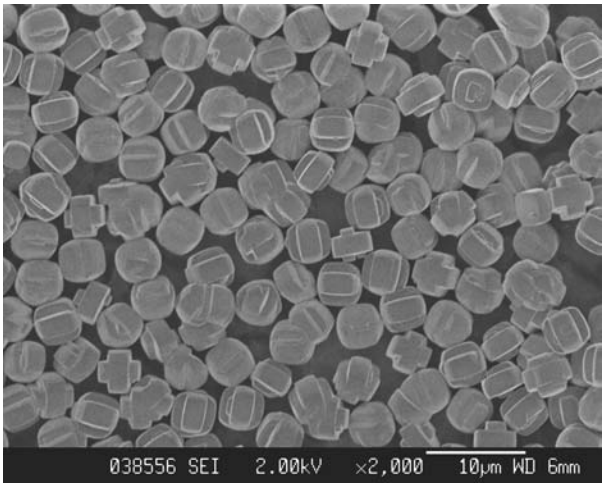

Figure 4.1: SEM image of our silicalite sample.

4.2.2 Interaction model

In table 4.2, the Lennard-Jones parameters for the intermolecular interactions are listed. Propene is described by an uncharged united atom model. The parameters for the CH_3-CH_3 and CH_3-O interactions are taken from Calero *et al*. [82]. The other interaction parameters for propene (LJ interactions, bond-bending and bond-stretching) originate from Jakobtorweihen *et al*. [186]. Note that Jakobtorweihen *et al*. used tail corrections and a different cutoff radius (14 Å). We have converted the original parameters of Jakobtorweihen *et al*. to a potential that is truncated and shifted at 12 Å without the use of tail corrections.

For benzene, the 9-site model of Zhao *et al*. [194] is used. Besides the six (uncharged) united CH atoms, three additional beads are used to model the quadrupole moment of benzene. These charged beads are located symmetrically on the 6-fold axis with a positive charge of +2.42e placed in the benzene plane and two compensating negatively charged beads at distances of 0.785 Å. Only the united CH atoms of benzene have LJ interactions with the zeolite or other guest molecules. The LJ interactions of benzene are adjusted to a potential that is truncated and shifted at 12 Å without the use of tail corrections. The partial charges of the zeolite atoms (q_O=-1.025e, q_{Si}=+2.05e) are taken from Calero *et al*. [82].

4.2.3 Experiments

Silicalite (ZSM5-06) was provided by ExxonMobil and consisted of intergrown x-shaped crystals with a uniform particle size of $\sim$4 μm, having a silica to alumina ratio in the gel of 600 (Fig. 4.1). The silicalite was calcined in flowing air to remove template molecules by heating to 823 K at a rate of 0.83 K min^{-1} and was maintained at that temperature for 4 hours before cooling down to ambient temperatures. A micropore volume of 0.14 cm^{3}g^{-1} was recorded using N_2-physisorption (Micromeritics Tristar 3000) at 77 K.

Adsorption isotherms of benzene in MFI were recorded in a TEOM reactor (Rupprecht & Pataschnick TEOM 1500 PMA). The sample (approximately 65 mg) was transferred into a 100 μl quartz container and held in place between two layers of quartz wool. The sample was dried overnight at 623 K in situ in nitrogen atmosphere (grade 5.0). For measurements helium (grade 4.6) was used as a carrier gas at a total pressure of 1.3 bar. Benzene was injected into the system using an ISCO 260D syringe pump in a range varying between 1-80 μl min^{-1} of benzene (Acros p.a.) in a helium flow of 80 ml min^{-1}, resulting in a benzene partial pressure between 0.45 and

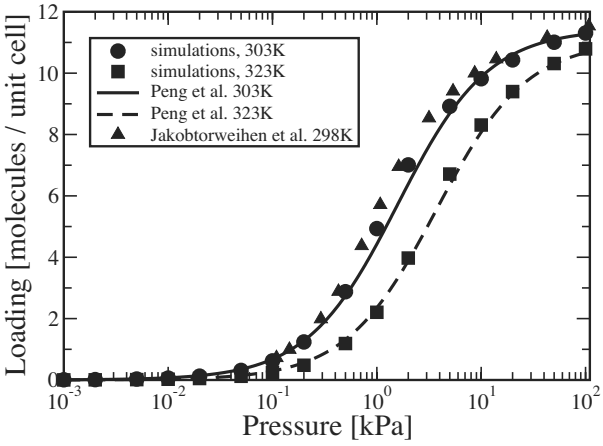

Figure 4.2: Experimental [204] and simulated [186] adsorption isotherms for propene in silicalite at various temperatures.

46.8 kPa. Results were corrected for loss of water and changes in gas density. For a detailed description of the TEOM technique we refer to Chen *et al*. [203] and Zhu *et al*. [181].

4.3 Results and discussion

4.3.1 Adsorption of pure components

Fig. 4.2 shows that our simulations for propene in silicalite agree well with experimental data at 303 K and 323 K. As expected, we exactly reproduce the simulations of Ref. [186] from which our force field was derived. The heat of adsorption from our simulations is approximately 38.8 kJ/mol while experiments show a value of 40 kJ/mol [205]. Propene is absorbed both at the intersections and the channel interiors of silicalite.

It is well known that benzene is a strong adsorbate with a large kinetic diameter of approximately 5.8 Å [210]. Therefore, in silicalite, benzene is preferentially adsorbed at the relatively wide channel intersections (about 9 Å wide) instead of the channel interiors (straight channels of size 5.3×5.6 Å and zigzag channels of size 5.1×5.5 Å). Experiments [207, 209, 211, 212] show that adsorption isotherms of aromatics (e.g. benzene, p-xylene) in silicalite have a characteristic inflection around four molecules per unit cell which corresponds to the four channel intersections per unit cell in silicalite. NMR experiments [213, 214] suggest that at four molecules per unit cell, the silicalite framework gradually undergoes a transformation from space group *Ortho* to *Para*. At loadings below four molecules per unit cell only the *Ortho* structure is present, while at loadings larger than seven molecules per unit cell the *Para* structure is found exclusively. An extra driving force is needed to push benzene molecules into the less-favorable channel interiors of silicalite. This process triggers the phase transition from *Ortho* to *Para* and results in an inflection in the adsorption isotherm. A similar inflection behavior (without a change in zeolite structure) has been found for branched hydrocarbons in MFI (e.g. isobutane) [83].

Fig. 4.3 (a) shows a comparison between our computed adsorption isotherms for benzene in *Ortho* silicalite and the available experimental data. Only the experimental data of Fig. 4.3 (a) was used to fit the missing force field parameters of table 4.2 and only up to the inflection point. Excellent agreement is found for all simulations with loadings up to four molecules per unit cell. The isotherm of Song *et al*. [207] at 323 K significantly deviates at loadings higher than four molecules per unit cell. This suggests that beyond 4 benzene molecules per unit cell the structural transition of the frameworks needs to be taken into account. A comparison between our simulations

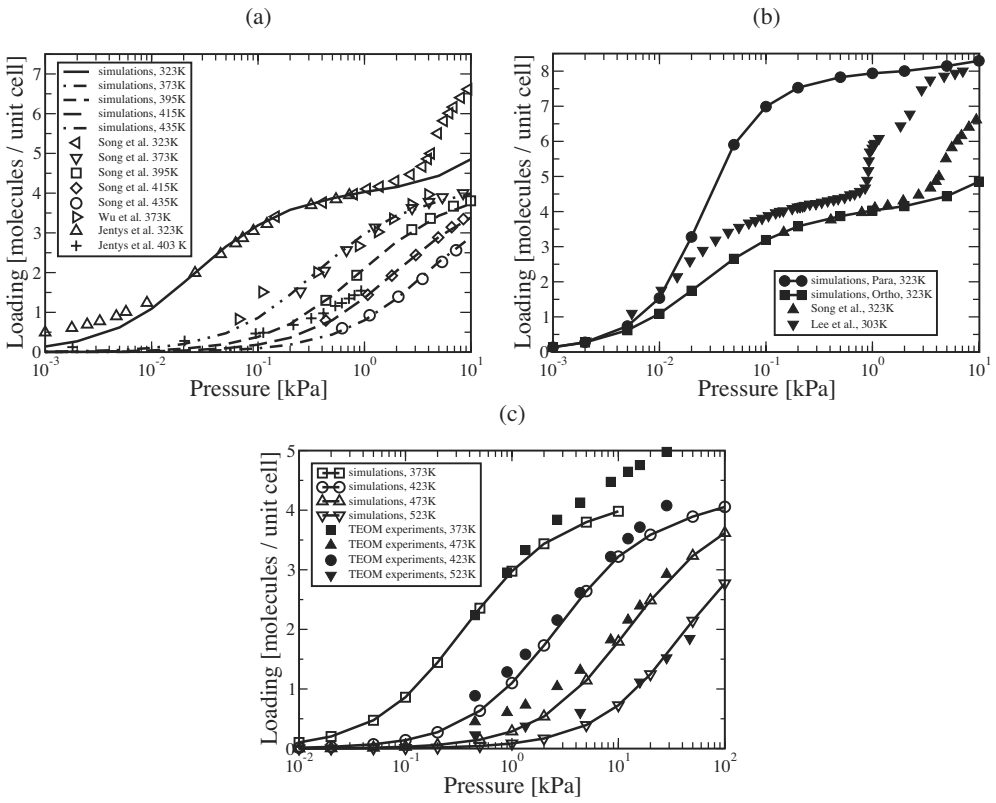

Figure 4.3: (a) Experimental [206–208] and simulated adsorption isotherms of benzene in silicalite (*Ortho* structure) at various temperatures. The lines represent simulation data, and symbols are used for experiments. (b) Simulated adsorption isotherms for benzene in *Para* and *Ortho* silicalite at 323 K. The experimental isotherms of Song *et al.* [207] at 323 K and Lee *et al.* [209] at 303 K are shown for comparison. (c) Comparison between adsorption isotherms measured using the TEOM technique and simulations (*Ortho* structure).

and TEOM experiments is presented in Fig. 4.3 (b). Excellent agreement is found at loadings lower than 4 benzene molecules per unit cell. Remarkably, the TEOM experiments at 373 K do not show the inflection behavior at 4 molecules per unit cell that was found in other experiments at much lower temperatures (323 K and lower). Note that to the best of our knowledge, there is no experimental adsorption data available in literature at pressures required for such a possible inflection at 373 K. The maximum loading from the experiments agrees well with the computed maximum loading for the *Para* structure (8 molecules per unit cell), see Fig. 4.3 (c). In the *Para* structure, benzene still is preferentially adsorbed at the channel intersections but adsorption in the channel interiors is also possible. The adsorption isotherm of benzene in the *Para* structure does not show inflection behavior at 4 molecules per unit cell.

The isosteric heat of adsorption of benzene in silicalite is shown in Fig. 4.4. Below a loading of four molecules per unit cell, simulations show a constant value of 52 kJ/mol which is in line with experiments. However, at almost zero coverage, the heat of adsorption of Jentys *et al.* [208] is significantly higher (70 kJ/mol) and quickly drops with increasing loading. Jentys *et al.* explained this phenomenon by strong interactions of benzene with defect sites (e.g. SiOH groups), present in silicalite at very low concentrations. Indeed, at low pressure the isotherms from Jentys *et al.* overestimate our computed isotherms (see Fig. 4.3 (a)).

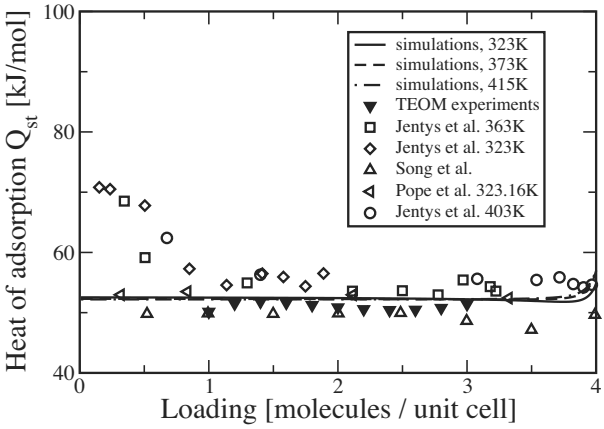

Figure 4.4: Experimental [207, 208, 215] and computed isosteric heats of adsorption of benzene in silicalite at various temperatures. The lines represent simulation data, and symbols are used for experimental data.

Takahashi and co-workers [216] have measured adsorption isotherms for benzene in FAU-type zeolite with a Si/Al ratio of 195. From their isotherms at 393 K and 363 K, we deduct $Q = 33$ kJ/mol and a Henry coefficient $K_H(393\text{K}) = 0.10$ mmol g^{-1}Pa^{-1}. As their data show a good comparison with our simulation results ($Q = 37$ kJ/mol and $K_H(393\text{K}) = 0.080$ mmol g^{-1}Pa^{-1}) we are confident that our benzene force field is suitable for frameworks other than MFI.

Fig. 4.5 shows the adsorption isotherms of benzene and propene in various all-silica frameworks. Mordenite consists of large straight channels (diameter 7 Å) and small side pockets (3.4×4.8 Å) that can be entered from the straight channels. At the temperatures and pressures in this study, benzene and propene are exclusively adsorbed in the straight channels. The adsorption for benzene starts at much lower pressures than for propene as the attractive interactions of benzene with the framework are much stronger. The maximum loading of propene (in molecules per unit cell) is almost a factor 3 larger than of benzene. Zeolite Y is the most open zeolite and consists of 12 Å wide supercages accessible through 7.2 Å windows. This results in a low Henry coefficient and very high maximum loading. Zeolite MCM22 consists of two independent pore systems of 10-membered rings, a large cavity (7.1×18.0 Å) and a channel (4.0×5.5 Å). The

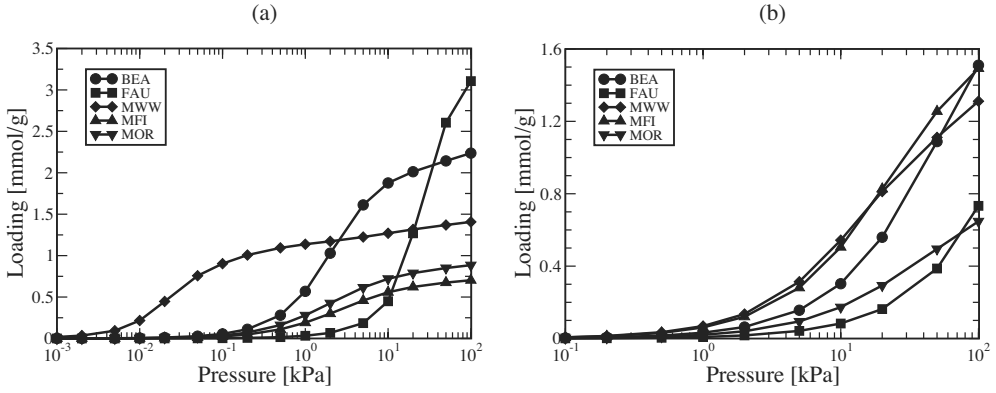

Figure 4.5: Simulated adsorption isotherms of (a) benzene at 423 K and (b) propene at 373 K in zeolite β (BEA), Y (FAU), MCM22 (MWW), silicalite (MFI) and mordenite (MOR).

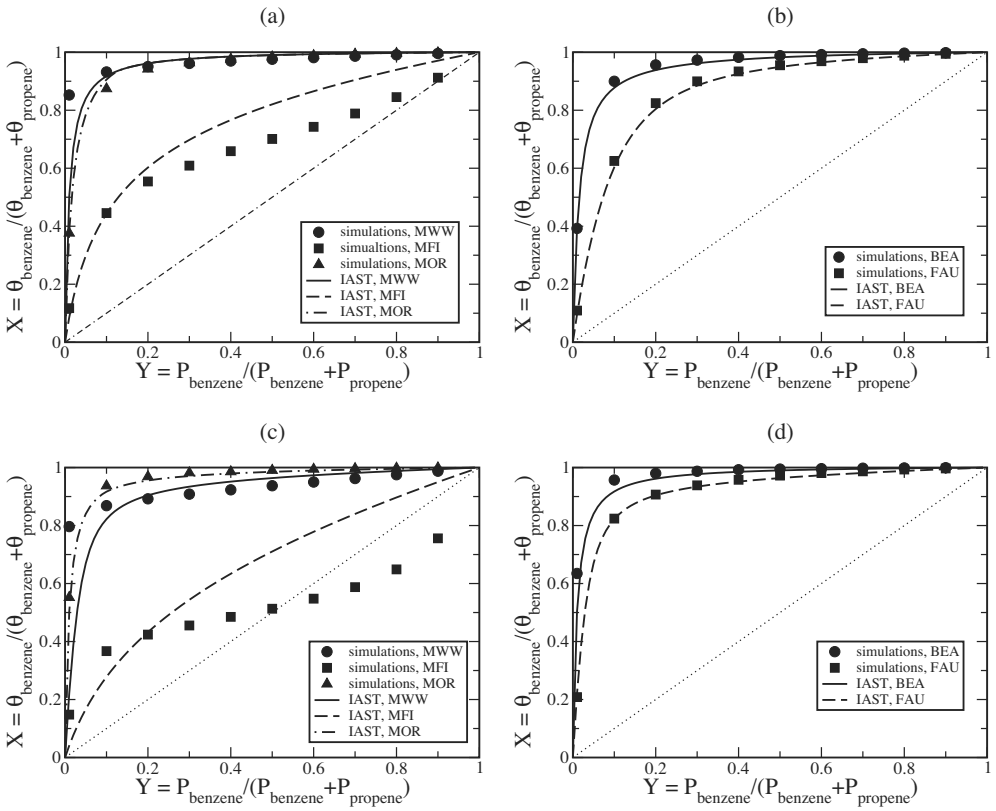

Figure 4.6: x-y diagrams of benzene/propene mixtures in various zeolites (abbreviations as in Fig. 4.5) at 423 K ((a) and (b)) and 373 K ((c) and (d)). Molecular simulations are compared with the IAST. Total pressure $P_{\text{benzene}} + P_{\text{propene}} = 1.0$ bar. θ_i and P_i denotes respectively the loading and partial pressure of component i. The dashed line is the expected result for a-selective adsorption.

cylindrical cavities of MCM22 are much smaller than the more sphere-like cavities of zeolite Y. As the size of benzene is commensurate with the size of the cavity in MCM22, the Henry coefficient (slope of the adsorption isotherm at low loading) is very large.

4.3.2 Adsorption of binary propene/benzene mixtures

The x-y diagrams of benzene/propene mixtures at a total pressure of 1 bar are plotted in Fig. 4.6. A comparison with the Ideal Adsorbed Solution Theory (IAST) of Myers and Prausnitz [217] has been included. Three different types of adsorption behavior can be distinguished. Frameworks BEA, MWW and MOR have a very high selectivity for benzene. In these frameworks, propene and benzene are adsorbed at the same location in the zeolite. As benzene is adsorbed much stronger than propene, the selectivity is very high. As framework FAU has very large cavities, the benzene/propene selectivity is lower and close to the selectivity that one would expect for a liquid. The selectivity for benzene is even lower for framework MFI, and for $T = 373$ K a reversal of the selectivity is observed. We will come back to this issue at the end of this section. The comparison with the IAST is quite good in general except for MFI due to the segregated nature of the adsorbed phase [184, 218].

As can seen from Fig. 4.7, MCM22 is a strong absorbent for benzene. Large amounts of benzene are adsorbed at low pressures (around 1.0 Pa). The adsorption of benzene is hardly affected by propene and therefore the pure component and mixture isotherms for benzene are identical. In

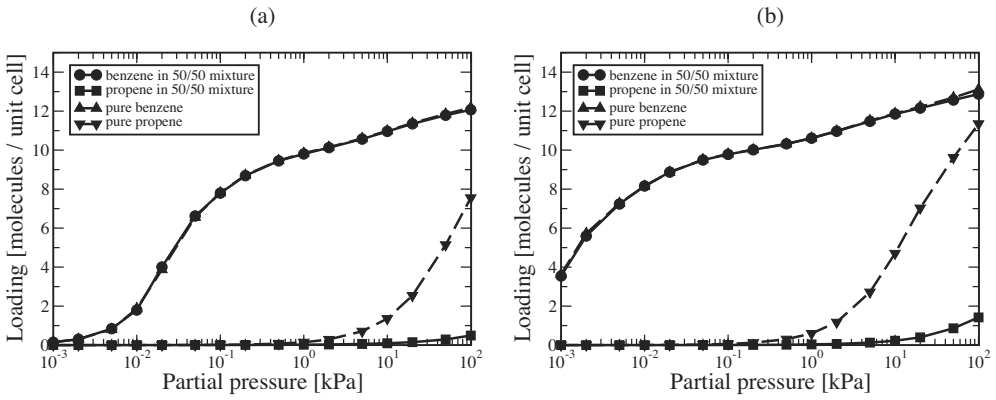

Figure 4.7: Adsorption isotherms of benzene and propene in equimolar (50/50) mixtures comparing with those of pure components in zeolite MCM22 at (a) 423 K and (b) 373 K.

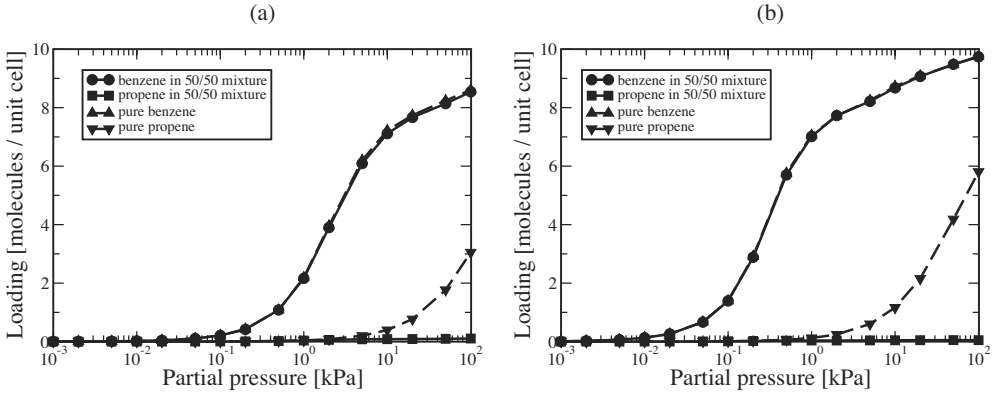

Figure 4.8: Adsorption isotherms of benzene and propene in equimolar (50/50) mixtures comparing with those of pure components in zeolite β at (a) 423 K and (b) 373 K.

the benzene/propene mixture, propene is excluded from the zeolite as benzene is adsorbed much stronger than propene. Due to the presence of the (narrow) channel system in MCM22 (4.0×5.5 Å), a small amount of propene is absorbed in these channels at low temperature. These channels are too small for benzene. The adsorption of propene in the narrow channel system directly results in a lower selectivity for benzene at 373 K (Fig. 4.6 (b)).

A similar feature is found for zeolites β and MOR (Figs. 4.8 and 4.9) that almost exclusively adsorb benzene, independent of temperature. Fig. 4.10 shows the somewhat weaker adsorption of benzene and propene in zeolite Y. At 423 K, the adsorption of benzene starts at 10 kPa, and quickly increases with pressure. Therefore, the adsorption of benzene in zeolite Y is quite sensitive to pressure and this also leads to a lower selectivity for benzene at low partial pressures (Fig. 4.6). This effect disappears at higher partial pressures of benzene. At low partial pressures of benzene, the benzene selectivity in zeolite Y depends more strongly on temperature than the other zeolites (MCM22, MOR, BEA, see Fig. 4.6). The reason for this is that the adsorption isotherm of benzene in FAU is very sensitive to the pressure. Changes in the temperature effectively shift adsorption isotherms and therefore the benzene loading can change significantly with temperature.

The adsorption of benzene/propene mixtures is significantly different in MFI as propene is not excluded from the zeolite, see Fig. 4.11. Instead, the adsorption of propene in 50/50 mixtures is

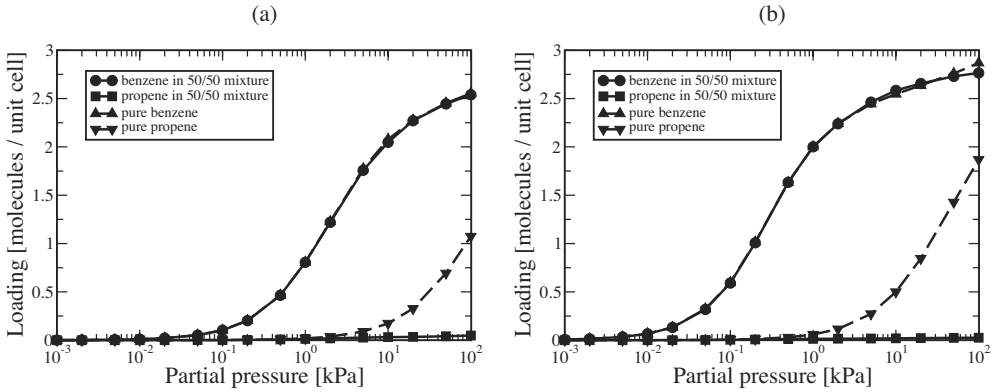

Figure 4.9: Adsorption isotherms of benzene and propene in equimolar (50/50) mixtures comparing with those of pure components in zeolite MOR at (a) 423 K and (b) 373 K.

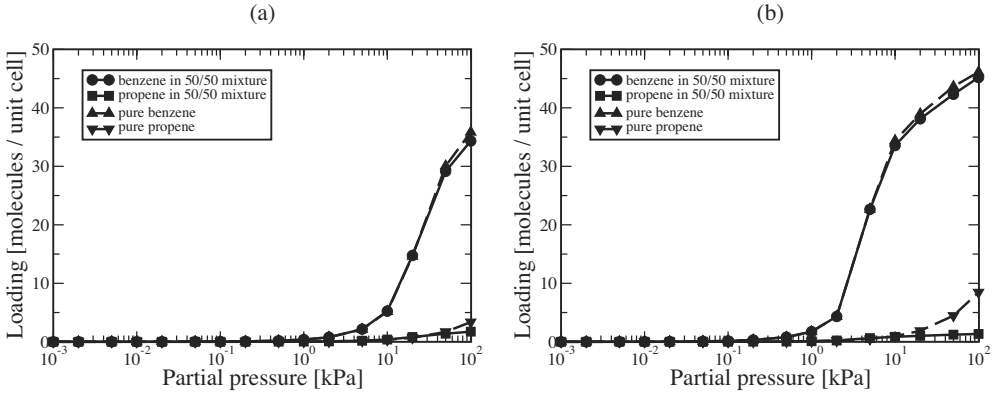

Figure 4.10: Adsorption isotherms of benzene and propene in equimolar (50/50) mixtures comparing with those of pure components in zeolite Y at (a) 423 K and (b) 373 K.

slightly reduced compared to the pure component isotherm of propene. Both the simulations and the IAST suggest a reversal of the selectivity at very high pressure. The adsorption of benzene in the 50/50 mixture is almost identical to the adsorption of the pure component isotherm. This suggests that in contrast to zeolites BEA, MCM22, FAU and MOR, propene is adsorbed at different adsorption sites inside the zeolite. Simulation snapshots show that benzene is preferentially adsorbed at the intersections and that propene can adsorb at both the intersections and the channel interiors (Fig. 4.12(a)). In the presence of benzene, the intersections are occupied by the stronger adsorbing benzene molecules and therefore propene is exclusively adsorbed in the channel interiors (Fig. 4.12(b)), resulting in a somewhat lower adsorption of propene compared to the pure component isotherm.

Fig. 4.6 (b) shows that at 373 K, the selectivity for benzene is even reversed in favor of propene. The reason is that at a total pressure of 1 bar, the loading of benzene is limited by the number of channel intersections. Therefore, as soon as the intersections are filled with benzene, increasing the partial pressure of benzene does not results in a higher loading of benzene, so the x-y diagram will be quite flat for a large range of partial pressures of benzene. This effect will be more pronounced at low temperatures. At higher temperatures, the total loading of benzene is lower than 4 molecules per unit cell and therefore this effect does not play a role.

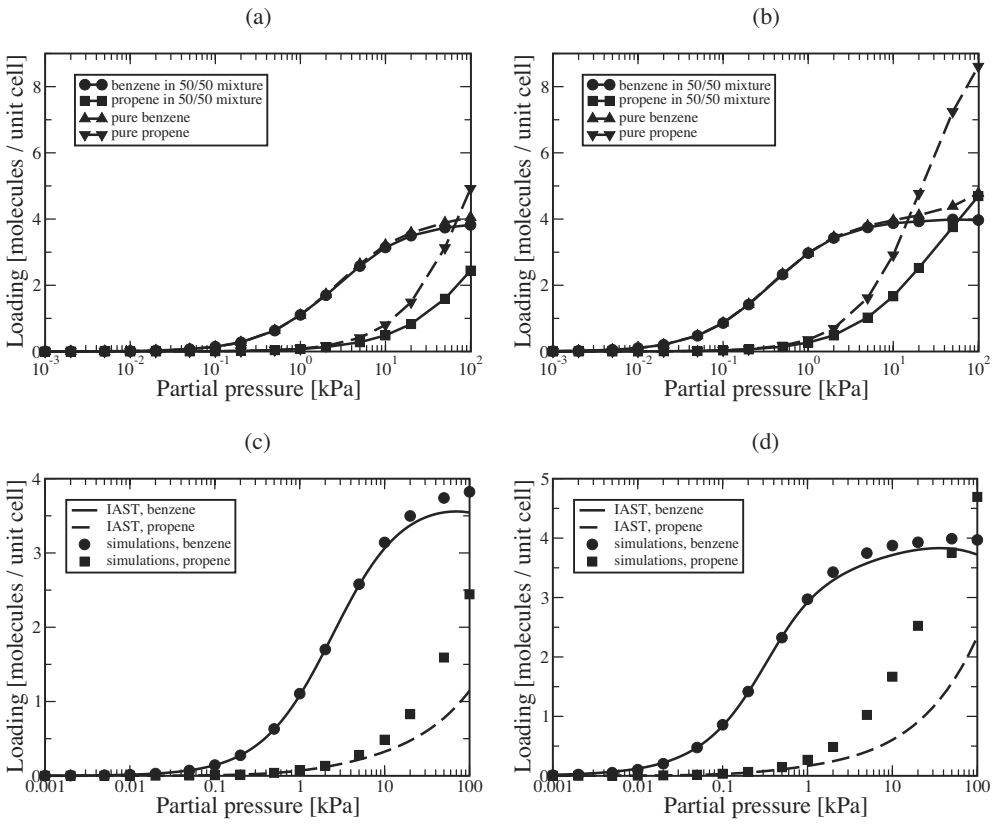

Figure 4.11: Adsorption isotherms of benzene and propene in equimolar (50/50) mixtures comparing with those of pure components in zeolite MFI at (a) 423 K and (b) 373 K. Comparison of the computed mixture isotherms (50/50 mixtures) with the IAST is shown in (c) 423 K and (d) 373 K.

4.4 Conclusions

We have constructed a 9-site force field for the adsorption of benzene in zeolites. The comparison with experimental data revealed a good agreement with our simulations. The selectivity for benzene in benzene/propene mixtures is investigated for various zeolites that have the potential to be used as catalyst for cumene synthesis. High selectivities for benzene are found in zeolite β, MCM22 and MOR. The selectivity of these zeolites is hardly influenced by temperature. Silicalite is not very selective for benzene. Zeolite Y is an intermediate case as the selectivity for benzene is low at low partial pressure and high temperature. A lower temperatures, however, the selectivity for benzene is high at sufficiently high pressure.

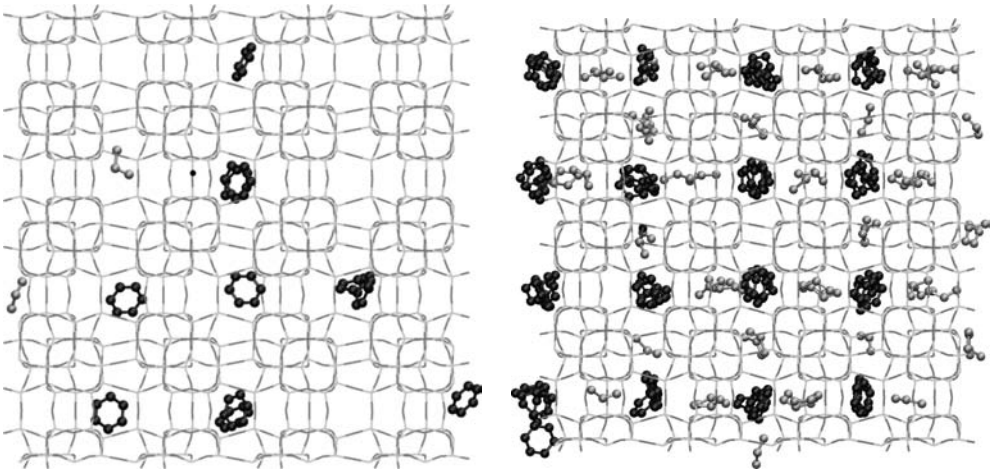

Figure 4.12: Typical snapshots of 50/50 benzene/propene mixtures at low (a) and high (b) total loading.

5

Zeolite microporosity studied by molecular simulation

A simulation method is presented to efficiently calculate the pore size distribution of microporous materials. The microporosity of several typical zeolites is analyzed. The effects of the inaccessible pores and non-framework cations on the pore size distribution of zeolites have also been studied. Molecular simulations of Ar adsorption are used to investigate the correlations between the adsorption isotherms and the pore size distribution. The feasibility to derive the pore size distribution of zeolite micropores directly from adsorption isotherms is discussed.

S. Ban, T.J.H. Vlugt, *Molecular Simulation* (2009), in press. doi:10.1080/08927020802660614

5.1 Introduction

In recent years major progress has been made in the synthesis and textual characterization of highly ordered microporous materials, e.g. microporous molecular sieves [219–221]. Zeolites are important microporous molecular sieves with well-defined crystalline structures [210, 222]. Therefore, the pore structure follows directly from the crystallographic data. Zeolite pores are narrow as the pore width is usually smaller than 1.5 nm. An accurate textural characterization of microporous materials is of crucial importance for their application, for example in catalysis and separation technology [19, 39, 223–225]. The pore architecture, i.e. pore size, pore size distribution, pore volume, and pore topology all have a large influence on adsorption and transport phenomena [115, 155, 226–230]. Although many experimental methods are available for the characterization of porous materials, physical adsorption is still the most popular one as it can access a wide range of pore sizes (from 0.35 nm up to 100 nm) [140]. This includes the complete range from micro- and mesopores to macropores. Moreover, gas adsorption techniques are convenient to use and not cost intensive compared to some other methods such as small angle X-ray and neutron scattering, mercury porosimetry, electron microscopy, thermoporometry and NMR [140].

Physisorption occurs whenever a gas or liquid (the so-called "guest") is brought into contact with the surface of a porous solid ("host"). The amount of adsorbed material (adsorption isotherm) is determined by the applied pressure and temperature, as well as the interplay between the guest-host and guest-guest interactions in the pores. This is reflected in the shape of the adsorption isotherm. The IUPAC classification of adsorption isotherms [231] distinguishes six types of isotherms. Pores are classified by their internal pore width (the pore width of a cylindrical pore is defined by its diameter; for slit pores the pore width is defined as the distance between opposite walls). Pores smaller than 2 nm are classified as micropores, while mesopores have a pore width between 2 and 50 nm. Pores larger than 50 nm are classified as macropores.

In order to extract the surface area, pore size, pore size distribution, pore volume, pore topology and porosity from gas adsorption isotherms, one needs to apply suitable theoretical models that capture the important underlying adsorption mechanisms. Molecular simulations (Monte Carlo and Molecular Dynamics) have been used to obtain a better understanding of sorption phenomena in porous materials [17, 75, 136, 155, 232–242]. These microscopic methods describe the guest-host system at a molecular level, in contrast to classical methods that are based on macroscopic thermodynamic assumptions. It has been shown that the application of theoretical and molecular simulation-based methods leads to a much more accurate pore size analysis over the complete micro and mesopore size range [243–245].

In this work, we present an efficient simulation method to characterize zeolite pores in terms of the micropore size distribution, the micropore volume and the accessibility of micropores. Only the coordinates of the zeolite framework atoms are required, and they can be derived from XRD experiments easily. The details of our approach are presented in the section 2. In section 3, we briefly discuss the pore size distribution of some typical zeolites, and show how this is affected by non-framework cations. We also briefly discuss the fact that for some zeolite structures, some parts are inaccessible. For various framework structures, we study the physisorption of Ar using Monte Carlo simulations in the grand-canonical ensemble. Several models are discussed on how to relate the isotherm of Ar adsorption to the pore size distribution. Concluding remake will be given in section 4.

5.2 Simulation methods

5.2.1 Pore size distribution

In this work, the pore size of a certain cavity is defined as *the maximum diameter of a sphere that can be located in that cavity*. This definition is applicable to pores with an arbitrary shape. For cylindrical or slit pores, our definition is identical to the IUPAC definition. Using our definition of the pore size, the pore size distribution is computed from the coordinates of the framework atoms using the following algorithm shown in Fig. 5.1: *(1)* a three-dimensional grid with a small

spacing is constructed. We typically use a grid size of 0.1 Å (in each direction). *(2)* a spherical test particle is positioned at a random position in the zeolite. The radius of this particle is chosen as the minimum distance between the center of the particle and any of the zeolite framework atoms, minus the radius of the closest framework atom. The radius of an oxygen framework atom is 1.35 Å. Tetrahedral atoms, e.g. *Si*, *Al*, are not considered as for most zeolites they are well screened by adjacent oxygen atoms [142]. *(3)* The diameter of the test particle is recorded for all grid points that are inside the test particle. *(4)* This procedure is repeated many times. We found that the number of test spheres should be at least 100 times the number of gridpoints. For each grid point, the maximum recorded diameter is computed and this quantity is defined as the local pore size of a specific grid point. The simulation stops when the local pore size of all gridpoints is converged. *(5)* The fraction of pores with a diameter between r and $r+\Delta r$ (pore size distribution) is equal to the fraction of gridpoint with a maximum diameter between r and $r+\Delta r$. Note that the channel dimensions of zeolites suggested by Atlas of Zeolite Structures [1] are actually the sizes of the channel openings, directly related to the accessibility. This definition of pore size is slightly different compared to ours.

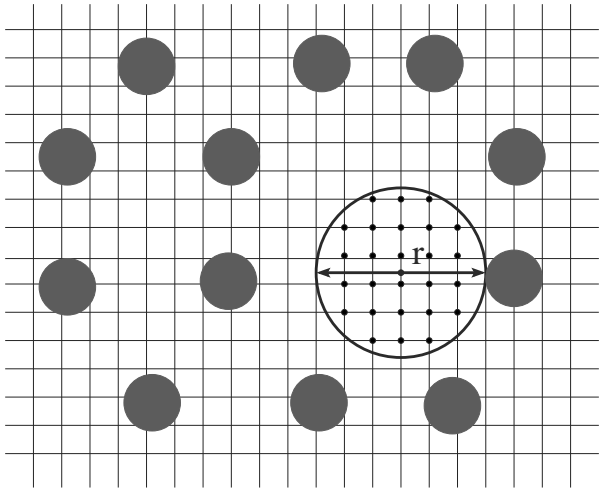

Figure 5.1: Schematic representation of the simulation scheme to compute the pore size distribution of porous materials. The large spheres are the zeolite atoms, and the circle represents the particle inserted randomly in the zeolite framework. The dark dots are the grid points inside the inserted particle with a diameter r.

N_2/Ar physisorption experiments are the most often methods to measure the total pore volume experimentally. These methods can only detect the pores larger than 4.5 Å [220]. Using our calculated pore size distribution, the micropore volume is calculated by integrating the pore size distribution up to 20 Å, starting from pore sizes of 4.5 Å or 3.5 Å. It is important to note that some zeolites (e.g. LTA-type zeolite) may contain inaccessible cavities, that are (in principle) large enough to accommodate adsorbate molecules. In this case, the largest entrance to the cavities is often a small six membered ring. The contribution of the inaccessible cavities to the total micropore volume should be subtracted, depending on the size of the guest molecules. In this work, we will try to establish a relation between the pore size distribution and adsorption isotherms computed using molecular simulations. Therefore, to make this comparison it is not necessary to artificially block inaccessible cages. However, for a comparison between computed isotherms and measured isotherms one needs to take care that in the simulations, the inaccessible cages are really inaccessible for guest molecules.

5.2.2 Ar physisorption

Gas physisorption is the most popular method for the characterization of pore sizes as it allows accessing a wide range of pore sizes (from 0.35 nm to 100 nm). Ar shows nearly perfect physisorption behavior at cryogenic conditions (87.3 K) [231]. Compared to N_2 and CO_2, Ar has weaker attractive interactions with the host structure, in particular for zeolites with non-framework cations [246]. As a consequence, micropores of $0.5- \sim 1$ nm are filled with Ar at much higher relative pressures, i.e. $10^{-5} < p/p_0 < 10^{-3}$ than for N_2 (p_0 being the saturation pressure). However, analysis of Ar physisorption is problematic for small zeolite micropores. The reason for this is that when the pore size is close to the kinetic diameter of Ar, the local density of Ar inside zeolite micropore becomes smaller than the density of liquid Ar due to confinement effects. Therefore, the pore volume can not be computed directly from the density of liquid Ar as this will lead to an underestimation of the micropore volume.

In this study, simulations of Ar adsorption in zeolites at 77 K are conducted. This will be used to develop the correlation between the Ar adsorption isotherms and the simulated micropore size distributions. Adsorption isotherms are calculated using Monte Carlo simulations in grand-canonical ensemble, for details we refer the reader to Refs. [77, 84, 138, 201]. Lennard-Jones (LJ) interactions are used to describe interactions between Ar and zeolite atoms. The intermolecular interactions are truncated and shifted at 12 Å [81]. Periodic boundary conditions in all directions are applied. The pressure is varied between 10^{-5} and 10^2 kPa at 77 K. A typical simulation consists of at least 2×10^6 cycles. In each cycle, trial moves are attempted to translate or to exchange a molecule with the reservoir [84]. The number of trial moves per cycle is equal to the number of molecules with a minimum of 20. As we want to make a comparison between the computed pore size distribution and the computed adsorption isotherms, it is not necessary to identify or block inaccessible cages. We would like to point out that for comparison with experimental isotherms it is necessary to block inaccessible cages in the simulations.

In our simulations, the zeolites are considered rigid as framework flexibility only results in very small deviations of adsorption properties [72]. For MFI-type zeolite however, a phase transition of the zeolite framework may occur upon Ar adsorption [151, 247–250]. A detailed study of this is beyond the scope of the present work. In our adsorption simulations, all zeolites are considered as all-silica structures. The Lennard-Jones interaction parameters are chosen as $\sigma_{\mathrm{Ar-Ar}} = 3.42$ Å, $\varepsilon_{\mathrm{Ar-Ar}}/k_B = 124.07$ K, $\sigma_{\mathrm{Ar-O}} = 3.17$ Å and $\varepsilon_{\mathrm{Ar-O}}/k_B = 95.61$ K [251]. The Lennard-Jones interaction between *Si* and Ar is not taken into account [252].

The Dubinin-Astakhov (DA) adsorption equation was used to model the filling of a pore of diameter r [253]:

$$N(r,p) = \rho(r) \exp\left[-\left(\frac{RT ln(p_0/p)}{\alpha E_0(r)} \right)^{n(r)} \right] \tag{5.1}$$

in which $N(r,p)$ is the loading of adsorbed molecules at pressure p, ρ (in units of mmol/ml) is the saturation loading of Ar in pores of diameter r, $P(r)$ is the pore size distribution in units of ml g^{-1} $Å^{-1}$, α is the (dimensionless) affinity parameter (0.31 for Ar [253]), E_0 is the characteristic adsorption energy (kJ/mol), p_0 is the saturation vapor pressure, and $n(r)$ is a constant that only depends on r. The total loading $\theta(p)$ of Ar in the zeolite is computed by integration over all pores [244, 245, 254–256],

$$\theta(p) = \int_{r=3.5\text{Å}}^{r=20\text{Å}} P(r')N(r',p)dr' \tag{5.2}$$

This integration is from the minimum considered pore diameter 3.5 Å to the maximum pore diameter of micropores (20 Å). In total, three parameters depend on the pore diameter r: $\rho(r)$, $E_0(r)$ and $n(r)$. The function $\rho(r)$ determines the saturation loading at which the adsorption isotherm levels off. The adsorption energy $E_0(r)$ determines at which pressure the guest molecules start to enter the zeolite cavities. The function $n(r)$ defines the slope of the isotherm prior to saturation.

For a large collection of zeolites, we have fitted $\rho(r)$, $E_0(r)$ and $n(r)$ using the pore size distribution computed using the scheme described in section 5.2.1. This is done as follows: *(1)* For zeolites with only one pore type or adsorption site, the value of $\rho(r)$ can be computed directly

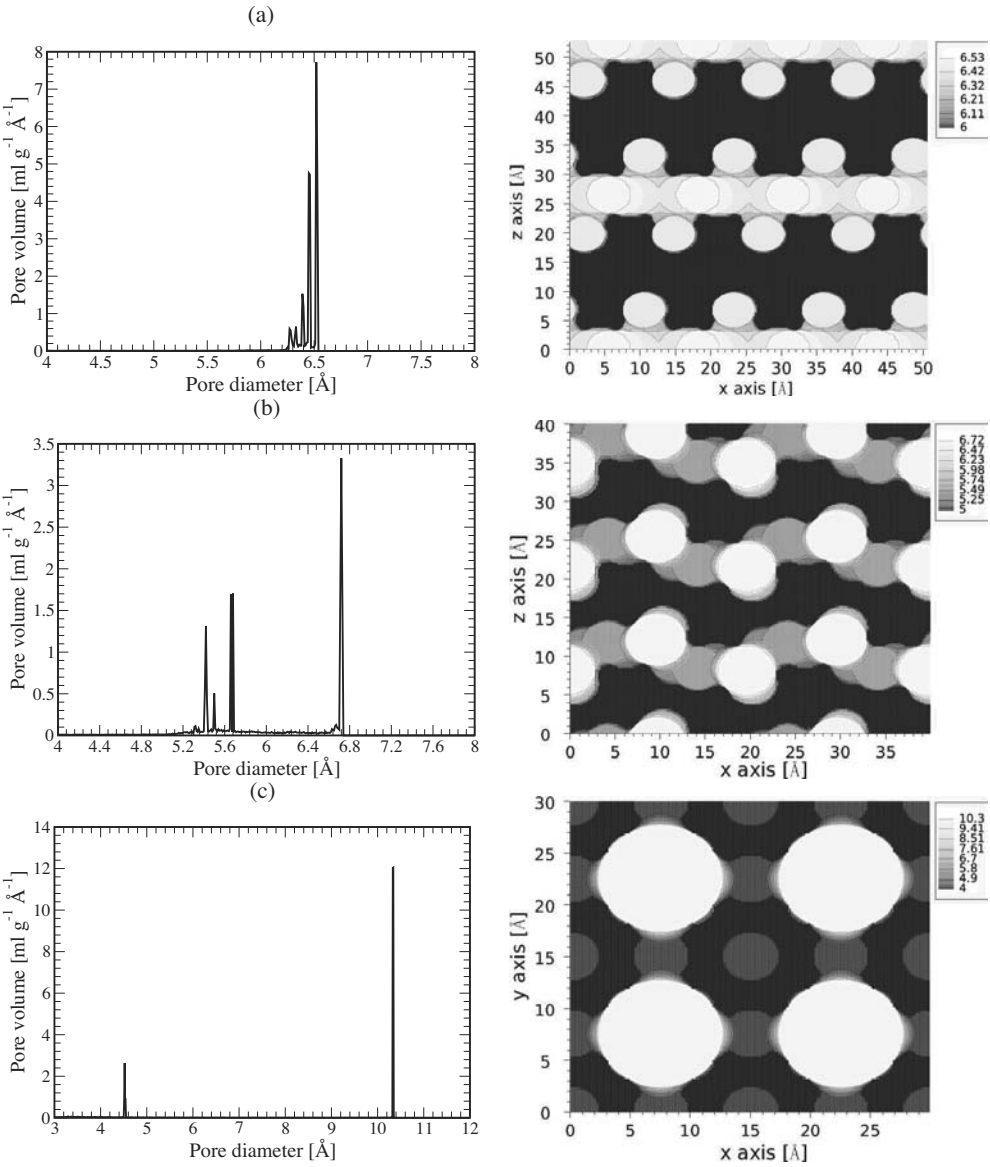

Figure 5.2: Left: Computed pore size distributions of various zeolites: *(a)* BEA, *(b)* MFI and *(c)* RHO. Right: corresponding contour plots for BEA, MFI and RHO. The contour planes are chosen as follows: *x*-*z* plane at $y = 0.75b$ for BEA, *x*-*z* plane at $y = 0.25b$ for MFI and *x*-*y* plane at $z = 0.5c$ for RHO (a, b, c being the length of the basisvectors of the unit cell). The color of the contour maps denotes the pore diameter. The dark area in the contour plots denotes cavities with a pore diameter smaller than 6 Å for BEA, pore diameters smaller than 5 Å for MFI and pore diameter smaller than 4 Å for RHO.

from the pore volume and the saturation loading. Some care is needed for zeolites with more than one pore type. In this case, we identify the number of adsorption sites by the inflection behavior [83, 257]. If the inflection behavior is absent, then we only consider a single adsorption site. Inflection behavior of the adsorption isotherm is not necessarily caused by the presence of multiple adsorption sites, as it may also be caused by rearrangement of the guest molecules. Simulation

snapshots have been used to identify whether or not multiple adsorption sites are present. *(2)* The other parameters $E_0(r)$ and $n(r)$ are fitted to the computed adsorption isotherm. *(3)* The fitting procedure is repeated for many zeolites and we will investigate general trends in the obtained values for $\rho(r)$, $E_0(r)$ and $n(r)$.

From the functions, $\rho(r)$, $E_0(r)$ and $n(r)$, now fitted for all zeolites, we will investigate whether or not it is possible to predict the earlier computed pore size distribution from the computed adsorption isotherm. This is done as follows. For pore diameters r in the range ($4- \sim 13$ Å), the corresponding pore volume equals $\theta(p_0)/\rho(r)$. We compute the absolute error between the computed isotherm (using GCMC) and the fitted isotherm (calculated using Eqs. 6.1,6.2 and the functions $\rho(r)$, $E_0(r)$ and $n(r)$ fitted for all zeolites simultaneously). The pore diameter that leads to the smallest difference is selected. For zeolites with more than one adsorption site, the simulated Ar adsorption isotherm is separated using the inflection pressure corresponding to the adsorption of Ar in different pore types. The pore diameters that lead to the smallest difference between the computed and fitted isotherm are selected.

5.3 Results and discussion

5.3.1 Micropores of all-silica zeolites

The pore size distributions have been computed for most of zeolite structures taken from IZA zeolite database [1]. The total micropore volume is calculated by integrating the pore size distribution in the range of pore diameters $3.5- \sim 20$ Å and $4.5- \sim 20$ Å. Results for typical all-silica zeolites are listed in Table 5.1. It is trivial to see that the pore volume integrated from 3.5 Å ($V_{3.5}$) is slightly larger than the pore volume integrated from from 4.5 Å ($V_{4.5}$). In particular, MON-type zeolite has an unique 4 Å pore, which leads to $V_{4.5} = 0$.

Detailed information of the zeolite porosity for BEA, MFI, RHO can be seen in the pore size distributions and the corresponding contours in Figure 6.11. Zeolite BEA has two different channels running along the crystallographic x and y axis respectively. The sizes of these channel openings are 6.6×6.7 Å and 5.6×5.6 Å. The simulated pore size distribution for zeolite BEA in Fig. 6.11 (a) shows a slightly disperse pore size ranging from 6.25 to 6.55 Å, corresponding to the channel interiors shown from the contour plot. In Figure 6.11 (b), the pore size distribution of MFI shows a large peak at 6.7 Å and some smaller ones between 5.4 and 5.7 Å. The corresponding contour map suggests that the large peak corresponds to the intersections of the straight channel

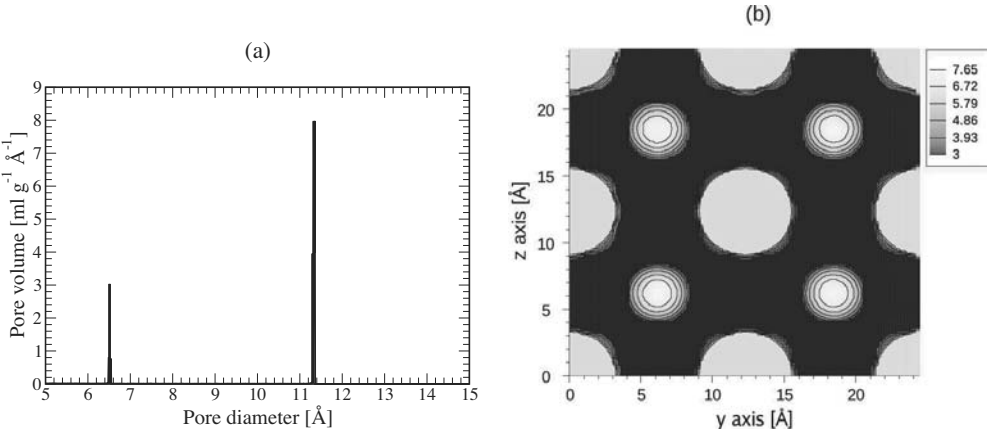

Figure 5.3: (*a*) Computed pore size distribution and (*b*) the contour map for the LTA-type zeolite. The contour plane is chosen as y-z plane at $x = 0.5a$. The color of the contour maps denotes the pore diameter. The dark area in contour plot denotes cavities with a pore diameter smaller than 3 Å.

Zeolite Type	$V_{3.5}$ [ml/g]	$V_{4.5}$ [ml/g]	Zeolite Type	$V_{3.5}$ [ml/g]	$V_{4.5}$ [ml/g]
AEL	0.136	0.126	AET	0.172	0.165
AFI	0.192	0.184	AFO	0.129	0.119
AFR	0.341	0.280	AFS	0.405	0.366
AFY	0.489	0.452	ATN	0.179	0.149
ATO	0.118	0.107	BEA	0.322	0.314
BOG	0.299	0.286	BPH	0.289	0.273
CHA	0.357	0.332	EAB	0.299	0.281
EUO	0.192	0.179	FER	0.225	0.210
GME	0.357	0.315	KFI	0.344	0.315
LEV	0.324	0.303	LTN	0.304	0.261
MAZ	0.282	0.221	MEI	0.387	0.351
MEL	0.210	0.198	MER	0.308	0.120
MFI	0.211	0.201	MFS	0.199	0.164
MON	0.200	0.000	MOR	0.238	0.208
MTT	0.126	0.106	MWW	0.270	0.253
OFF	0.301	0.289	RHO	0.381	0.350
TON	0.134	0.121	VFI	0.337	0.328
AWW	0.246	0.230	CAN	0.247	0.136
DDR	0.249	0.226	ERI	0.293	0.281
EMT	0.452	0.439	FAU	0.481	0.468
LTA	0.457	0.440	LTL	0.211	0.203

Table 5.1: Micropore volumes of various all-silica zeolites computed using the scheme described in section 5.2.1. Zeolite framework coordinates were taken from the IZA zeolite database [1]. V_x denotes the micropore volume calculated in the range $x \sim 20$ Å. Zeolites in the bottom table contain cages that are inaccessible for most guest molecules. To calculate the density of the zeolite (in g/ml), all framework atoms other than Si have been replaced by Si. Note that this only influences the value for the pore volume per gram zeolite, and not the pore volume per unit cell. Non-framework cations have not been considered here.

(5.3×5.6 Å) and the zigzag channel (5.1×5.5 Å). Peaks in the range of $5.4- \sim 5.7$ Å represent the channel interiors of MFI. The RHO-type framework has a cage-like structure, where large *Ita* cages are connected by small eight-membered rings (3.6×3.6 Å). The pore size distribution of RHO shows two sharp peaks at pore diameter 12 Å and 4.5 Å respectively. The corresponding contour map indicates that the cage interiors with a pore diameter 12 Å and the small windows in size of 4.5 Å have the largest contribution to the pore volume.

As mentioned earlier, the zeolite framework may contain inaccessible cages which consist of six membered (or smaller) rings. As the six membered opening is smaller than 3 Å, it will prevent most molecules with a kinetic diameter larger than 3 Å to enter the cage. The LTA zeolite has two types of cages: (1) the *sod* cage consisting of four and six membered rings; and (2) the *ita* cage possesses extra eight membered rings which make it accessible [1]. From the contour map in Fig. 5.3 (b), it can be seen that there are four *sod* cages located in the center, edges and corners on the *y*-*z* slice of a LTA unit cell. The pore size distribution in Fig. 5.3 (a) shows two pores of diameters 6.5 and 11.3 Å, corresponding to the interiors of the inaccessible *sod* cage and the accessible *ita* cages. The total pore volume larger than 3.5 Å equals 0.457 ml/g. This volume decreases to 0.347 ml/g when the contribution of the *sod* cage is excluded.

Compared to all-silica zeolites, many zeolites have much more complex compositions, as they may contain framework atoms like *Al*, *P*, *Co* and non-framework compounds like *Li*, Na, *Ca*, *Mg* and H_2O etc. Non-framework cations occupy a certain volume and therefore they influence the pore size distribution. Fig. 5.4 shows the effect of non-framework Na cations on the pore size distribution of Na-MOR framework in the *Pbcn* space group. The framework of MOR consists of two distinct cavities, which are twelve membered main channels (7.0×6.5 Å) in the direction

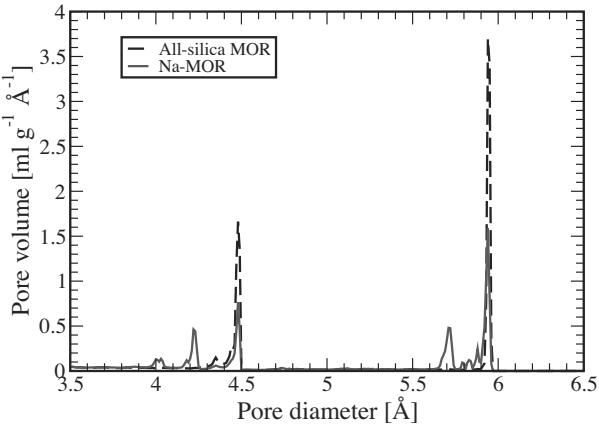

Figure 5.4: Simulated pore size distributions for all-silica MOR and Na-MOR with $Si/Al = 5$. The pore size distribution of Na-MOR is obtained by averaging ten Na-MOR samples with $Si/Al = 5$. The non-framework Na cations are preferentially located at three adsorption sites: the main channels, the opening of the side pocket and the eight membered rings [144, 258].

of the z axis and eight membered side pockets (3.4×4.8 Å) in y direction [1]. In Na-MOR, the adsorption of guest molecules is very sensitive to the distribution of aluminum atoms [161, 162]. In our present study, we randomly distribute Al atoms over all tetrahedral sites of the Na-MOR supercell, in such a way that the Löwenstein rule as well as the guidelines outlined by Alberti et al. [126] are satisfied. This fixes the *Al* content for each of the crystallographic T-sites in MOR-type zeolite. The pore size distribution of all-silica MOR (*Pbcn*) has two major peaks at pore diameters of 4.5 and 5.9 Å, corresponding to the side pocket and the main channel, see Fig. 5.5 (a). When non-framework Na cations present, both peaks become 60% lower than those of the all-silica MOR, while some minor peaks appear at smaller pore diameters around 4.2 and 5.7 Å. The reason for this is that non-framework Na cations make the pore less uniform. This can be seen from Fig. 5.5 (b). This figure also shows that non-framework Na cations sitting near the opening of the side pockets partially or fully block the entrance of the side pockets, and narrow the main channels to some extent. The pore volume ($V_{3.5}$) of the all-silica MOR is 0.199 ml/g ($0.35V_{\text{unitcell}}$) and that of Na-MOR decreases to 0.176 ml/g ($0.327V_{\text{unitcell}}$, V_{unitcell} being the volume of the unit

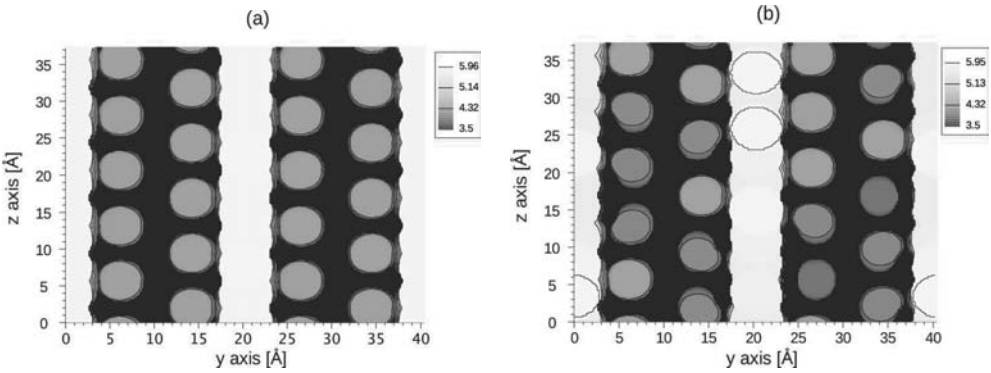

Figure 5.5: (*a*) Typical snapshots of simulated contours for the all-silica MOR and Na-MOR with $Si/Al = 5$. The contour planes are chosen as the y-z plane at $x = 0.5a$. The color of the contour maps denotes the pore diameter. The dark area in contour planes denotes cavities with a pore diameter smaller than 3.5 Å.

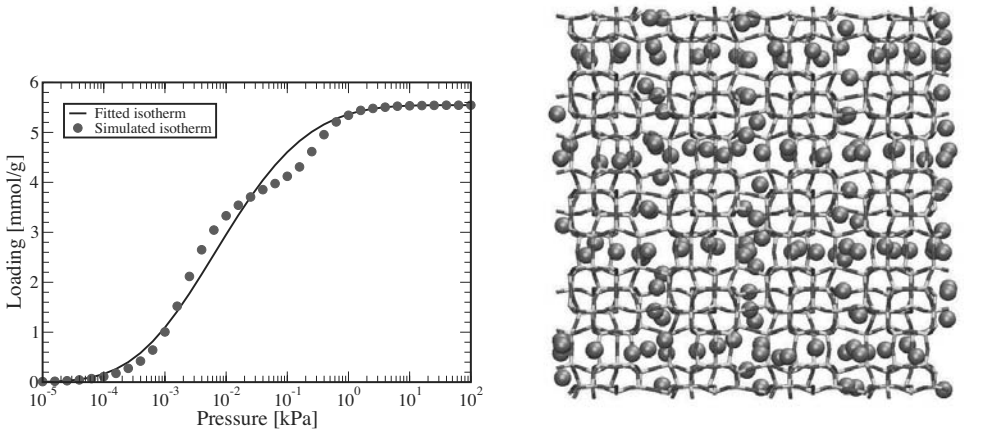

Figure 5.6: Left: Adsorption isotherms of Ar in MFI-type zeolite, along with a fit to Eqs. 6.1,6.2. Right: Typical snapshot (x-y plane) at 0.01 kPa at 77 K.

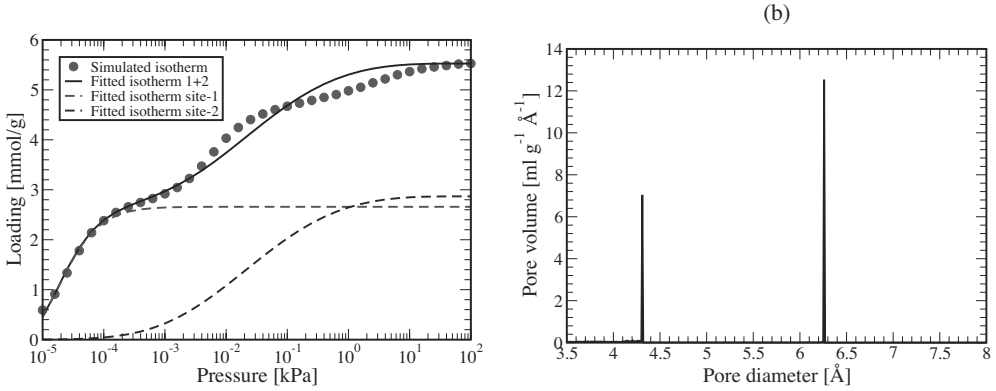

Figure 5.7: Left: Simulated adsorption isotherms of Ar in CAN at 77 K. The dashed lines are the fitted isotherms for the two distinct adsorption sites. Right: the calculated pore size distribution of CAN. The blocking of the inaccessible cages is not considered.

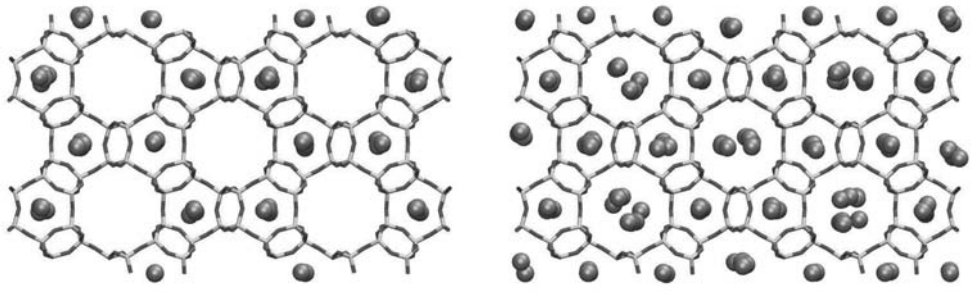

Figure 5.8: Typical snapshots (x-y plane) of Ar adsorbed in CAN-type zeolite at a pressure of 2.5×10^{-4} kPa (left) and 10^2 kPa (right). The blocking of the inaccessible cages is not considered.

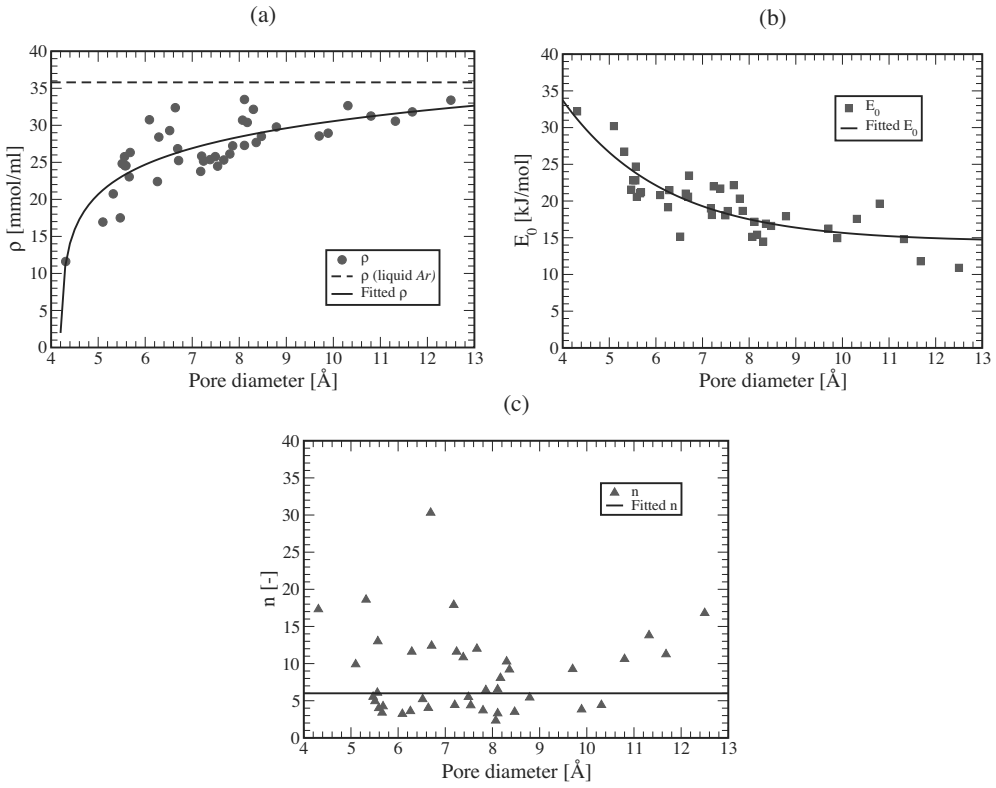

Figure 5.9: The fitted parameters for the DA adsorption isotherm, i.e. ρ, E_0 and n, as a function of the pore diameter in the range from 4 to 13 Å for various zeolites. In Fig. (a), the density ρ of the liquid Ar (35.8 mmol/ml) is drawn as a dashed line.

cell). This indicates that non-framework Na cations occupy the void space of zeolites and cause a volume loss of $0.023V_{\text{unitcell}}$. For a fixed *Al* content of the four T sites, we found only very small differences in the total pore volume for different distributions of Al atoms. However, for a different Al content of the T-sites, the pore volume will be different due to a different fraction of Na in the side pockets.

5.3.2 Ar physisorption

The computed adsorption isotherm of Ar in MFI-type zeolite at 77 K is plotted in Fig. 5.6, along with its fit to Eqs. 6.1,6.2. The computed adsorption isotherm shows an inflection point at 0.01 kPa. The pore size distribution in Fig. 6.11 shows that MFI has two different pores at 5.5 and 6.7 Å, corresponding to the channel interiors and channel intersections respectively. In principle, from the isotherm only, one may relate the inflection to different adsorption capacities of different adsorption sites. However, a simulation snapshot of Ar at 0.01 kPa (Fig. 5.6) shows that both the channel interiors and intersections are simultaneously filled by Ar molecules. The step-like behavior of the Ar adsorption isotherm in these simulations is therefore not caused by the Ar adsorption in *different* pores of MFI [247]. Therefore, it is convenient here to consider MFI as a zeolite containing a single adsorption site. The fitted isotherm agrees well with the isotherm for simulations. The fitting parameters are $\rho = 26.33$ mmol/ml, $E_0 = 21.21$ kJ/mol and $n = 4.24$ at the selected diameter 5.7 Å. The typical pore diameter is chosen from the major peaks of the pore

size distribution, which covers the largest pore volume.

The typical fitting results for Ar adsorption in zeolite CAN at 77 K are shown in Fig. 5.7. Similar to MFI, the adsorption isotherm of Ar in CAN shows two inflection points at the pressure of 10^{-4} and 1 kPa respectively. The snapshots of the simulations (Fig. 5.8) confirm that the first inflection point at 2.5×10^{-4} corresponds to saturation of the small *can* cages (4.3 Å), while the second inflection at 1 kPa is attributed to the packing of Ar in the large channels along z axis. Therefore, two different DA isotherms are used to fit the complete isotherm. For the *can* cages, the fitted parameters are $\rho = 11.61$ mmol/ml, $E_0 = 32.21$ kJ/mol and $n = 17.31$ using a pore diameter 4.3 Å. For the large channel, the fitted parameters are $\rho = 22.40$ mmol/ml, $E_0 = 19.15$ kJ/mol and $n = 3.60$ for a pore diameter 6.3 Å. By comparing the two sets of DA parameters, it can be seen that the large channel always has a higher loading capacity but weaker adsorption strength than the small pore. Note that the parameter n is much more sensitive to the pore shape and the molecular packing than the other parameters.

This fitting of computed isotherms to Eqs. 6.1, 6.2 was conducted for nearly forty zeolite frameworks types. The collection of the fitted DA parameters in the range of $4- \sim 13$ Å are shown in Fig. 5.9. In Fig. 5.9 (a), the general trends can be identified for $\rho(r)$ and $E_0(r)$. Fluctuation in their values is caused by the dependence of the zeolite adsorption on the pore shapes and the molecular packing.

Starting from a pore diameter of $r = 4$ Å, $\rho(r)$ has a sharp increase up to 25 mmol/ml at 6 Å followed by a slow convergence to 33 mmol/ml at the pore diameter 13 Å. Furthermore, at the maximum micropore diameter 20 Å, ρ equals 35.6 mmol/ml, which agrees well with the standard density of the liquid Ar (35.8 mmol/ml). This means that Ar will stay in the liquid phase when the pore is large enough. However, for zeolite micropores smaller than 20 Å, calculation of the micropore volume using the density of liquid Ar (35.8 mmol/ml) will result in an underestimation of the pore volume up to about 30%. For the adsorption energy $E_0(r)$, a reverse trend can be observed. Starting from a large adsorption energy of 34 kJ/mol at $r = 4$ Å, E_0 gradually decreases and levels off around 15 kJ/mol at the diameter 13 Å. This is because small pores have a stronger adsorption strength than large pores. The slope parameter $n(r)$ plotted in Fig. 5.9 (b) shows a larger scatter due to the large sensitivity on the adsorption isotherm.

The collected DA parameters in the range of $4- \sim 13$ Å for Ar at 77 K can be fitted using:

$$\rho(r) = 5.04\ln[r-4.18]+21.68 \quad (5.3)$$

$$E_0(r) = 121.37\exp[-0.46r]+14.45 \quad (5.4)$$

$$n(r) = 6 \quad (5.5)$$

in which r is the pore diameter in Å, ρ and E_0 are in units of mmol/ml and kJ/mol respectively. From the concentration parameter $\rho(r)$ in Eq. 6.3, it can be seen that the minimum pore diameter that can be estimated from the Ar adsorption isotherm is about 4 Å, and any pores smaller than that exceed the measurement capability of the Ar physisorption.

Using the fitted DA adsorption parameters of Eqs. 6.3, 5.4, 5.5, we re-computed the pore volume and pore size of zeolites directly from the computed Ar adsorption isotherms, and compared the results to the direct computation using the algorithm described in section 5.2.1. Nearly forty framework types have been tested in this way, see table 5.2. For most zeolites, the pore volume and size are correctly reproduced compared to the pore size distributions simulated earlier (using the method of section 5.2.1). In general, this procedure is more accurate for zeolites containing a single adsorption site than for zeolites containing multiple adsorption sites. For the latter, the difficulty is that the adsorption isotherms may contain inflections corresponding to the self packing of Ar. To identify the number of the adsorption sites prior to fitting the adsorption isotherms requires knowledge of the zeolite structure. Many zeolites may be subject to some severe chemical pretreatments. This can amorphize the zeolite framework into a less well-defined structure.

Zeolite Type	Adsorption Sites	Fitted V [ml/g]	Calculated $V_{3.5}$ [ml/g]	Fitted r [Å]	Calculated r [Å]
AEL	1	0.142	0.136	5.6	5.6
AET	1	0.170	0.172	13.0	8.3
AFI	1	0.179	0.192	8.7	8.1
AFO	1	0.138	0.129	5.8	5.6
AFR	2	0.397	0.341	4.8, 9.6	4.4, 8.1
AFS	1	0.375	0.405	9.5	9.7
AFY	1	0.477	0.489	8.0	8.5
ATN	1	0.182	0.179	5.4	5.7
ATO	1	0.083	0.118	6.1	5.5
AWW	1	0.231	0.246	6.2	7.4
BEA	1	0.301	0.322	10.9	6.5
BOG	2	0.270	0.299	5.2, 7.7	7.2, 8.4
BPH	1	0.307	0.289	7.7	8.8
CAN	2	0.324	0.247	4.4, 8.4	4.3, 6.3
DDR	1	0.291	0.249	5.8	7.7
EAB	1	0.268	0.299	7.2	7.5
EUO	1	0.246	0.192	5.9	6.7
FAU	1	0.439	0.481	13.0	11.7
FER	1	0.235	0.225	5.7	5.5
GME	2	0.350	0.357	5.3, 7.9	5.0, 7.9
KFI	1	0.399	0.344	7.0	10.8
LEV	1	0.304	0.324	7.4	7.2
LTA	1	0.393	0.457	13.0	11.3
LTL	1	0.201	0.211	9.7	9.9
MAZ	2	0.267	0.282	5.2, 7.3	6.3, 8.1
MEI	1	0.396	0.387	9.1	8.2
MEL	1	0.204	0.210	6.2	5.6
MER	1	0.392	0.308	5.8	6.1
MFI	1	0.225	0.211	6.0	5.7
MFS	1	0.186	0.199	6.1	6.6
MTT	1	0.173	0.126	5.8	5.6
MOR	2	0.274	0.238	4.6, 7.5	5.1, 6.7
MWW	1	0.282	0.270	6.1	7.8
OFF	1	0.280	0.301	7.5	7.5
RHO	2	0.437	0.381	5.0, 9.8	4.5, 10.3
TON	1	0.125	0.134	5.3	5.3
VFI	1	0.345	0.337	13.0	12.5

Table 5.2: Comparison of fitted pore volumes (V) and pore sizes (r) and the calculated ones for various all-silica zeolites. The calculated pore volume $V_{3.5}$ is calculated using the algorithm described in section 5.2.1. The fitted pore volume is obtained by fitting Eqs. 6.1, 6.2 to the adsorption isotherms (computed from GCMC simulations) using Eqs. 6.3, 5.4, 5.5 for ρ, E_0 and n. The pore diameters are obtained in a similar way. Note that the MOR-type framework has space group *Cmcm*.

5.4 Conclusions

A method to characterize the zeolite microporosity has been developed. The pore volume and the pore size distribution of zeolites can be computed accurately. The contour maps of zeolites clearly show the position and diameter of the zeolite pores. In this way, it is possible to easily identify the locations and the local pore volume of the inaccessible cages for some zeolites. The simulations of Na-MOR show that the non-framework Na cations may occupy the internal space and cause a decline for both the pore volume and the pore size compared to all-silica frameworks.

Based on the calculated pore size distributions for various zeolites, adsorption isotherms of Ar have been fitted by the Dubinin-Astakhov (DA) equations. The collection of three DA parameters show clear trends as a function of the pore diameter. By using fitted functions for all three DA parameters, it is possible to identify the pore volumes and the pore sizes directly from the corresponding Ar adsorption isotherm. The fitted results of zeolite microporosities agree well with the ones directly calculated.

6

Insight into the effect of dealumination on mordenite using experimentally validated simulations

Mordenite (MOR-type zeolite) is a widely used catalyst, in particular for (hydro-) isomerization and alkylation reactions in the petrochemical industry. However, having a one-dimensional micropore system, this material is susceptible to diffusion limitations and deactivation. To circumvent this problem, typically additional (meso)porosity is created by applying dealumination and/or steaming processes. The detailed description of the dealumination process is of crucial importance to understand how mordenite can be modified into an efficient catalyst. In this work, we present for the first time a simulation model to describe the influence of the dealumination process on the structural properties of mordenite. Using Kinetic Monte Carlo simulations, dealumination is described as a multiple-step process consisting of the removal of the framework Al as well as the self-healing of silanol nests by Si atoms. The simulation results are in very good agreement with experimental results from ^{29}Si NMR, XRD, and N_2 and Ar physisorption. In particular, the simulations confirm the enlargement of the micropores and the creation of mesopores during dealumination.

S. Ban, A.N.C. van Laak, J. Landers, A.V. Neimark, P.E. de Jongh, K.P. de Jong, Thijs J.H. Vlugt, submitted.

6.1 Introduction

Materials with hierarchical pore systems are of importance in fields such as catalysis, adsorption and drug delivery [259]. Zeolites are prime examples, in particular those zeolites that combine micropores with mesopores, often referred to as mesoporous zeolites [45, 260–262]. Mesopores are essential to improve the mass transfer characteristics of microporous zeolite crystals. Recently, several new methods to obtain mesoporous zeolites have been developed such as bifunctional templating [263], carbon templating [264–266] and desilication [267, 268]. However, dealumination prevails as the method of choice for zeolite modification to arrive at mesoporosity [45]. Steaming and/or acid leaching of zeolites is used to bring about the desired extent of dealumination.

Mordenite (MOR-type zeolite) is a widely used catalyst, most importantly for cracking, (hydro-) isomerization and alkylation reactions in the petrochemical industry [53]. This zeolite contains one-dimensional straight channels along the z crystallographic axis, usually referred to as main channels, with twelve-membered rings of 6.5×7.0 Å. The main channels are interconnected by side pockets via eight-membered rings (3.4×4.8 Å) along the y crystallographic axis. These side pockets are inaccessible to molecules larger than methane [122, 123]. As a result of the effectively one-dimensional micropore system, mordenite is susceptible to diffusion limitations and deactivation. To circumvent this problem, typically additional (meso)porosity is created by applying dealumination and/or steaming processes [18, 48, 65, 118, 269–271]. These processes change both the acidity and the porosity. The number of Brønsted acid sites, directly related to the number of the framework Al atoms, is being reduced. However, the acid strength of the remaining Brønsted acid sites increases, at least up to a certain Si/Al ratio [272, 273]. Another factor is the change in porosity. Nagano *et al*. [48] showed that dealumination of mordenite leads to an enlargement of the main channels and, even more pronounced, the side pockets. Furthermore, dealumination can create additional mesoporosity. Due to the improved diffusion properties and higher resistance to deactivation, dealuminated mordenite has been proposed for many industrial applications [18, 46, 65]. It is of crucial importance to understand how framework Al is distributed over the zeolite framework, and whether and how this is changed upon dealumination. There are indications that it is possible to preferentially leach Al from specific positions [118, 274], especially from the side pockets. This will have an important impact not only on the size and connectivity of the additionally created pores, but also on the location of the active acid sites for catalysis.

Although dealumination of zeolites is of eminent importance, the molecular details of this process are not well understood. A few model descriptions have been reported in literature. Sokol *et al*. [71] used density function theory to study local framework defects generated by dealumination. Although individual defects are accurately studied on the atomic scale, the changes of the zeolite porosity cannot be extracted from their work. Ding *et al*. [275] adopted Monte Carlo simulations to study the Si-Al connectivity for parent and dealuminated MOR and compared the results with ^{29}Si NMR experiments. This approach only focuses on the Al distribution without considering the structure of the MOR framework explicitly. In order to be able to describe the dealumination process, and its impact on the Al distribution, crystallinity, acidity and porosity, we present in this paper Kinetic Monte Carlo simulations of the dealumination process. First, the framework Al distribution in the simulation is compared to ^{29}Si NMR experiments from literature. Validity of the simulated framework is also provided by a comparison of the simulated and experimental XRD patterns. Second, the dealumination process is described using Kinetic Monte Carlo simulations, providing access to the resulting changes in Si-Al connectivity (directly determining the acidity of the Brønsted acid sites), crystallinity, porosity and pore size distribution. The good agreement between simulation and available experimental data support the validity of our detailed description of the dealumination process. By combining experiments and simulations a more detailed picture can be obtained than is accessible experimentally.

6.2 Methods

6.2.1 Sample preparation

Sodium mordenite supplied by Albemarle Catalysts was ion-exchanged in an aqueous 1M ammonium nitrate solution at 353 K for 24 hours, followed by filtering and washing. Per gram of mordenite 12 ml of ammonia nitrate solution was used. This procedure was repeated twice to ensure complete removal of sodium ions. The sample was then converted from the ammonia form to the proton form by heating to 723 K with a ramp of 1 K/min and a dwell time of three hours. The obtained mordenite sample had a Si/Al ratio of 6. This sample will be referred to as A6. The dealuminated MOR was obtained by treating the parent sample for one hour at 100 °C in 6M HNO_3 followed by calcination at 450 °C for three hours. After repeating this procedure twice, a mordenite sample with a Si/Al ratio of 50 was obtained. This sample will be referred to as A50.

6.2.2 Crystallinity

Crystal size and morphology were determined with a Tecnai FEI XL 30SFEG Scanning Electron Microscope (SEM). For A6 and A50 HMOR samples, powder X-ray diffraction (XRD) patterns were obtained using a Bruker-AS D8 with CoK_α radiation ($\lambda = 0.1789$ nm) in the range of $5^\circ \sim 40^\circ$ 2θ. In this work, the crystallinity is defined as the sum of the intensities of the [330], [150], [241], [202], [350] and [511] diffraction planes, normalized by assuming that this sum for the parent HMOR corresponds to 100% crystallinity [46]. XRD patterns were calculated from simulations using a MOR supercell containing $28 \times 25 \times 68$ unit cells, in the absence of water molecules. A Lorentzian distribution was assumed for the calculated XRD intensities [276]. The full width at half of the maximum intensity was set to 0.08° 2θ. Note that experimentally XRD usually yields diffraction patterns with broader lines due to instrumental broadening, disorder, and/or small crystallite sizes. The isotropic displacement factors are set to 2.5 Å for Si and Al atoms and 5.1 Å for O atoms. To calculate the XRD pattern only scattering by the framework atoms (Si, Al, and O) is taken into account, as the scattering contributions of the protons can be neglected [277].

6.2.3 Porosity

Experimentally the porosity was studied using N_2 and Ar physisorption. N_2 physisorption isotherms were recorded with a Micromeritics Tristar 3000 at 77 K. Prior to the physisorption measurements, the samples were dried overnight at 573 K in a flow of nitrogen. The t-plot method was applied to obtain the micropore volumes and external surface areas. To accurately study the microporosity, Ar physisorption was performed. These measurements were performed at 87 K with an Autosorb-1-C instrument (Quantachrome Instruments) equipped with a high precision pressure transducer (Baratron MKS), which allowed for low pressure measurements in the range of $0.0133 \sim 133$ Pa. The saturation pressure p_0 was measured throughout the entire analysis by means of a dedicated saturation pressure transducer. Low-pressure data points were corrected for the thermal transpiration effect according to a standard procedure [278]. Prior to the adsorption analysis, the samples were outgassed at 300 °C for three hours.

Ar adsorption isotherms were analyzed using NLDFT that allows for the quantification of both micro- and mesopores [279–282]. The NLDFT models have been shown to accurately describe pore size distributions in silica materials that exhibit cylindrical and spherical mesopores, and they have been extended to the micropore region with a lower limit of around 4.5 Å [281, 282]. The pore size distribution has been obtained from the adsorption branch of the isotherm by the hybrid NLDFT kernel composed of metastable adsorption isotherms in spheroidal pores larger than 50 Å and equilibrium adsorption isotherms in cylindrical pores smaller than 50 Å [282]. Thus, this model assumes a representation of the pore network as a system of spheroidal shaped mesopores connected by cylindrical channels, and embedded in a microporous matrix; the micropore shape is assumed cylindrical as well. This assumption seems plausible for mordenite. This hybrid kernel

accurately describes the delay of condensation in mesoscopic voids in the region of adsorption hysteresis and the reversible equilibrium adsorption in micropores and small connecting mesopores.

In the computer simulations, the porosity is computed using a geometric method originally developed to calculate zeolite microporosities [141]. The size of a pore is defined as the maximum diameter of a sphere that fits in the pore. This definition is generally applicable to all pores with an arbitrary structure. The size distribution of the pores is computed as follows: *(1)* a three-dimensional grid is constructed. *(2)* A sphere is positioned at a random position. The radius of this sphere is set as the minimum distance between the center of the sphere and any of the zeolite framework atoms, minus the radius of the closest framework atom. *(3)* The radius of the sphere is recorded for all grid points inside this sphere. *(4)* This procedure is repeated many times. For each grid point, the maximum radius of the sphere is recorded. The simulation stops when the maximum radius for each grid point is converged. *(5)* The fraction of pores with a radius between r and $r+\Delta r$ is equal to the fraction of grid points belonging to spheres with a maximum radius between r and $r+\Delta r$. From this, the pore size distribution $p(r)$ can be computed in units of ml g^{-1} Å^{-1}. The total pore volume follows from the integration of $p(r)$. In N_2/Ar physisorption experiments, the smallest pore that can be detected is larger than 4.5 Å [220]. Electron tomography does not show mesopores larger than 100 Å [283]. We hence compute the total pore volume by integration of $p(r)$ from 4.5 to 100 Å. Note that even though the standard IUPAC classification defines micropores as pores smaller than 20 Å, here it is more natural to define micropores as pores smaller than 8 Å.

6.2.4 Initial location of framework Al

The framework of mordenite can be constructed using only 5-1 secondary building units, forming 4, 5, 8 and 12-membered rings [1]. Each unit cell $T_{48}O_{96}$ contains four distinctly different tetrahedral sites T_1, T_2, T_3 and T_4 and ten distinct oxygen sites $O_1, \ldots O_{10}$. The four-membered rings (four per unit cell) each contain two T_3 and two T_4 sites. The T_3 and T_4 sites are located near the side pockets, while the T_1 and T_2 sites can be found in the main channel. For a more detailed description of the structure and symmetry of mordenite, we refer the reader to Refs. [1, 126]. The early study of Alberti *et al.* [126] showed that in HMOR, the Al content of the T sites has a ratio of $T_1 : T_2 : T_3 : T_4 = 18 : 10 : 43 : 29$ for a wide range of the Si/Al ratio. Furthermore, the Brønsted acid sites are preferentially located at O_2, O_7 and O_9. As each unit cell of MOR contains 16 T_1 atoms, 16 T_2 atoms, 8 T_3 atoms and 8 T_4 atoms, the total number of Al atoms present at each T site scales as $T_1 : T_2 : T_3 : T_4 = 36 : 20 : 43 : 29$. This result agrees well with quantum mechanical calculations [284–287] that show the preferential occupancy of Al at the four-membered rings of MOR. This is also in agreement with results of molecular simulations [129, 130].

In this work, we constructed a supercell consisting of $28 \times 25 \times 68$ unit cells, i.e. $a = 506.6$ Å, $b = 512.9$ Å and $c = 511.6$ Å, starting from an all-silica mordenite. In the model, the Al-O bond length is considered equal to the Si-O bond length. For a given Si/Al ratio, a Monte Carlo (MC) scheme is used to distribute the Al atoms over the framework, using the relative Al occupancy at each T site derived by Alberti *et al.* [126]. Initially, the T sites for Al are randomly selected, in such a way that two Al atoms are separated by at least one Si atom in order to obey the Löwenstein rule. Based on electrostatic arguments, Dempsey *et al.* [288] proposed that the number of Al-O-Si-O-Al linkages has to be minimized for a given Si/Al ratio. However, Schröder *et al.* [289] and Limtrakul *et al.* [290, 291] showed that Dempsey's rule does not hold for zeolites with multiple four-membered rings, which is supported by the experiments of Takaishi *et al.* [292]. In this paper, we propose that Dempsey's rule applies to all Al except for Al in four-membered rings i.e. T_3 and T_4 sites.

The distribution of Al in the framework is simulated using a Monte Carlo (MC) simulation. We considered the interaction of a next-nearest-neighboring Al pair in the Al-O-Si-O-Al linkage. The energy of this pair is given by E_{ij} (in units of k_BT), where i and j are the indexes of the T sites of Al ($i, j = 1, \ldots 4$, note that $E_{ij} = E_{ji}$). Here, E_{34} is set to a negative value as the Al-O-Si-O-Al linkage is favored at the T_3 and T_4 sites of four-membered rings. The other E_{ij} are set to large positive values as according to Dempsey's rule the Al-O-Si-O-Al linkage should be avoided at other T sites. In each MC step, an attempt is made to exchange the position of a randomly selected framework

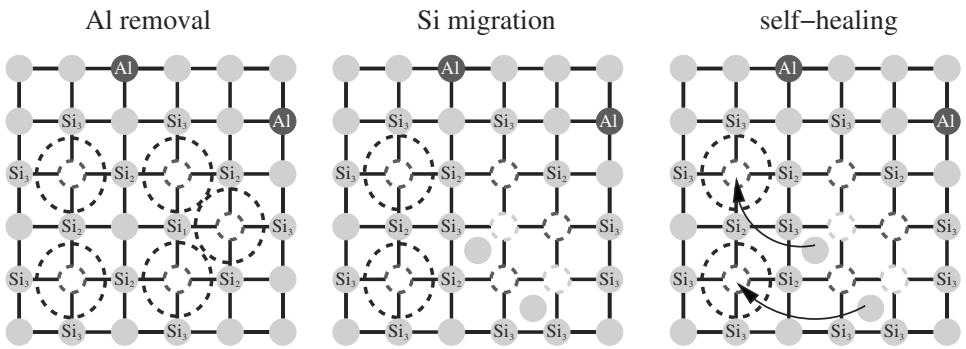

Figure 6.1: Schematic representation of the dealumination scheme used in the simulations: Al removal (Al-), Si migration (Si-) and self-healing (Si+), see section 6.2.5. Mordenite is schematically represented by an orthogonal lattice, where framework Al is denoted by dark spheres and framework Si by grey spheres. Si atoms with i next-nearest Al neighbors are denoted by Si_i. The removed Al and migrated Si atoms are drawn as dashed dark and grey circles, respectively. Silanol nests are indicated as large dashed circles. The arrows show the self-healing of silanol nests by migrated Si atoms.

Al with a framework Si atom. This move is accepted when the total energy is lowered, otherwise it is rejected. Configurations that violate Löwenstein's rule are always rejected. A typical simulation requires at least 10^4 trial moves for each Al atom.

We also created stacking fault domains in the MOR framework. Experimentally it has been shown that mordenite crystals consist of unit cells of *Cmcm* symmetry interdispersed with unit cells that are offset by half a unit cell along the z crystallographic axis [49]. Such packing defects are often referred to as the stacking faults. XRD refinements show that mordenite samples may contain up to 20% of framework atoms located in stacking faults [49]. The presence of stacking fault domains causes local fault junctures, which are sensitive to dealumination, and hence are regions where mesopores are preferentially generated [49]. Stacking fault domains are randomly distributed in the zeolite and their content may vary depending on the synthesis conditions. In our simulations, we construct stacking fault domains by randomly inserting rectangular units of $1 \times 1 \times 5$ unit cells (with a size of $18.094 \times 20.516 \times 37.620$ Å) into the large supercell. With a probability of 0.8, the stacking fault domain is inserted at a position where it is connected to a stacking fault domain that was already inserted. In this way, the size of the resulting mesopores corresponds to those observed in experiments using electron tomography [283].

6.2.5 Simulation scheme for dealumination

Inspired by the mechanism proposed by Marcilly [44], our dealumination scheme consists of the following steps (see also Fig. 6.1):

1. The removal of framework Al (denoted by Al-). Framework Al is removed and transformed into extra-framework Al (Al_{EF}, this typically consists of AlO^+, $Al(OH)^{2+}$ and $AlO(OH)$). Typically extra-framework Al is removed using a mild acid. In our simulation we only consider the rate of the step to extract Al from the framework, and we assume that all resulting Al_{EF} is effectively removed from the system in a separate step. Due to the hydrolysis of Al-(O-Si-)$_4$ bonds, the removal of one framework Al atom results in the formation of a framework vacancy consisting of four silanol (SiOH) groups, i.e. a silanol nest (here denoted by 4SiOH).

2. The migration of framework Si (denoted by Si-). Framework Si is mainly extracted from stacking fault domains. The generated Si atoms will migrate through the crystal and eventually heal the generated silanol nests, see below. The migrating Si atoms are denoted by Si_{MG}.

Rate constants for Si migration, k_{Si_i}				
	Si_4	Si_3	Si_2	Si_1
Cmcm domain	0	0	0.5	1000
Stacking fault domain	0	0	10	1000
Interface	1	1	1	1
Rate constants for Al removal, k_{Al_i}				
	Al_4	Al_3	Al_2	Al_1
Cmcm domain	1	1000	1000	1000
Stacking fault domain	1	1000	1000	1000
Rate constants for self-healing, $k_{\mathrm{Si}+}$				
Cmcm domain			2	
Stacking fault domain			0	

Table 6.1: Rate constants for Al removal, Si migration and self-healing (in units of events per unit of time, arbitrary units). The subscript *i* of a Si/Al atom refers to the number of its next-nearest Si/Al neighbors.

3. The self-healing of a silanol nest (denoted by Si+). Silanol nests can be healed by migrating Si atoms ($\mathrm{Si}_{\mathrm{MG}}$) extracted from stacking fault domains, in order to form a perfect local siliceous structure.

The Kinetic Monte Carlo (KMC) method [293] is then used to study the dynamics of the dealumination process. In this method, all possible events (possible simulation steps) are considered and it is assumed that these events are independent. For each T-atom, each of the possible steps are considered as separate events. At each time step, a certain event in the simulation is selected with a probability proportional to its rate *r*:

$$r_{\mathrm{Al}-} = k_{\mathrm{Al}_i}[\mathrm{Al}_i] \tag{6.1}$$
$$r_{\mathrm{Si}-} = k_{\mathrm{Si}_i}[\mathrm{Si}_i] \tag{6.2}$$
$$r_{\mathrm{Si}+} = k_{\mathrm{Si}+}[\mathrm{4SiOH}][\mathrm{Si}_{\mathrm{MG}}] \tag{6.3}$$

in which the brackets $[\cdots]$ denote the concentration of a certain component. For each framework Si or Al atom, the subscript *i* denotes whether it is connected to 1, 2, 3 or 4 other TO_4 units (where T can be either an Al or Si metal atom). Therefore, the number of hydroxyl group connected to T_i equals $4-i$. k_{Al_i}, k_{Si_i}, $k_{\mathrm{Si}+}$ are predetermined rate constants. Note that the Al removal and Si migration are first order reactions, while the self-healing is a second order reaction. The main source of Si_{MG} for self-healing originates from stacking fault domains, even though the roughening of the crystal surface and extraction of Si from *Cmcm* domains may also contribute a small amount [294]. As we are only interested in the final zeolite structure after many KMC steps, arbitrary units for the reaction rates will be used.

In principle, quantum-mechanical calculations could be used to extract the activation energy and therefore rate constants for the steps given in Eqs. 6.1, 6.2, 6.3. Due to the complexity and heterogeneity of the zeolite framework, this approach is extremely difficult to implement. In our simulations, based on our understanding of the experimental system we have guessed values for these constants as follows: *(1)* the rate constant of k_{Al_4} is set to 1 (arbitrary units) in the *Cmcm* and stacking fault domain. During dealumination, framework Al is considered to be equally active in both regions. The value of this rate constant is used as a reference for the others; *(2)* the rate constants are set to a value of 1000 for the following reactants: Al_1, Al_2, Al_3, and Si_1, both in the *Cmcm* and stacking fault domains. T atoms connected more than one hydroxyl group are considered less stable during dealumination. As shown by NMR studies, these components hardly exist [46, 295–298]; *(3)* rate constants are set to 0 for inert compounds like Si_3 and Si_4. This is reasonable unless hydrofluoric acid is used for dealumination; *(4)* the rate constant k_{Si_2} in the *Cmcm* region is set to 0.5. This value is between the values for k_{Si_3} and k_{Al_4}. Si_2 is the main component that affects the change of the porosity of the framework. For instance, when $k_{\mathrm{Si}_2} = 0$, silanol nests will be completely healed by $\mathrm{Si}_{\mathrm{MG}}$, resulting in a defect-free framework. For the stacking fault

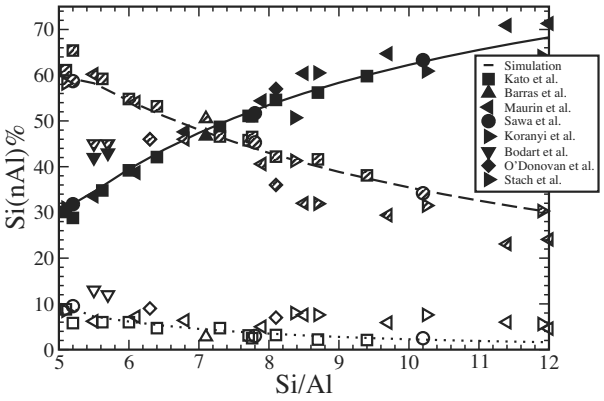

Figure 6.2: Simulated Si(nAl) distribution of parent HMOR (prior to dealumination). For the ^{29}Si NMR experiments: filled symbols, Si(0Al); semi-open symbols, Si(1Al); open symbols, Si(2Al). For our simulations: solid line, Si(0Al); dash line, Si(1Al); dotted line, Si(2Al). The experimental data is taken from Kato *et al*. [299], Barras *et al*. [300], Maurin *et al*. [301], Sawa *et al*. [295], Koranyi *et al*. [302], Bodart *et al*. [296], O'Donovan *et al*. [46] and Stach *et al*. [298].

domains, the value of k_{Si_2} is set to a large value (10); *(5)* As the boundaries between stacking fault domains and *Cmcm* domains are easily destructed, we assume that at these interfaces all Si is as reactive as Al_4 (rate constant of 1); *(6)* Self-healing of silanol nests is considered to take place equally frequent for all silanol nests, except inside the stacking fault domains where self-healing does not take place as we assume that the Si atoms in these domains will be used for self-healing of the *Cmcm* part of the structure. An overview of all kinetic constants is given in table 6.1. In our simulations, we assumed that the total fraction of stacking fault domains equals $r_{\text{meso}} = 0.13$ as this results in a similar mesoporosity as in electron tomography experiments. In addition, the value of r_{meso} matches the number of Si atoms needed in the self-healing step in the *Cmcm* domains. In this way, nearly all Si_{MG} will be used to heal silanol nests. A typical simulation is started from a large supercell with predefined stacking fault domains. A list of all possible events is constructed, and one of these events is selected with a probability proportional to its rate. After the execution of this event, the list of possible events is updated and the procedure is repeated until the desired Si/Al ratio is reached.

6.3 Results and discussion

6.3.1 Al distribution

In Fig. 6.2, the Si-Al connectivity as a function of the Si/Al ratio is shown for parent HMOR based on the scheme described in section 2.4. Si(nAl) denotes a framework Si atom which is connected via oxygen atoms to n Al atoms ($1 \leq n \leq 4$). In general, for increasing Si/Al ratios the fraction of Si(1Al) and Si(2Al) decreases while the fraction of Si(0Al) increases. The computed fractions of Si(nAl) are in good agreement with available ^{29}Si NMR experiments [46, 295, 296, 298–302]. The used values for E_{ij} result in a preferential occupation of framework Al at T_3 and T_4 sites [129], while Al-O-Si-O-Al linkages are unfavorable at the other T sites, following Dempsey's rule. Completely ignoring Dempsey's rule (i.e. $E_{ij}/k_BT = 0$ for each i,j) results in the following distribution: 42% Si(0Al), 42% Si(1Al) and 16% Si(2Al) for MOR with Si/Al=5, clearly in disagreement with the experimental data in Fig. 6.2. Setting $E_{ij}/k_BT = 10$ for all i, j exactly corresponds to Dempsey's rule. As expected, the resulting fractions of Si(nAl) clearly disagree with the experimental ones (see Fig. 6.3). In particular, the fraction of Al pairs in the four-membered rings approaches zero for Si/Al ratios larger than 6 (Fig. 6.3(b)), in disagreement with the pref-

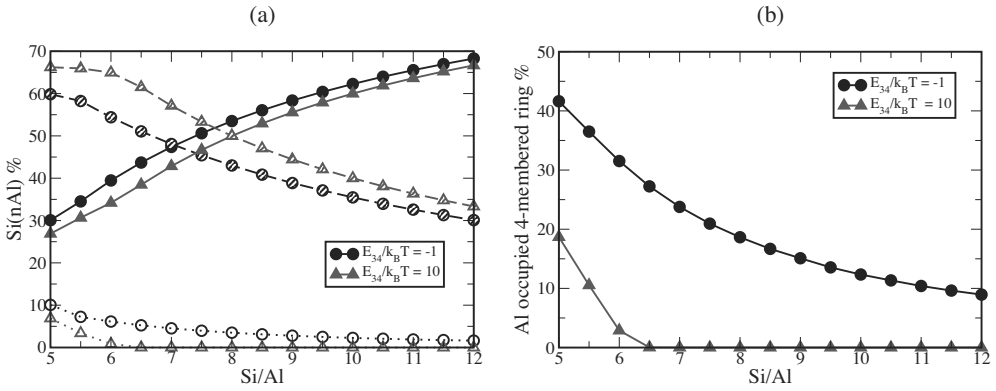

Figure 6.3: (a) Simulated Si(nAl) distribution of parent HMOR as a function of the Si/Al ratio for two different values of E_{34}. Solid line, Si(0Al); dashed line, Si(1Al); dotted line, Si(2Al). (b) The fraction of four-membered rings occupied by Al pairs for $E_{34}/k_BT = -1$ and 10, respectively. A single unit cell of MOR contains four four-membered rings, and each four-membered ring contains two T_3 and two T_4 sites.

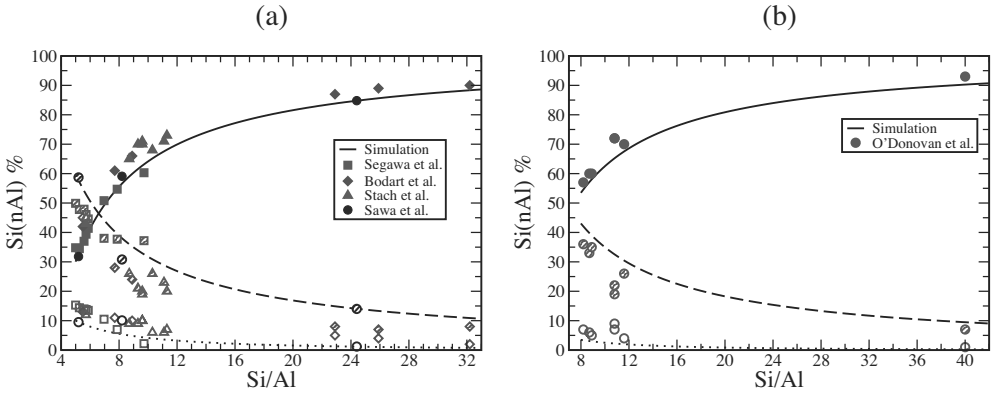

Figure 6.4: Simulated Si(nAl) distributions during dealumination of (a) parent HMOR with Si/Al= 5 and (b) parent HMOR with Si/Al= 8. Experiments: solid symbols, Si(0Al); semi-open symbols, Si(1Al); open symbols, Si(2Al). Simulations: solid line, Si(0Al); dashed line, Si(1Al); dotted line, Si(2Al). The experimental data is taken from Sawa *et al.* [295], Bodart *et al.* [296], O'Donovan *et al.* [46], Segawa *et al.* [297] and Stach *et al.* [298].

erential locations of Al widely reported in literature [129, 284–287]. Therefore, we conclude that Dempsey's rule is valid for all the building units of MOR except for the four-membered ring. We speculate that these findings are also applicable to the other aluminosilicate zeolites with similar secondary building units.

Fig. 6.4 shows the computed fractions of Si(nAl) of dealuminated HMOR based on the dealumination scheme described in section 6.2.5. The parent HMOR samples have Si/Al ratios of 5 and 8 and are generated using the procedure of section 6.2.5. Similar trends of the fractions of Si(nAl) as a function of the Si/Al ratio can be observed as for parent HMOR (Fig. 6.2). Our simulations are in very good agreement with various ^{29}Si NMR experiments from literature, even though the computed fractions of Si(0Al) and Si(2Al) are slightly lower than the corresponding experimental values, and the computed fraction of Si(1Al) is somewhat larger. We found this is a general trend independent of the precise values of the model parameters of our dealumination scheme. These minor discrepancies can be attributed to the approximations made in the experiments. In ^{29}Si NMR measurements, it is often assumed that the only silanol present in the zeolite framework is SiOH (attributed to peak at -105 ppm) so that the peak at -99 ppm is only caused by Si(2Al) rather

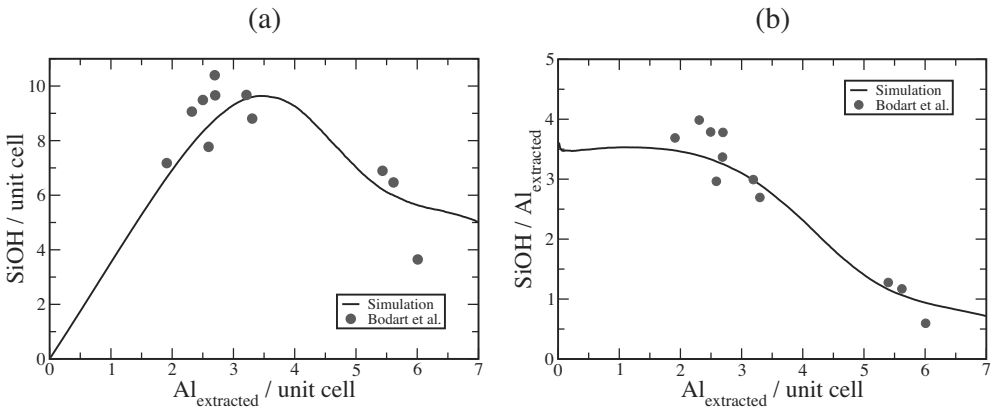

Figure 6.5: Computed SiOH concentration during dealumination of parent HMOR with Si/Al= 5.5 compared to the experiments by Bodart *et al*. [296]. A ratio of Si/Al=50 corresponds to ≈ 6 extracted Al atoms per unit cell.

than $Si(OH)_2$ [296]. However, the Si-Al connectivity of parent HMOR (Fig. 6.2) shows that approximately 10% of the framework Si is present as Si(2Al). During dealumination, Si(2Al) will be quickly transferred into $Si(OH)_2$ resulting in a contribution to the NMR signal at -99 ppm. It is straightforward to show that neglecting the contribution of $Si(OH)_2$ to the NMR signal at -99 ppm will result in an overestimation of the fraction of Si(2Al) and an underestimation of the fraction of Si(1Al) in HMOR.

The concentrations of silanol groups in dealuminated HMOR are shown in Fig. 6.5. Starting from parent HMOR with Si/Al=5.5, dealuminated HMOR shows a maximum silanol concentration at around three extracted Al atoms per unit cell, in agreement with the available experiments. The change in the number of silanol groups during dealumination indicates that the dealumination process consists of three stages. During the first stage, two dominating reactions take place simultaneously: the removal of framework Al, and the migration of Si at the interface between the stacking fault and *Cmcm* domains. As four SiOH are generated by extracting a single Al atom, the initial slope of Fig. 6.5 (a) should be close to four. A close inspection of our simulation results reveals that this slope is approximately 3.5 SiOH per extracted Al per unit cell. The reason for this difference is that only SiOH is taken into account here. When the number of extracted Al atoms per unit cell reaches around three, the fraction of SiOH rapidly levels off at about ten SiOH per unit cell. Further dealumination results in a decrease of the number of silanol groups. This phenomenon is caused by the self-healing of silanol nests by migrating Si atoms. It is often observed experimentally that dealumination is accompanied by the formation of internal mesopores as well as the roughening of the zeolite external surface [294]. The extracted Si from the stacking fault domains will be used in the self-healing process. The rate constant of self-healing has a larger value than that of Al removal (table 6.1). According to Eq. 6.3, the self-healing rate is increased significantly when enough migrated Si is extracted from the stacking fault domains. In the final stage, nearly all framework Al is extracted and the concentration of SiOH levels off at around five SiOH per unit cell. Our simulation shows a good agreement with the experimental data of Bodart *et al*. [296].

6.3.2 Changes in morphology and crystallinity

Fig. 6.6 shows SEM images of parent and dealuminated mordenite. The images clearly show that particles of a few μm are present, consisting of aggregates of crystallites with typical dimensions of around 200 nm. The dealumination process hardly affects the morphology of the particles, although after dealumination the particles appear to be slightly more open with less densely packed crystallites.

Fig. 6.7 shows the experimental XRD patterns as well as those derived from the simulations, both for parent and dealuminated samples. The parent material was assumed to have a crystallinity of 100%, calculated from the sum of intensities of the peaks defined in section 6.2.2. Upon dealumination the intensity of the peaks at high diffraction angles decreased both in experiments and simulations. This indicates that the framework is partially dissolved upon dealumination. Note that in experiments the increase in intensities of the peaks at low diffraction angles after dealumination is related to the enhanced hydrophobicity due to the loss of acid sites. This effect is not visible in the simulated spectra, as water was not considered in our simulations. The simulated crystallinity as a function of the degree of dealumination is shown in Fig. 6.8. It is clear that even after heavy dealumination, still 70% crystallinity is retained. Experimentally a crystallinity of 89% was found for A50 sample. This qualitatively agrees with literature reports on the crystallinity of dealuminated MOR and zeolite Y [46, 303, 304]. In conclusion, the crystallinity and morphology of mordenite crystals are largely preserved upon dealumination, supported by good agreement between experimental and simulation results.

6.3.3 Impact of dealumination on the porosity

The porosity of mordenite before and after dealumination was experimentally analyzed using N_2 and Ar physisorption isotherms, see Fig. 6.9. The N_2 isotherms show a significant uptake at relative pressures below 0.05 due to micropore filling, and a modest hysteresis loop at relative pressures higher than 0.4 indicative of the presence of mesopores. The forced closure of the desorption branch of the isotherm around $p/p_0 = 0.4$ indicates that the mesopores can be assessed via openings smaller than about 4 nm. The experimental isotherms suggest a clear increase in both micro- and mesopore volume upon dealumination. In addition, the external surface area is enlarged, which can be attributed to the enlarged mesoporosity and surface roughness during the acid

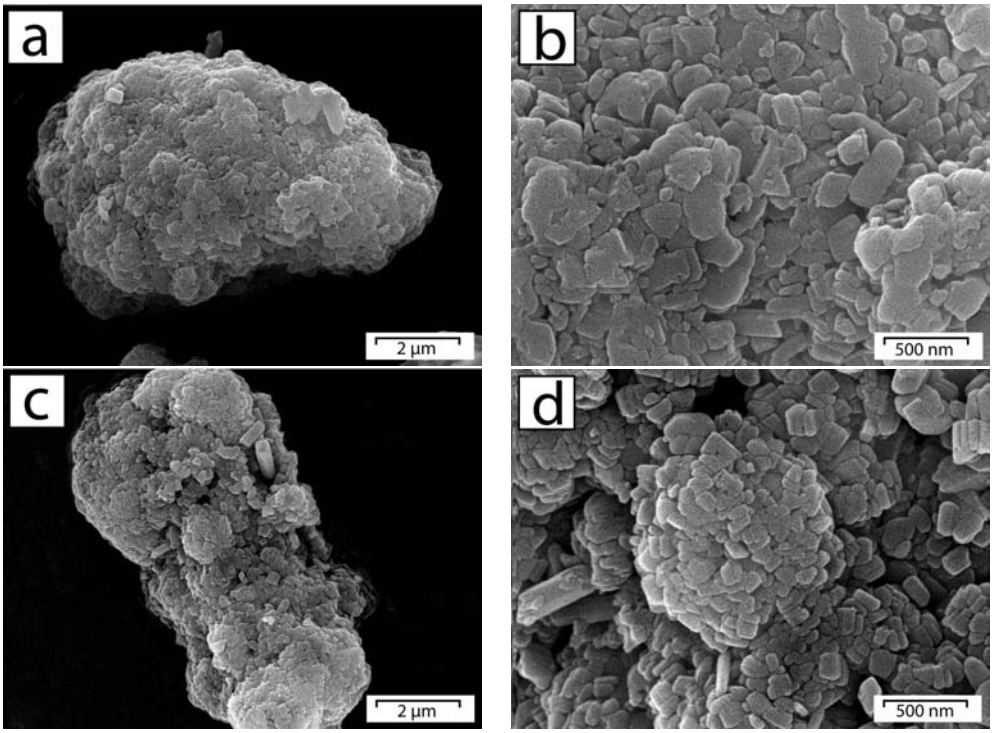

Figure 6.6: SEM images of (a,b) A6 and (c,d) A50 HMOR samples.

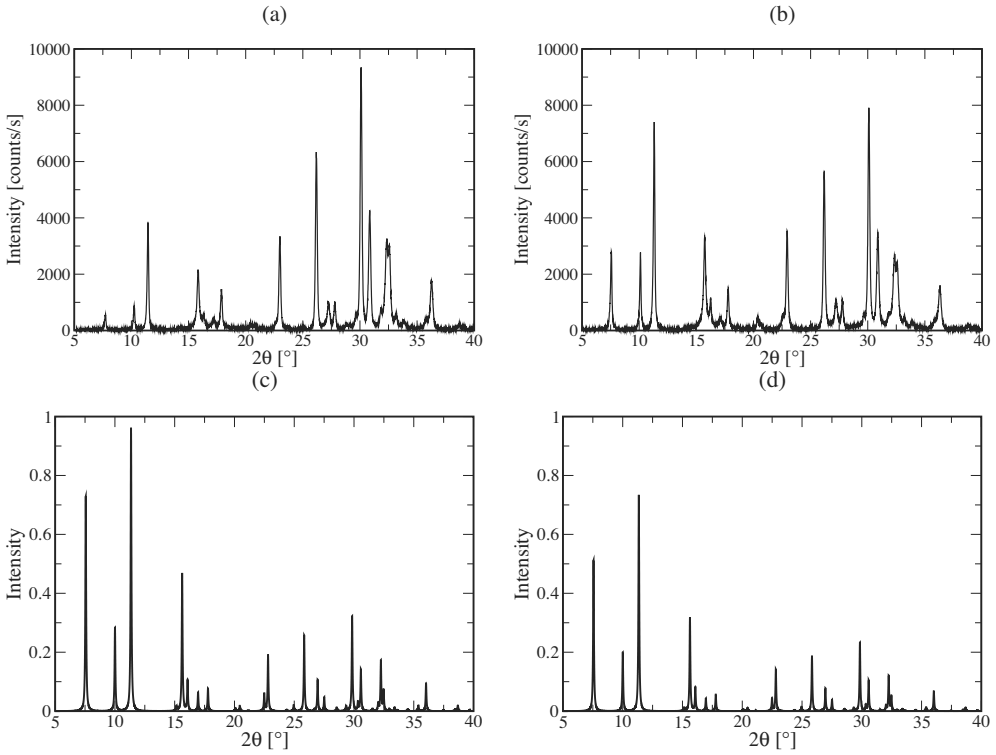

Figure 6.7: Experimental CoK$_\alpha$ XRD patterns of (a) A6 and (b) A50 HMOR samples. The A50 HMOR has a 89% crystallinity, assuming 100% crystallinity for A6 HMOR. Computed CoK$_\alpha$ XRD powder pattern of (c) parent HMOR with Si/Al= 6.0 and (d) dealuminated HMOR with Si/Al= 50 starting from parent HMOR with Si/Al= 6.0. The latter system has a crystallinity of 72%. The simulated MOR supercell consists of $28 \times 25 \times 68$ unit cells. It is assumed that water is not present. Note that the same scale of the XRD intensities is used for either experiments (a,b) or simulations (c,d).

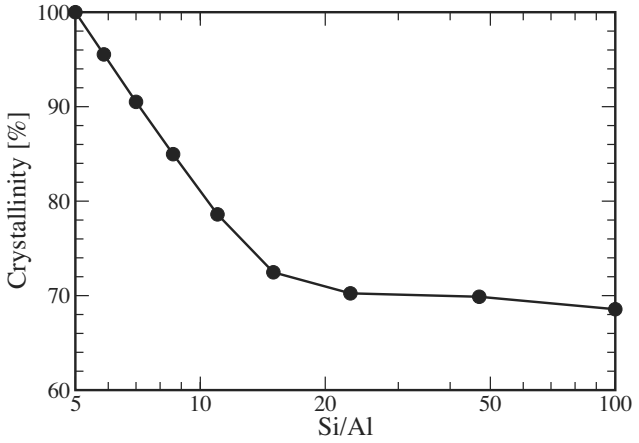

Figure 6.8: Computed zeolite crystallinity during dealumination of parent HMOR with Si/Al= 5.5.

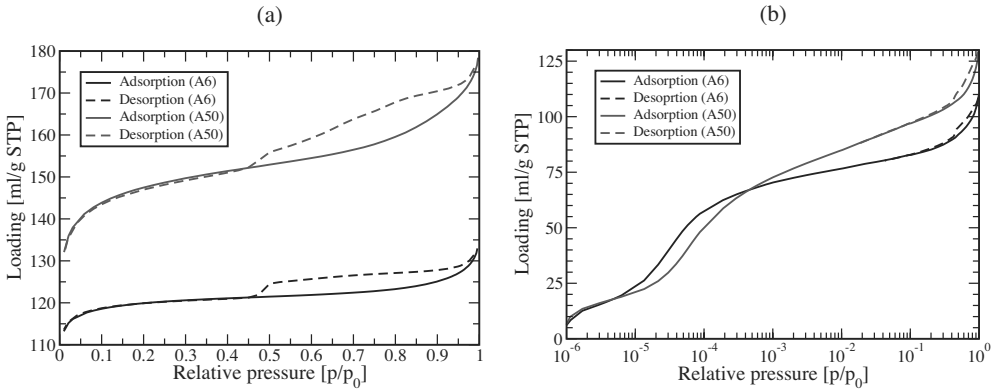

Figure 6.9: Physisorption isotherms of (a) N_2 and (b) Ar for A6 and A50 HMOR samples.

treatment (as was also suggested from the SEM images, Fig. 6.6). Similar results were derived from the Ar physisorption isotherms at high relative pressures. The Ar adsorption isotherms at low pressures give more detailed information on the change of microporosity upon dealumination. In the relative pressure range of $10^{-5} \sim 10^{-4}$, the Ar loading in A6 is higher than for A50, while the opposite is true starting from a relative pressure of 10^{-3}. The enlargement of the micropores upon dealumination weakens the adsorption strength, resulting in a low Ar loading at low pressures. This is a typical example for which classical methods of micropore size analysis are not suitable, and it is imperative to use NLDFT to interpret the experimental results. These micropore results of the NLDFT analysis will be compared in detail with simulations.

The simulated pore size distribution of parent mordenite is shown in Fig. 6.10 (a). Three major peaks are observed at pore diameters of 6.7 Å, 5.1 Å and 3.8 Å, corresponding to the main channels, the side pockets and the inaccessible eight-membered channels, respectively. The simulated pore sizes are in excellent agreement with the values reported by the Atlas of Zeolite Framework Types [1]. The various pores in parent mordenite are illustrated in Fig. 6.10 (b). The computed micropore volume of 0.21 ml/g for micropores of $4.5 \sim 8$ Å is in good agreement with experimental results considering a $0.01 \sim 0.02$ ml/g error in the experimentally obtained micropore volume

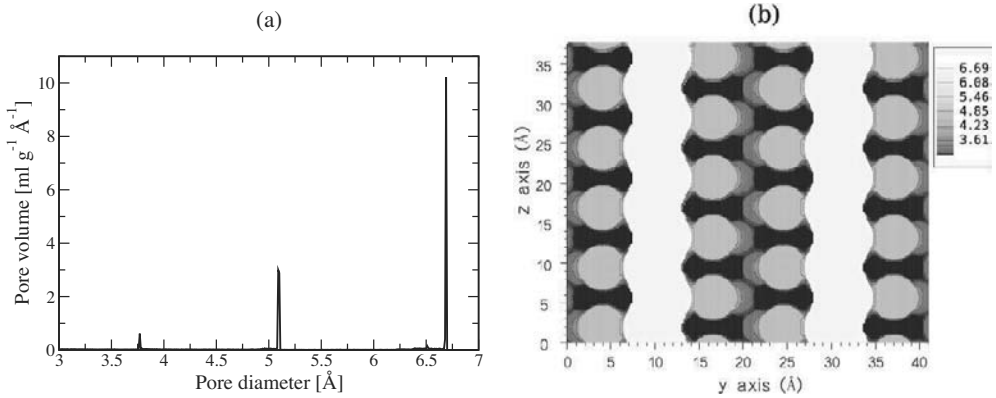

Figure 6.10: (a) Computed micropore size distribution of parent HMOR Si/Al=6. (b) Slice through the y-z plane at $x = a/2$, showing the location of the main channels and the side pockets. In this figure, two main channels are indicated as a white channel in the z direction, while the side pockets are shown as spherical regions separated by the dark four-membered rings. The color coding shows the pore diameter in Å. Only pores larger than 3 Å are shown.

		A6			A50		
		Ar	N_2	sim.	Ar	N_2	sim.
Pore volume [ml/g]	Ultramicropore	0.15	-	0.21	0.16	-	0.21
	Supermicropore	0.00	-	0	0.01	-	0.047
	Micropore volume	0.15	0.17	0.21	0.17	0.20	0.257
	Mesopore	0.03	0.02	0	0.04	0.05	0.04
Surface area [m^2/g]	Ultramicropore	1160	-	-	1200	-	-
	Supermicropore	0	-	-	43	-	-
	Mesopore	16	26	-	20	74	-
	Surface area	1176	-	-	1263	-	-
Pore diameter [Å]	Side pocket	4.62	-	5.1	4.62	-	5.0
	Main channel	5.52	-	6.7	5.82	-	6.6
	Secondary pore	-	-	0	-	-	7.1

Table 6.2: Porosity of A6 and A50 HMOR samples analyzed by the NLDFT method based on high-resolution Ar physisorption isotherms (denoted by Ar), N_2 Physisorption (denoted by N_2) and simulations (denoted by sim.). In this table, we used the following definitions: ultramicropores are defined as pores smaller than 8 Å, supermicropores are defined as pores of 8 $\sim$ 20 Å, mesopores are defined as pores larger than 20 Å, and micropores are defined as pores smaller than 20 Å.

(see table 6.2). Furthermore, we may expect small differences because of the definition of pore volume in the simulations (section 6.2.3). After dealumination, the total micropore volume of dealuminated HMOR with Si/Al= 50 is 0.21 ml/g for micropores smaller than 8 Å, identical to that of parent mordenite. This is slightly larger than the experimentally measured micropore volumes (0.20 ml/g measured by N_2 and 0.16 ml/g by Ar physisorption). For dealuminated mordenite, the simulated total pore volume is 0.297 ml/g. The sum of the mesopore volume and supermicropore volume equals 0.087 ml/g. This is slightly larger than the corresponding values obtained from N_2 and Ar physisorption (both 0.05 ml/g).

Fig. 6.11 shows the influence of dealumination on the micropore size distribution for both the simulations and the analysis of Ar adsorption isotherms. As the experiments result in data with a much lower resolution than in the simulations, the simulation results were binned to a resolution of 0.3 Å to allow a direct comparison. In the parent sample, the micropores in the side pockets and main channels of HMOR are identified as pores of 4.6 Å and 5.5 Å by the NLDFT method, and

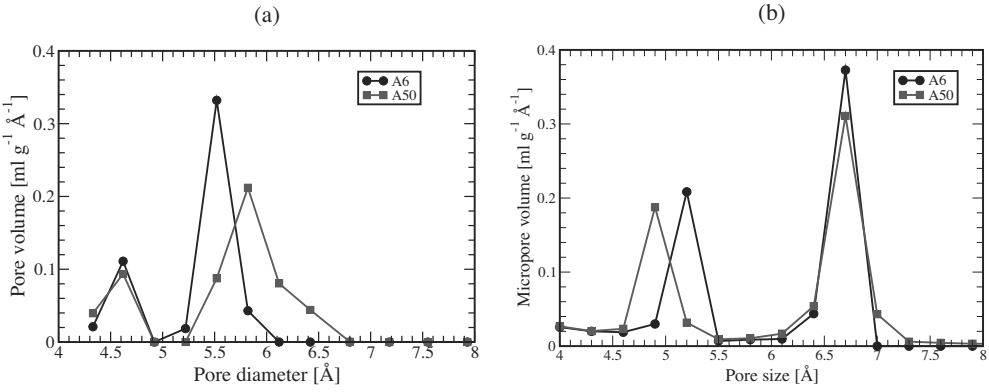

Figure 6.11: Comparison between (a) the micropore size distribution obtained from Ar physisorption and (b) simulated micropore size distribution for parent HMOR A6 and dealuminated HMOR A50. The parent HMOR A6 has a Si/Al ratio 6, while dealuminated HMOR A50 has a Si/Al ratio 50. The simulated results are obtained by binning the micropore size distribution of Fig. 6.12 (a).

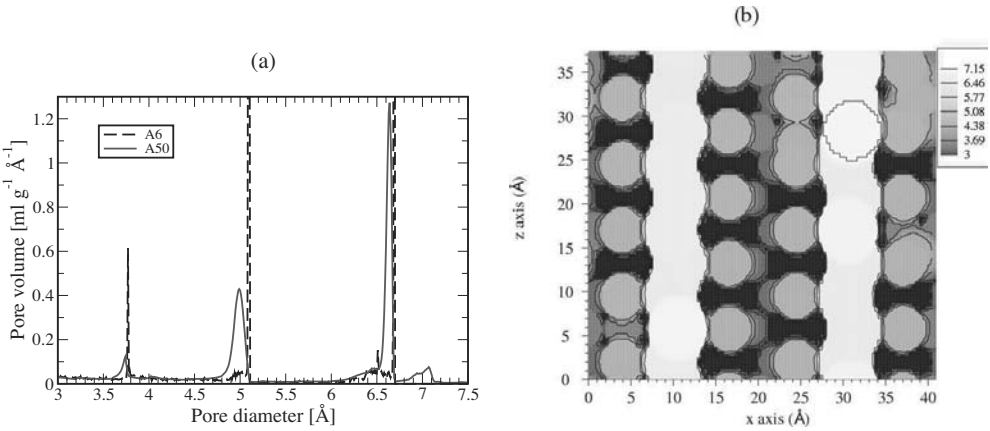

Figure 6.12: (a) Simulated micropore size distribution of dealuminated HMOR with Si/Al= 50. (b) Slice through the y-z plane at $x = a/2$, showing the location of the main channels and the side pockets. The micropore size distribution of parent HMOR is taken from Figure 6.10 (a) and the peaks are not complete shown in this figure. The color coding shows the pore diameter in Å. Only pores larger than 3 Å are shown.

as pores of 5.2 Å and 6.7 Å by simulations. Ar physisorption underestimates pore sizes, which is inherent to probing small pores using Ar atoms with a comparable size. During dealumination, the pore sizes are hardly changed (also see table 6.2). It is important to note that for both approaches, after dealumination broad peaks can be observed at the pore diameters larger than the main channel of parent mordenite. This indicates a transformation of the main channels upon dealumination. It is clear that much information is lost by the 0.3 Å resolution. However, the direct comparison between simulated and experimental data confirms the validity of our simulation model.

Fig. 6.12 (a) illustrates the importance of our simulations, as information on the micropore size distribution can be obtained with a much higher resolution and detail than is available from experiments. Several conclusions concerning the effect of the dealumination can be drawn:

1. The peak at a pore size of 3.8 Å which is associated with the modulating eight-membered channel slightly broadens, and the total pore volume associated with this peak does not change significantly;

2. The peak related to a pore size of 5.1 Å, which is associated with the side pockets, also broadens and its maximum shifts to slightly smaller pore sizes. This is typically caused by the roughing of the side pockets during dealumination. At the same time the total pore volume related to these side pockets significantly decreases (with 0.006 ml/g). This indicates that indeed part of the side pockets is affected by the dealumination process.

3. The peak at 6.7 Å, which is associated with the main channel, also broadens and shifts to slightly smaller pore sizes. More importantly, also here a significant loss in the total pore volume is observed (of 0.013 ml/g). This loss of the pore volume is attributed to the destruction of well-defined main channels by dealumination.

4. After dealumination there is an additional broad peak around pore diameters of $7 \sim 7.5$ Å. The occurrence of this peak corresponds to newly created pores, significantly larger than the main channels, which has been reported in several experiments [55, 271]. The volume of these secondary pores (of 0.016 ml/g) compensates largely for the loss of pore volume associated with the side pockets (of 0.006 ml/g) and main channel (of 0.013 ml/g) upon dealumination. This means that the total micropore volume does not change much upon dealumination.

Concluding, during dealumination, two distinct areas of mordenite are predominantly dissolved: the Al-rich four-membered rings and the internal surfaces of the main channels. This leads to parts of the main channel merging with damaged side pockets nearby (see Fig. 6.12 (b)). Hence part of the pore volume associated with well-defined main channels and side pockets is lost, but secondary pores are formed instead during dealumination. Although in much less detail, these results are validated by the analysis of the Ar physisorption (Fig. 6.11 (a)) which shows pores in the range of $6.1 \sim 6.8$ Å appearing. We therefore confirm that dealumination of HMOR brings about the formation of the secondary pores in evidence of both simulations and the NLDFT analysis.

6.4 Conclusions

In this work, we have combined experiments with simulations to achieve a detailed understanding of the effect of dealumination on the pore system of HMOR.

A simulation method is developed to model the distribution of the framework Al in parent HMOR. In agreement with NMR experiments, we can conclude that *(1)* beside the Löwenstein's rule, the Al content in the four T sites is given by Alberti *et al*. [126]; *(2)* Dempsey's rule is valid for all building units of MOR except for the four-membered rings. This leads to the conclusion that the presence of Al stabilizes four-membered rings. This is expected to be valid for other zeolites containing similar building units. For instance, DDR-type zeolites contain no four-membered rings, and thus an all-silica structure can easily be obtained.

In our simulations, dealumination is considered as a multiple-step process consisting of the removal of framework Al and the self-healing of the SiOH nests by migrated Si atoms. The computed Si-Al connectivities agree well with ^{29}Si NMR experiments from literature for both parent and dealuminated HMOR. The SiOH concentration of HMOR during dealumination reveals that the dealumination procedure contains three stages: *(1)* the removal of framework Al takes place in the *Cmcm* and stacking fault domains simultaneously. In particular, the extraction of the framework Al generates SiOH nests, and migrating Si atoms are created by the removal of the framework Si from the interfaces between the *Cmcm* and stacking fault domains. *(2)* Once enough SiOH nests and migrating Si atoms are present, the self-healing reaction occurs rapidly to transform some SiOH nests into a silicious structure. *(3)* The final structure of dealuminated HMOR shows modified micropores and newly created mesopores. All migrating Si atoms are used in the self-healing process. This dealumination mechanism is expected to be applicable to other aluminosilicate zeolites. For example, during dealumination, the Al-rich LTA-type zeolite will be completely dissolved, while MFI-type zeolite may still maintain the well-defined micropores apart from the formation of mesopores. We speculate that this is because of the presence of four-membered rings in LTA-type zeolite, while these rings are absent in MFI-type zeolite.

Ar physisorption experiments are combined with simulation techniques to investigate the microporosity of MOR at the molecular level. For dealuminated MOR, both approaches indicate the formation of the secondary pores (larger than the main channel) in the dealuminated HMOR. The mechanism of this transformation follows from the observation that during dealumination, two distinct areas of the MOR framework are mainly dissolved: the Al-rich four-membered rings and the internal surfaces of the main channels. This results in merging of the main channels with damaged side pockets nearby, forming large secondary pores during dealumination. Such an enlargement of micropores may have a considerable effect on the catalytic performance of MOR.

References

[1] Baerlocher, C.; McCusker, L.B.; Olson, D.H., *Atlas of Zeolite Framework Types*, 6th ed. Elsevier; Amsterdam, 2007.

[2] Huang, H.J.; Ramaswamy, S.; Tschirner, U.W.; Ramarao, B.V. *Sep. Purif. Techno.* **2008**, *62*, 1–21.

[3] Bejblova, M.; Zilkova, N.; Cejka, J. *Res. Chem. Intermediat.* **2008**, *34*, 439–454.

[4] Mravec, D.; Hudec, J.; Janotka, I. *Chem. Pap.-Chem. Zvesti* **2005**, *59*, 62–69.

[5] Bellussi, G.; Pollesel, P. *Stud. Surf. Sci. Catal.* **2005**, *158*, 1201–1212.

[6] Kerby, M.C.; Degnan, T.F.; Marler, D.O.; Beck, J.S. *Catal. Today* **2005**, *104*, 55–63.

[7] Degnan, T.F. *J. Catal.* **2003**, *216*, 32–46.

[8] Hagen, A.; Roessner, F. *Catal. Rev.* **2000**, *42*, 403–437.

[9] Naber, J.E.; de Jong, K.P.; Stork, W.H.J.; Kuipers, H.P.C.E.; Post, M.F.M. *Stud. Surf. Sci. Cat.* **1994**, *84*, 2197–2219.

[10] Lunsford, J.H. *Catal. Rev.* **1975**, *12*, 137–162.

[11] Habib, S.; Launay, F.; Laforge, S.; Comparot, J.D.; Faust, A.C.; Millot, Y.; Onfroy, T.; Montouillout, V.; Magnoux, P.; Paillaud, J.L.; Gedeon, A. *Appl. Catal. A-Gen.* **2008**, *344*, 61–69.

[12] Xu, B.; Bordiga, S.; Prins, R.; van Bokhoven, J.A. *Appl. Catal. A-Gen.* **2007**, *333*, 245–253.

[13] Suzuki, K.; Noda, T.; Katada, N.; Niwa, M. *J. Catal.* **2007**, *250*, 151–160.

[14] Eswaramoorthi, I.; Bhavani, A.G.; Lingappan, N. *Appl. Catal. A-Gen.* **2003**, *253*, 469–486.

[15] Ichihashi, H.; Sato, H. *Appl. Catal. A-Gen.* **2001**, *221*, 359–366.

[16] Traa, Y.; Burger, B.; Weitkamp, J. *Micropor. Mesopor. Mater.* **1999**, *30*, 3–41.

[17] Smit, B.; Maesen, T.L.M. *Chem. Rev.* **2008**, *108*, 4125–4184.

[18] Lee, G.S.; Maj, J.J.; Rocke, S.C.; Garcés, J.M. *Catalysis Letters* **1989**, *2*, 243–248.

[19] Smit, B.; Maesen, T.L.M. *Nature* **2008**, *451*, 671–678.

[20] Zhu, W.; Kapteijn, F.; Moulijn, J.A.; den Exter, M.C.; Jansen, J.C. *Langmuir* **2000**, *16*, 3322–3329.

[21] Babarao, R.; Hu, Z.Q.; Jiang, J.W.; Chempath, S.; Sandler, S.I. *Langmuir* **2007**, *23*, 659–666.

[22] Funke, H.H.; Argo, A.M.; Falconer, J.L.; Noble, R.D. *Ind. Eng. Chem. Res.* **1997**, *36*, 137–143.

[23] Huddersman, K.; Klimczyk, M. *A.I.Ch.E.J.* **1996**, *42*, 405–408.

[24] Kapteijn, F.; Bakker, W.J.W.; Zheng, G.; Poppe, J.; Moulijn, J.A. *Chem. Eng. J.* **1995**, *57*, 143–153.

[25] Barrer, R.M. *J. Chem. Soc. Faraday Trans.* **1990**, *86*, 1123–1130.

[26] Ahunbay, M.G.; Elliott, J.R.; Talu, O. *J. Phys. Chem. B* **2002**, *106*, 5163–5168.

[27] Bakker, W.J.W.; van den Broeke, L.J.P.; Kapteijn, F.; Moulijn, J.A. *A.I.Ch.E.J.* **1997**, *43*, 2203–2214.

[28] R.K. Duck and J. Y. Hie, patent KR2008079793-A.

[29] Q. Liu and F. Xin and Q. Wang and Y. Dong, patent CN101269886-A.

[30] Bish, D.L.; Vaniman, D.T.; Chipera, S.J.; Carey, J.W. *Am. Mineral.* **2004**, *89*, 248–248.

[31] Kazemian, H.; Modarres, H.; Mobtaker, H.G. *J. Radioanal. Nucl. Ch.* **2003**, *258*, 551–556.

[32] de Gennaro, R.; Langella, A.; D'Amore, M.; Dondi, A.; Colella, A.; Cappelletti, P.; de Gennaro, A. *Appl. Clay Sci.* **2008**, *41*, 61–72.

[33] Bennett, C.H., in *Diffusion in Solids: Recent Developments*, edited by Nowick, A.S.; Burton, J.J. Academic Press; New York, 1975, pp. 73–113.

[34] Kärger, J.; Ruthven, D.M., *Diffusion in zeolites and other microporous solids* John Wiley & Sons; New York, 1991.

[35] Krishna, R. *Chem. Phys. Lett.* **2000**, *326*, 477–484.

[36] Nivarthi, S.; McCormick, A.V.; Davis, H.T. *Chem. Phys. Lett.* **1994**, *229*, 297–301.

[37] Post, M.F.M., in *Introduction to Zeolite Science and Practice*, Vol. 58 of *Studies in Surface Science and Catalysis*, edited by van Bekkum, H.; Flaningen, E.M.; Jansen, J.C. Elsevier; Amsterdam, 1991.

[38] van Donk, S.; Broersma, A.; Gijzeman, O.L.J.; van Bokhoven, J.A.; Bitter, J.H.; de Jong, K.P. *J. Catal.* **2001**, *204*, 272–280.

[39] Clark, L.A., Confinement and pore shape effects on adsorption, diffusion and reaction in zeolites Ph.D. thesis, Northwestern University, Evanston, IL, USA, 2000.

[40] Swabb, E.A.; Gates, B.C. *Ind. Eng. Chem. Fundamen.* **1972**, *11*, 540–545.

[41] Rajagopalan, K.; Petersa, A.W.; Edwardsa, G.C. *Appl. Catal.* **1986**, *23*, 69–80.

[42] Voogd, P.; van Bekkum, H. *Appl. Catal.* **1990**, *59*, 311–331.

[43] Bellussi, G.; Pazzuconi, G.; Perego, C.; Girotti, G.; Terzoni, G. *J. Catal.* **1995**, *157*, 227.

[44] Marcilly, C.R. *Petrole et Techniques* **1986**, *328*, 12–18.

[45] van Donk, S.; Janssen, A.H.; Bitter, J.H.; de Jong, K.P. *Catalysis Reviews-Science and Engineering* **2003**, *45*, 297–319.

[46] O'Donovan, A.W.; O'Connor, C.T.; Koch, K.R. *Micropor. Matt.* **1995**, *5*, 185–202.

[47] Sato, K.; Nishimura, Y.; Shimada, H. *Catal. Lett.* **1999**, *60*, 83–87.

[48] Nagano, J.; Eguchi, T.; Asanuma, T.; Masui, H.; Nakayama, H.; Nakamura, N.; Derouane, E.G. *Micropor. Mesopor. Mater.* **1999**, *33*, 249–256.

[49] Rudolf, P.R.; Garces, J.M. *Zeolites* **1994**, *14*, 137–147.

[50] Morin, S.; Ayraulta, P.; Gnepa, N.S.; Guisne, M. *Appl. Catal. A-Gen.* **1998**, *166*, 281–292.

[51] Lynch, J.; Raatz, F.; Dufresne, P. *Zeolites* **1987**, *7*, 333–340.

[52] Meyers, B.L.; Fleisch, T.H.; Ray, G.J.; Miller, J.T.; Hall, J.B. *J. Catal.* **1988**, *110*, 82–95.

[53] Lee, G.J.; Graces, J.M.; Meima, G.R.; van der Aalst, M.J.M. *U.S. Patent* **1991**, *5,198,595*, .

[54] Meima, G.R.; van der Aalst, M.J.M.; Samson, M.S.U.; Graces, J.M.; Lee, J.G. *ERDÖL ERDGAS KOHLE* **1996**, *7*, 315.

[55] Meima, G.R. *Cattech* **1998**, *2*, 5–12.

[56] Dwyer, J. *Stud. Surf. Sci. Catal.* **1987**, *37*, 333.

[57] Karge, H.G.; Dondur, V. *J. Phys. Chem.* **1990**, *94*, 765–772.

[58] Olken, M.M.; Garces, J.M., in *Proceedings from the 9th International Zeolite Conference*, edited by von Ballmoos, R.; Higgins, J.B.; Treacy, M.M.J. Butterworth Heineman; Boston, 1992, p. 559.

[59] Ban, S.; van Laak, A.N.C.; Landers, J.; Neimark, A.V.; de Jongh, P.E.; de Jong, K.P.; Vlugt, T.J.H. **2009**, In preparation.

[60] Perego, C.; Amarilli, S.; Millini, R.; Bellussi, G.; Girotti, G.; Terzoni, G. *Micropor. Matt.* **1996**, *6*, 395.

[61] Perego, C.; Ingallina, P. *Catal. Today* **2002**, *73*, 3–22.

[62] Cejtin, H.; Edler, J.; Gottlieb, A.; Helling, R.; Li, H.; Philbin, J.; Wingreen, N.; Tang, C. *J. Chem. Phys.* **2001**, *116*, 352–359.

[63] Meima, G.R.; van der Aalst, M.J.M.; Samson, M.S.U.; Garces, J.M.; Lee, L.G. *Proc. 9th Intern. Zeolite Conf., Butterworth, Boston* **1992**, 327–334.

[64] van Donk, S.; Bus, E.; Broersma, A.; Bitter, J.H.; de Jong, K.P. *J. Catal.* **2002**, *212*, 86–93.

[65] Ivanova, I.I.; Montouillout, V.; Fernandez, C.; Marie, O.; Gilson, J.P. *Micropor. Mesopor. Mater.* **2003**, *57*, 297–308.

[66] Su, B.L.; Norberg, V. *Coll. Surf. A* **2001**, *187-188*, 311–318.

[67] Garces, J.M., in *Proc. 12th Intern. Zeolite Conf*, Material Research Society Warrendale; PA, 1998, pp. 261–313.

[68] Garces, J.; Maj, J.J.; Lee, G.J.; Rocke, S.C. *US, 4,891,448* , .

[69] Derouane, E.G.; Gabelica, Z. *J. Catal.* **1980**, *65*, 486–489.

[70] Clark, L.A.; Ye, G.T.; Snurr, R.Q. *Phys. Rev. Lett.* **2000**, *84*, 2893–2896.

[71] Sokol, A.A.; Catlow, C.R.A.; Garces, J.M.; Alex Kuperman, A. *J. Phys. Chem. B* **2002**, *106*, 6163–6177.

[72] Vlugt, T.J.H.; Schenk, M. *J. Phys. Chem. B* **2002**, *106*, 12757–12763.

[73] Ungerer, P.; Tavitian, B.; Boutin, A., *Applications of molecular simulation in the oil and gas industry* IFP publications; Paris, 2005.

[74] June, R.L.; Bell, A.T.; Theodorou, D.N. *J. Phys. Chem.* **1990**, *94*, 8232–8240.

[75] June, R.L.; Bell, A.T.; Theodorou, D.N. *J. Phys. Chem.* **1992**, *96*, 1051–1060.

[76] Leroy, F.; Rousseau, B.; Fuchs, A. H. *Phys. Chem. Chem. Phys.* **2004**, *6*, 775-783.

[77] Frenkel, D.; Smit, B., *Understanding Molecular Simulation: from Algorithms to Applications*, 2nd ed. Academic Press; San Diego, 2002.

[78] Smit, B.; Siepmann, J.I. *Science* **1994**, *264*, 1118–1120.

[79] Chen, B.; Martin, M.G.; Siepmann, J.I. *J. Phys. Chem. B* **1998**, *102*, 2578–2586.

[80] Chen, B.; Siepmann, J.I. *J. Phys. Chem. B* **1999**, *103*, 5370–5379.

[81] Dubbeldam, D.; Calero, S.; Vlugt, T.J.H.; Krishna, R.; Maesen, Th.L.M.; Smit, B. *J. Phys. Chem. B* **2004**, *108*, 12301–12313.

[82] Calero, S.; Dubbeldam, D.; Krishna, R.; Smit, B.; Vlugt, T.J.H.; Denayer, J.F.M.; Martens, J.A.; Maesen, Th.L.M. *J. Am. Chem. Soc.* **2004**, *126*, 11377–11386.

[83] Vlugt, T.J.H.; Zhu, W.; Kapteijn, F.; Moulijn, J.A.; Smit, B.; Krishna, R. *J. Am. Chem. Soc.* **1998**, *120*, 5599–5600.

[84] Vlugt, T.J.H.; Krishna, R.; Smit, B. *J. Phys. Chem. B* **1999**, *103*, 1102–1118.

[85] Ryckaert, J.P.; McDonald, I.R.; Klein, M.L. *Mol. Phys.* **1989**, *67*, 957–979.

[86] Bourasseau, E.; Ungerer, P.; Boutin, A. *J. Phys. Chem. B* **2002**, *106*, 5483–5491.

[87] Allen, M.P.; Tildesley, D.J., *Computer Simulation of Liquids* Clarendon Press; Oxford, 1987.

[88] Ewald, P.P. *Ann. Phys.* **1921**, *64*, 253–287.

[89] Wolf, D.; Keblinski, P.; Phillpot, S.R.; Eggebrecht, J. *J. Chem. Phys.* **1999**, *110*, 8254–8282.

[90] Metropolis, N.; Rosenbluth, A.W.; Rosenbluth, M.N.; Teller, A.N.; Teller, E. *J. Chem. Phys.* **1953**, *21*, 1087–1092.

[91] Metropolis, N. *Los Alamos Science* **1987**, *12*, 125–130.

[92] Landau, D.P.; Binder, K., *A Guide to Monte Carlo Simulations in Statistical Physics* Cambridge University Press; Cambridge, 2000.

[93] Doi, M.; Edwards, S.F., *The Theory of Polymer Dynamics* Clarendon Press; Oxford, 1986.

[94] Dunweg, B.; Grest, G.S.; Kremer, K., *Numerical Methods for Polymeric Systems* Springer; New York, 1998.

[95] Kremer, K.; Grest, G.S. *J. Chem. Phys.* **1990**, *92*, 5057.

[96] Rosenbluth, M.N.; Rosenbluth, A.W. *J. Chem. Phys.* **1955**, *23*, 356–359.

[97] Harris, J.; Rice, S.A. *J. Chem. Phys.* **1988**, *88*, 1298–1306.

[98] Frenkel, D.; Mooij, G.C.A.M.; Smit, B. *J. Phys.: Condens. Matter* **1992**, *4*, 3053–3076.

[99] Siepmann, J.I.; Frenkel, D. *Mol. Phys.* **1992**, *75*, 59–70.

[100] Consta, S.; Wilding, N.B.; Frenkel, D.; Alexandrowicz, Z. *J. Chem. Phys.* **1999**, *110*, 3220–3228.

[101] Consta, S.; Vlugt, T.J.H.; Wichers Hoeth, J.; Smit, B.; Frenkel, D. *Mol. Phys.* **1999**, *97*, 1243–1254.

[102] Houdayer, J. *J. Chem. Phys.* **2002**, *116*, 1783–1787.

[103] Vlugt, T.J.H.; Martin, M.G.; Smit, B.; Siepmann, J.I.; Krishna, R. *Mol. Phys.* **1998**, *94*, 727–733.

[104] Vlugt, T.J.H. *Mol. Sim.* **1999**, *23*, 63–78.

[105] Combe, N.; Vlugt, T.J.H.; Wolde, P.R.T.; Frenkel, D. *Mol. Phys.* **2003**, *101*, 1675–1682.

[106] Martin, M.G.; Siepmann, J.I. *J. Phys. Chem. B* **1999**, *103*, 4508–4517.

[107] Panagiotopoulos, A.Z. *Mol. Phys.* **1987**, *61*, 813–826.

[108] Panagiotopoulos, A.Z.; Quirke, N.; Stapleton, M.; Tildesley, D.J. *Mol. Phys.* **1988**, *63*, 527–545.

[109] Martin, M.G.; Siepmann, J.I. *J. Am. Chem. Soc.* **1997**, *119*, 8921-8924.

[110] Fichthorn, K.A.; Weinberg, W.H. *J. Phys. Chem.* **1991**, *95*, 1090–1096.

[111] Bortz, A.B.; Kalos, M.H.; Lebowitz, J.L. *J. Comput. Phys.* **1975**, *17*, 10–18.

[112] Rapaport, D.C., *The art of molecular dynamics simulation*, 2nd ed. Cambridge University Press; Cambridge, 2004.

[113] Goldstein, H., *Classical Mechanics*, 2nd ed. Addison-Wesley; Reading, 1980.

[114] Reichl, L.E., *A Modern Course in Statistical Physics* University of Texas Press; Austin, 1980.

[115] Dubbeldam, D.; Snurr, R.Q. *Mol. Sim.* **2007**, *33*, 305–325.

[116] Krishna, R.; van Baten, J.M. *Chem. Eng. Sci.* **2008**, *63*, 3120–3140.

[117] Dubbeldam, D.; Ford, D.C.; Ellis, D.E.; Snurr, R.Q. *Mol. Sim.* **2009**, doi:10.1080/08927020902818039.

[118] Tromp, M.; van Bokhoven, J.A.; Oostenbrink, M.T.G.; Bitter, J.H.; de Jong, K.P.; Koningsberger, D.C. *J. Catal.* **2000**, *190*, 209–214.

[119] Leia, G.D.; Carvilla, B.T.; Sachtler, W.M.H. *Appl. Catal. A-Gen.* **1996**, *142*, 347–359.

[120] Haag, W.O., in *Zeolites and Related Microporous Materials: State of the Art 1994*, Studies in Surface Science and Catalysis, edited by Weitkamp, J.; Karge, H.G.; Pfeifer, H.; Hölderich, W. Elsevier; Amsterdam, 1994, Vol. 84, pp. 1375–1394.

[121] Schlenker, J.L.; Pluth, J.J.; Smit, J.V. *Materials Research Bulletin* **1979**, *14*, 751.

[122] Choudhary, V.R.; Mayadevi, S.; Singh, A.P. *J. Chem. Soc. Faraday Trans.* **1995**, *91*, 2935–2944.

[123] Webster, C.E.; Cottone, A.; Drago, R.S. *J. Am. Chem. Soc.* **1999**, *121*, 12127–12139.

[124] Beerdsen, E.; Dubbeldam, D.; Smit, B.; Vlugt, T.J.H.; Calero, S. *J. Phys. Chem. B* **2003**, *107*, 12088–12096.

[125] Marie, O.; Massiani, P.; Thibault-Starzyk, F. *J. Phys. Chem. B* **2004**, *108*, 5073–5081.

[126] Alberti, A. *Zeolites* **1997**, *19*, 411–415.

[127] Niwa, M.; Suzuki, K.; Katada, N.; Kanougi, T.; Atoguchi, T. *J. Phys. Chem. B* **2005**, *109*, 18749–18757.

[128] Bevilacqua, M.; Busca, G. *Catalysis Communications* **2002**, *3*, 497–502.

[129] García-Pérez, E.; Dubbeldam, D.; Liu, B.; Smit, B.; Calero, S. *Angew. Chem. Int. Ed.* **2007**, *46*, 276–278.

[130] Liu, B.; García-Pérez, E.; Dubbeldam, D.; Smit, B.; Calero, S. *J. Phys. Chem. C* **2007**, *11*, 10419–10426.

[131] Leroy, F.; Jobic, H. *Chem. Phys. Lett.* **2005**, *406*, 375–380.

[132] Fan, J.F.; van de Graaf, B.; Xiao, H.M.; Njo, S.L. *J. Mole. Struc.* **1999**, *492*, 133–142.

[133] Fan, J.F.; Wang, Q.X.; Gong, X.D.; Xiao, H.M. *J. Mole. Struc.* **2003**, *638*, 129–134.

[134] Masuda, T.; Fujikata, Y.; Nishida, T.; Hashimoto, K. *Micropor. Mesopor. Mater.* **1998**, *23*, 157–167.

[135] Demuth, T.; Hafner, J.; Benco, L.; Toulhoat, H. *J. Phys. Chem. B* **2000**, *104*, 4593–4607.

[136] Macedonia, M.D.; Moore, D.D.; Maginn, E.J.; Olken, M.M. *Langmuir* **2000**, *16*, 3823–3834.

[137] Siepmann, J.I., in *Computer simulation of biomolecular systems: theoretical and experimental applications*, edited by van Gunsteren, W.F.; Weiner, P.K.; Wilkinson, A.J. Escom Science Publisher; Leiden, 1993, pp. 249–264.

[138] Smit, B. *Mol. Phys.* **1995**, *85*, 153–172.

[139] Swope, W.C.; Andersen, H.C.; Berens, P.H.; Wilson, K.R. *J. Chem. Phys.* **1982**, *76*, 637–649.

[140] Rouquerol, J.; Avnir, D.; Fairbridge, C.W.; Everett, D.H.; Haynes, J.H.; Pernicone, N.; Ramsay, J.D.F.; Sing, K.S.W.; Unger, K.K. *Pure Appl. Chem.* **1994**, *66*, 1739.

[141] Ban, S.; Vlugt, T.J.H. *Mol. Sim.* **2009**, doi: 10.1080/08927020802660614.

[142] Smit, B.; den Ouden, C.J.J. *J. Phys. Chem.* **1988**, *92*, 7169–7171.

[143] Devautour, S.; Adboulaye, A.; Giuntini, J.C.; Henn, F. *J. Phys. Chem. B* **2001**, *105*, 9298–9301.

[144] Pamba, M.; Maurin, G.; Devautour, S.; Vanderschueren, J.; Giuntini, J.C.; Renzo, F.D.; Hamidi, F. *Phys. Chem. Chem. Phys.* **2000**, *2*, 2027–2031.

[145] Coughlan, B.; Caroll, W.M.; Mcann, W.A. *J. Chem. Soc. Faraday Trans.* **1977**, *73*, 1612.

[146] Tyburce, B.; Kappenstein, C.; Cartraud, P.; Garnier, E. *J. Chem. Soc. Faraday Trans.* **1991**, *87*, 2849–2853.

[147] Mortier, W.J., *Compilation of Extraframework Sites in Zeolites* Butterworth; Guildford, 1982.

[148] Nesterenko, N.S.; Thibault-Starzyk, F.; Montouillout, V.; Yuschenko, V.V.; Fernandez, C.; Gilson, J.P.; Fajula, F.; Ivanova, I.I. *Micro. Meso. Mater.* **2004**, *71*, 157–166.

[149] Katada, N.; Takeguchi, T.; Suzuki, T.; Fukushima, T.; Inagaki, K.; Tokunaga, S.; Shimada, H.; Sato, K.; Oumi, Y.; Sano, T.; Segawa, K.; Nakai, K.; Shoji, H.; Wu, P.; Tatsumi, T.; Komatsu, T.; Masuda, T.; Domen, K.; Yoda, E.; Kondo, J.N.; Okuhara, T.; Kageyama, Y.; Niwa, M.; Ogura, M.; Matsukata, M.; Kikuchi, E.; Okazaki, N.; Takahashi, M.; Tada, A.; Tawada, S.; Kubota, Y.; Sugi, Y.; Higashio, Y.; Kamada, M.; Kioka, Y.; Yamamoto, K.; Shouji, T.; Arima, Y.; Okamoto, Y.; Matsumoto, H. *Appl. Catal. A-Gen.* **2005**, *283*, 63–74.

[150] Bezus, A.G.; Kiselev, A.V.; Lopatkin, A.A.; Du, P.Q. *J. Chem. Soc. Faraday Trans.* **1978**, *74*, 367–379.

[151] Snurr, R.Q.; Bell, A.T.; Theodorou, D.R. *J. Phys. Chem.* **1993**, *97*, 13742–13752.

[152] Smit, B.; Maesen, Th.L.M. *Nature* **1995**, *374*, 42–44.

[153] Maginn, E.J.; Bell, A.T.; Theodorou, D.N. *J. Phys. Chem.* **1995**, *99*, 2057–2079.

[154] Macedonia, M.D.; Maginn, E.J. *Mol. Phys.* **1999**, *96*, 1375–1390.

[155] Fuchs, A.H.; Cheetham, A.K. *J. Phys. Chem. B* **2001**, *105*, 7375–7383.

[156] Pascual, P.; Ungerer, P.; Tavitian, B.; Pernot, P.; Boutin, A. *Phys. Chem. Chem. Phys.* **2003**, *5*, 3684–3693.

[157] Dubbeldam, D.; Calero, S.; Vlugt, T.J.H.; Krishna, R.; Maesen, Th.L.M.; Beerdsen, E.; Smit, B. *Phys. Rev. Lett.* **2004**, *93*, 088302.

[158] Liu, B.; Smit, B.; Calero, S. *J. Phys. Chem. B* **2006**, *110*, 20166–20171.

[159] Fennell, C.J.; Gezelter, J.D. *J. Chem. Phys.* **2006**, *124*, 234104.

[160] García-Pérez, E.; Dubbeldam, D.; Maesen, Th.L.M.; Calero, S. *J. Phys. Chem. B* **2006**, *110*, 23968–23976.

[161] García-Pérez, E.; Dubbeldam, D.; Liu, B.; Smit, B.; Calero, S. *Angew. Chem. Int. Ed.* **2006**, *45*, 276-278.

[162] Liu, B.; García-Pérez, E.; Dubbeldam, D.; Smit, B.; Calero, S. *J. Phys. Chem. C* **2007**, *111*, 10419–10426.

[163] Wood, G.B.; Panagiotopoulos, A.Z.; Rowlinson, J.S. *Mol. Phys.* **1988**, *63*, 49–63.

[164] Dunne, J. A.; Mariwala, R.; Rao, M.; Sircar, S.; Gorte, R. J.; Myers, A. L. *Langmuir* **1996**, *12*, 5888–5895.

[165] Smit, B.; Siepmann, J.I. *J. Phys. Chem.* **1994**, *98*, 8442–8452.

[166] Karavias, F.; Myers, A.L. *Langmuir* **1991**, *7*, 3118–3126.

[167] Widom, B. *J. Chem. Phys.* **1963**, *39*, 2802–2812.

[168] de Pablo, J.J.; Laso, M.; Suter, U.W. *J. Chem. Phys.* **1992**, *96*, 6157–6162.

[169] Press, W.H.; Flannery, B.P.; Teukolsky, S.A.; Vetterling, W.T., *Numerical Recipes: The art of scientific computing* Cambridge University Press; Cambridge, 1986.

[170] Pluth, J.J.; Smith, J.V. *J. Am. Chem. Soc.* **1980**, *102*, 4704-4708.

[171] Patra, M.; Karttunen, M.; Hyvönen, M.T.; Falck, E.; Lindqvist, P.; Vattulainen, I. *Biophys. J.* **2003**, *84*, 3636–3645.

[172] Patra, M.; Karttunen, M.; Hyvönen, M.T.; Falck, E.; Vattulainen, I. *J. Phys. Chem. B* **2004**, *108*, 4485–4494.

[173] Demontis, P.; Spanu, S.; Suffritti, G.B. *J. Chem. Phys.* **2001**, *114*, 7980–7988.

[174] Zahn, D.; Schilling, B.; Kast, S.M. *J. Phys. Chem. B* **2002**, *106*, 10725–10732.

[175] Avendano, C.; Gil-Villegas, A. *Mol. Phys.* **2006**, *104*, 1475–1486.

[176] García-Pérez, E.; Parra, J.B.; Ania, C.O.; García-Sánchez, A.; van Baten, J.M.; Krishna, R.; Dubbeldam, D.; Calero, S. *Adsorption* **2007**, *13*, 469–476.

[177] Martin, M.G.; Thompson, A.P.; Nenoff, T.N. *J. Chem. Phys.* **2001**, *114*, 7174–7181.

[178] de Jong, K.P.; Mesters, C.M.A.M.; Peferoen, D.G.R.; Brugge, P.T.M.; de Groot, C. *Chem. Eng. Sci.* **1996**, *51*, 2053–2060.

[179] Stach, H.; Lohse, U.; Thamm, H.; Schirmer, W. *Zeolites* **1986**, *6*, 74–90.

[180] Sun, M.S.; Talu, O.; Shah, D.B. *J. Phys. Chem.* **1996**, *100*, 17276–17280.

[181] Zhu, W.; van de Graaf, J.M.; van den Broeke, L.J.P.; Kapteijn, F.; Moulijn, J.A. *Ind. Eng. Chem. Res.* **1998**, *37*, 1934–1942.

[182] Arik, I.C.; Denayer, J.F.M.; Baron, G.V. *Micropor. Mesopor. Mater.* **2003**, *60*, 111-114.

[183] van Donk, S.; Bitter, J.H.; Verberckmoes, A.; Versluis-Helder, M.; Broersma, A.; de Jong, K.P. *Angew. Chem. Int. Ed.* **2005**, *44*, 1360–1364.

[184] Krishna, R.; Paschek, D. *Phys. Chem. Chem. Phys.* **2001**, *3*, 453–462.

[185] Krishna, R.; Smit, B.; Calero, S. *Chem. Soc. Rev.* **2002**, *31*, 185–194.

[186] Jakobtorweihen, S.; Hansen, N.; Keil, F.J. *Molec. Phys.* **2005**, *103*, 471–489.

[187] Macedonia, M.D.; Maginn, E.J. *Fluid Phase Equilibria* **1999**, *160*, 19–27.

[188] Pascual, P.; Ungerer, P.; Tavitian, B.; Boutin, A. *J. Phys. Chem. B* **2004**, *108*, 393–398.

[189] Jorgensen, W.L.; Severance, D.L. *J. Am. Chem. Soc.* **1990**, *112*, 4768–4774.

[190] Chempath, S.; Snurr, R.Q.; Low, J.J. *AIChE Journal* **2004**, *50*, 463–469.

[191] Yue, X.P.; Yang, X.N. *Langmuir* **2006**, *22*, 3138–3147.

[192] Zeng, Y.P.; Ju, S.G.; Xing, W.H.; Chen, C.L. *Ind. Eng. Chem. Res.* **2007**, *46*, 242–248.

[193] Baker, C.M.; Grant, G.H. *Jour. Chem. theo. compu.* **2006**, *2*, 947–955.

[194] Zhao, X.S.; Chen, B.; Karaborni, S.; Siepmann, J.I. *J. Phys. Chem. B* **2005**, *109*, 5368–5374.

[195] Janda, K.C. *J. Chem. Phys.* **1975**, *63*, 1419.

[196] Steed, J.M. *J. Chem. Phys.* **1979**, *70*, 4940.

[197] Arunan, E.; Gutowsky, H.S. *J. Chem. Phys.* **1993**, *98*, 4294–4296.

[198] Wick, C.D.; Siepmann, J.I.; Klotz, W.L.; Schure, M.R. *Journal of Chromatography A* **2002**, *954*, 181–190.

[199] van Koningsveld, H.; Tuinstra, F.; van Bekkum, H.; Jansen, J.C. *Acta Cryst. B* **1989**, *45*, 423–431.

[200] Meier, W.M.; Olson, D.H.; Baerlocher, Ch., *Atlas of Zeolite Structure Types*, 4th ed. Elsevier; Amsterdam, 1996.

[201] Smit, B. *J. Phys. Chem.* **1995**, *99*, 5597–5603.

[202] Jorgensen, W.L.; Madura, J.D.; Swenson, C.J. *J. Am. Chem. Soc.* **1984**, *106*, 6638–6646.

[203] Chen, D.; Rebo, H.P.; Moljord, K.; Holmen, A. *Chem. Eng. Sci.* **1996**, *51*, 2687–2692.

[204] Peng, J.; Ban, H.Y.; Zhang, X.T.; Song, L.J.; Sun, Z.L. *Chem. Phys. Lett.* **2005**, *401*, 94–98.

[205] Thamm, H.; Stach, H.; Berezin, G.I. *Z. Chem.* **1984**, *24*, 420.

[206] Wu, P.D.; Debebe, A; Ma, Y.H. *Zeolite* **1983**, *3*, 118.

[207] Song, L.; Sun, Z.L.; Ban, H.Y.; Dai, M.; Rees, L.V.C. *Adsorption* **2005**, *11*, 325–339.

[208] Jentys, A.; Mukti, R.R.; Tanaka, H.; Lercher, J.A. *Micropor. Mesopor. Mater.* **2006**, *90*, 284–292.

[209] Lee, C.K.; Chiang, A.S.T.; Wu, F.Y. *AIChE Journal* **1992**, *38*, 128–135.

[210] Breck, D.W., *Zeolite Molecular Sieves* Wiley; New York, 1974.

[211] Talu, O.; Guo, C.J.; Hayhurst, D.T. *J. Phys. Chem.* **1989**, *93*, 7294–7298.

[212] Olsen, D.H.; Kokotailo, G.T.; Lawton, S.L.; Meier, W.M. *J. Phys. Chem.* **1981**, *85*, 2238–2243.

[213] Fyfe, C.A.; Feng, Y.; Grondey, H.; Kokotailo, G.T. *Chem. Soc. Chem. Commun.* **1990**, *18*, 1224–1226.

[214] Portsmouth, R.L.; Duer, M.J.; Gladden, L.F. *J. Chem. Soc. Faraday Trans.* **1995**, *93*, 559–567.

[215] Pope, C.G. *J. Phys. Chem.* **1986**, *90*, 835–837.

[216] Takahashi, A.; Yang, F.H.; Yang, R.T. *Ind. Eng. Chem. Res.* **2002**, *41*, 2487-2496.

[217] Myers, A.L.; Prausnitz, J.M. *AIChE Journal* **1965**, *11*, 121–130.

[218] Murthi, M.; Snurr, R.Q. *Langmuir* **2004**, *20*, 2489–2497.

[219] Cejka, J.; van Bekkum, H., *Zeolites and Ordered Mesoporous Materials: Progress and Prospects* Elsevier; Amsterdam, 2005.

[220] Cejka, J.; van Bekkum, H.; Corma, A.; Schüth, F. (editors), *Introduction to Zeolite Science and Practice 3th* Elsevier; Amsterdam, 2007.

[221] Lu, M.; Zhao, X.S., *Nanoporous Materials: Science and Engineering* Imperial College Press; London, 2004.

[222] Barrer, R.M., *Zeolites and Clay Minerals as Sorbents and Molecular Sieves* Academic Press; London, 1979.

[223] Bouyermaouen, A.; Bellemans, A. *J. Chem. Phys.* **1998**, *108*, 2170–2172.

[224] Demontis, P.; Fois, E.S.; Suffritti, G.B.; Quartieri, S. *J. Phys. Chem.* **1990**, *94*, 4329–4334.

[225] Gupta, S.; Nivarthi, S.S.; McCormick, A.V.; Danish, H.T. *Chem. Phys. Lett.* **1995**, *247*, 596–600.

[226] Harmandaris, V.A.; Angelopoulou, D.; Mavramtzas, V.G.; Theodorou, D.N. *J. Chem. Phys.* **2002**, *116*, 7656–7665.

[227] Hernández, E.; Catlow, C.R.A. *Proc. R. Soc. Lond. A* **1995**, *448*, 143–160.

[228] Kapteijn, F.; Moulijn, J.A.; Krishna, R. *Chem. Eng. Sci.* **2000**, *55*, 2923–2930.

[229] Kärger, J.; Vasenkov, S.; Auerbach, S., in *Handbook of zeolite catalysis and microporous materials*, edited by Auerbach, S.; Carrado, K.A.; Dutta, P.K. Marcel Dekker Inc.; New York, 2002.

[230] Beerdsen, E.; Dubbeldam, D.; Smit, B. *Phys. Rev. Lett.* **2006**, *96*, 044501.

[231] Sing, K.S.W. *Pure Appl. Chem.* **1985**, *57*, 603.

[232] Gelb, L.D.; Gubbins, K.E.; Radhakrishnan, R.; Sliwinska-Bartkowiak, *Rep. Porg. Phys.* **1999**, *62*, 1573.

[233] Evans, R.; Marconi, U.M.B.; Tarazona, P. *J. Chem. Soc. Faraday Trans.* **1986**, *82*, 1763.

[234] Tarazona, P.; Marconi, U.M.B.; Evans, R. *Mol. Phys.* **1987**, *60*, 573.

[235] Bock, H.; Gubbins, K.E.; Schoen, M. *J. Phys. Chem. C* **2007**, *111*, 15493–15504.

[236] Neimark, A.V. *Langmuir* **1995**, *11*, 4183.

[237] Ravikovitch, P.I.; Neimark, A.V. *Langmuir* **2002**, *18*, 1550.

[238] Coasne, B.; Jain, S.K.; Naamar, L.; Gubbins, K.E. *Phys. Rev. B* **2007**, *76*, 085416.

[239] Jain, S.K.; Gubbins, K.E.; Pellenq, R.J.M.; Pikunic, J.P. *Carbon* **2006**, *44*, 2445-2451.

[240] Gupta, A.; Clark, L.A.; Snurr, R.Q. *Langmuir* **2000**, *16*, 3910–3919.

[241] June, R.L.; Bell, A.T.; Theodorou, D.N. *J. Phys. Chem.* **1990**, *94*, 1508–1516.

[242] Bates, S.P.; van Well, W.J.M.; van Santen, R.A.; Smit, B. *J. Am. Chem. Soc.* **1996**, *118*, 6753–6759.

[243] Ustinov, E.A.; Do, D.D.; Fenelonov, V.B. *Carbon* **2006**, *44*, 653.

[244] Furmaniak, S.; Terzyk, A.P.; Gauden, P.A.; Lota, K.; Frackowiak, E.; Beguin, F.; Kowalczyk, P. *J. Coll. Inter. Sci.* **2008**, *317*, 442–448.

[245] Furmaniak, S.; Terzyk, A.P.; Jaroniec, M.; Gauden, P.A. *Micropor. Mesopor. Mater.* **2008**, *116*, 665–669.

[246] Sing, K.S.W.; Williams, R.T. *Part. Part. Syst. Charact.* **2004**, *21*, 71.

[247] García-Pérez, E.; Parra, J.B.; Ania, C.O.; Dubbeldam, D.; Vlugt, T.J.H.; Castillo, J.M.; Merkling, P.J.; Calero, S. *J. Phys. Chem. C* **2008**, *112*, 9976–9979.

[248] Hay, D.G.; Jaeger, H. *J. Chem. Soc. Chem. Commun.* **1984**, *21*, 1433–1433.

[249] Fyfe, C.A.; Strobl, H.; Kokotailo, G.T.; Kennedy, G.J.; Barlow, G.E. *J. Am. Chem. Soc.* **1988**, *110*, 3373.

[250] Wu, E.L.; Lawton, S.L.; Olson, D.H.; Rohrman, A.C.; Kokotailo, G.T. *J. Phys. Chem.* **1979**, *83*, 2777.

[251] Skoulidas, A.I.; Sholl, D.S. *J. Phys. Chem. B* **2002**, *106*, 5058–5067.

[252] Kiselev, A.V.; Lopatkin, A.A.; Shulga, A.A. *Zeolites* **1985**, *5*, 261–267.

[253] McEnaney, B *Carbon* **1987**, *25*, 69.

[254] Terzyk, A.P.; Furmaniak, S.; Gauden, P.A.; Harris, P.J.F.; Wloch, J.; Kowalczyk, P. *J. Phys.: Cond. Matt.* **2007**, *19*, 406208.

[255] Terzyk, A.P.; Furmaniak, S.; Harris, P.J.F.; Gauden, P.A.; Woch, J.; Kowalczyk, P.; Rychlicki, G. *Phys. Chem. Chem. Phys.* **2007**, *9*, 5919–5927.

[256] Do, D.D.; Do, H.D. *Adsorp. Sci. Tech.* **2003**, *21*, 389–423.

[257] Maris, T.; Vlugt, T.J.H.; Smit, B. *J. Phys. Chem. B* **1998**, *102*, 7183–7189.

[258] Meier, W.M.Z. *Z. Kristallogr.* **1961**, *115*, 439–450.

[259] Davis, M.E. *Nature* **2002**, *417*, 813–821.

[260] Tao, Y.; Kanoh, H.; Abrams, L.; Kaneko, K. *Chem. Rev.* **2006**, *106*, 896–910.

[261] Egeblad, K.; Christensen, C.H.; Kustova, M.; Christensen, C.H. *Chem. Mater.* **2008**, *20*, 946–960.

[262] Pérez-Ramírez, J.; Christensen, C.H.; Egeblad, K.; Christensen, C.H.; Groen, J.C. *Chem. Soc. Rev.* **2008**, *37*, 2530–2542.

[263] Choi, M.; Cho, H.S.; Srivastava, R.; Venkatesan, C.; Choi, D.; Ryoo, R. *Nature Materials* **2006**, *5*, 718–723.

[264] Schmidt, I.; Boisen, A.; Gustavsson, E.; Stahl, K.; Pehrson, S.; Dahl, S.; Carlsson, A.; Jacobsen, C.J.H. *Chem. Mater.* **2001**, *13*, 4416–4418.

[265] Jacobsen, C.J.H.; Madsen, C.; Houzvicka, J.; Schmidt, I.; Carlsson, A. *J. Am. Chem. Soc.* **2000**, *122*, 7116-7117.

[266] Tao, Y.; Kanoh, H.; Kaneko, K. *J. Am. Chem. Soc.* **2003**, *125*, 6044–6045.

[267] Groen, J.C.; Moulijn, J.A.; Pérez-Ramírez, J. *J. Mater. Chem.* **2006**, *16*, 2121–2131.

[268] Ogura, M.; Hinomiya, S.; Tateno, J.; Nara, Y.; Kikuchi, E.; Matsukata, M. *Chem. Lett.* **2008**, *8*, 882–883.

[269] Goovaerts, F.; Vansant, E.F.; Philippaerts, J.; Hulsters, P.D.; Gelan, J. *J. Chem. Soc. Faraday Trans.* **1989**, *85*, 3675–3685.

[270] Lin, F.N. and Davis, E.D., US patent 6140547, 2000.

[271] Chung, K.H. *Micropor. Mesopor. Mater.* **2008**, *111*, 544–550.

[272] Hunger, B.; Heuchel, M.; Clark, L.A.; Snurr, R.Q. *J. Phys. Chem. B* **2002**, *106*, 3882–3889.

[273] Chandra, A.K.; Goursot, A.; Fajula, F. *J. Mol. Catal. A: Chem.* **1997**, *119*, 45–50.

[274] Viswanadham, N.; Kumar, M. *Micropor. Mesopor. Mater.* **2006**, *92*, 31–37.

[275] Datong Ding, D.T.; Sun, P.C.; Jin, Q.H.; Li, B.H.; Wang, J.Z. *Zeolites* **1994**, *14*, 65–73.

[276] Treacy, M.M.J.; Higgins, J.B., *Collection of Simulated XRD Powder Patterns for Zeolites 7th* Elsevier Science; Amsterdam, 2007.

[277] Waasmaier, D.; Kirfel, A. *ACTA CRYST. A* **1995**, *51*, 416–431.

[278] Neimark, A.V.; Ravikovitch, P.I.; Grun, M.; Schuth, F.; Unger, K.K. *J. Colloid and Interface Sci.* **1998**, *207*, 159–169.

[279] Neimark, A.V.; Ravikovitch, P.I. *Micropor. Mesopor. Mater.* **2001**, *44-45*, 697–707.

[280] Ravikovitch, P.I.; Neimark, A.V. *Langmuir* **2002**, *18*, 1550–560.

[281] Smarsly, B.; Thommes, M.; Ravikovitch, P.R.; Neimark, A.V. *Adsorption* **2005**, *11*, 653–655.

[282] Thommes, M.; Smarsly, B.; Groenewolt, M.; Ravikovitch, P.I.; Neimark, A.V. *Langmuir* **2006**, *22*, 756–764.

[283] Koster, A.J.; Ziese, U.; Verkleij, A.J.; Janssen, A.H.; de Jong, K.P. *J. Phys. Chem. B* **2000**, *104*, 9368.

[284] Lu, B.W.; Kanai, T.; Oumi, Y.; Sano, T. **2007**, *14*, 89–96.

[285] Yuan, S.P.; Wang, J.G.; Li, Y.W.; Peng, S.Y. *J. Molec. Catal. A: Chemical* **2001**, *175*, 131–138.

[286] Oumi, Y.; Kanai, T.; Lu, B.W.; Sano, T. *Micropor. Mesopor. Mater.* **2007**, *101*, 127–133.

[287] Brändle, M.; Sauer, J. *J. Am. Chem. Soc.* **1998**, *120*, 1556–1570.

[288] Dempsey, E., *Molecular Sieves* Society of Chemical Industry; London, 1968, p. 293.

[289] Schröder, K.P.; Sauer, J *J. Phys. Chem.* **1993**, *97*, 6579.

[290] Limtrakul, J.; Yoinuan, J.; Tantanak, D. **1995**, *332*, 151–159.

[291] Limtrakul, J.; Tantanak, D. *Computers Phys.* **1996**, *208*, 331–340.

[292] Takaishi, T.; Kato, M.; Itabashi, K. *J. Phys. Chem.* **1994**, *98*, 5742–5743.

[293] Chatterjee, A.; Vlachos, D.G. *J. Computer-Aided Materials Design* **2007**, *14*, 253–308.

[294] Giudici, R.; Kouwenhoven, H.W.; Prins, R. *App. Catal. A-Gen.* **2000**, *203*, 101–110.

[295] Sawa, M.; Niwa, M.; Murakami, Y. *Zeolites* **1990**, *10*, 532.

[296] Bodart, P.; Nagy, J.B.; Debras, G.; Gabelica, Z.; Jacobs, P.A. *J. Phys. Chem.* **1986**, *90*, 5183–5190.

[297] Segawa, K.; Shimura, T. *App. Catal. A-Gen.* **2000**, *194-195*, 309–317.

[298] Stach, H.; Janchen, J.; Jerschkewitz, H.G.; Lohse, U.; Parlitz, B.; Zibrowius, B. *J. Phys. Chem.* **1992**, *96*, 8473–8479.

[299] Kato, M.; Itabashi, K.; Matsumoto, A.; Tsutsumi, K. *J. Phys. Chem. B* **2003**, *107*, 1788–1797.

[300] Barras, J.; Klinowshi, J.; McComb, D.W. *J. Chem. Soc. Faraday Trans.* **1994**, *90*, 3719–3723.

[301] Maurin, G.; Senet, P.; Devautour, S.; Henn, F.; van Doren, V.E.; Giuntin, J.C. *J. Phys. Chem. B* **2001**, *105*, 9157–9161.

[302] Koranyi, T.I.; Nagy, J.B. *J. Phys. Chem. B* **2005**, *109*, 15791–115797.

[303] Janssen, A.H.; Koster, A.J.; de Jong, K.P. *Angew. Chem. Int. Ed.* **2001**, *40*, 1102–1104.

[304] Wang, Q.L.; Giannetto, G.; Torrealba, M.; Perot, G.; Kappenstein, C.; Guisnet, M. *J. Catal.* **1991**, *130*, 459–470.

Summary

This thesis deals with the application of zeolite catalysis for the production of cumene via benzene alkylation with propene. In particular, the work will be focused on Mordenite (MOR-type zeolite).

The first step is to understand the effect of non-framework cations on the adsorption and diffusion of guest molecules adsorbed in MOR. In chapter 2, this effect is studied for alkanes in Na-MOR. The influence of the Al distribution is investigated. The simulations show that about one third of the framework Al is located in the four-membered rings of the side pockets, while the remaining Al is in the main channels of MOR. This distribution agrees well with other experimental and simulation results. Na-MOR models with various Si/Al ratios are used to compute the adsorption and diffusion behavior of alkanes. The simulations show a strong increase in the adsorption of alkanes for an increasing Na concentration. A direct correlation was found between the number of Al in the main channels and the quantities such as the adsorption isotherm, Henry coefficients, diffusion coefficient and micropore volume. For example, for a given Si/Al ratio, the adsorption isotherm corresponding to any Al M/S ratio (the ratio of Al in the main channel and in the side pocket), can be directly calculated using two pre-calculated reference isotherms that correspond to the maximum fraction of framework Al in the main channel and in the side pocket, respectively. We expect that this will also be applicable to molecules like benzene, propene and cumene. It is expected that the presence of non-framework cations (or the Brønsted acid sites) will significantly enhance the adsorption of benzene and propene, while the saturation loadings may decrease to some extent due to the occupancy of void micropore volume by non-framework cations. Diffusion of both benzene and propene will be slowed down as guest molecules strongly interact with Brønsted acid sites.

In chapter 3, a new method is introduced to compute the heat of adsorption for molecules in zeolite frameworks containing non-framework cations. This method is more accurate and efficient than either the conventional Widom's test particle method or the conventional method based on energy differences. In addition, we have shown that for studying adsorption in zeolites, the Ewald summation is superior to the recently proposed Wolf method both in accuracy and speed.

Apart from non-framework cations, the adsorption selectivity of benzene in benzene/propene mixtures is attributed to the micropore structure of zeolites. When the size of the micropores are close to the kinetic diameter of benzene, the heat of adsorption of benzene will be larger than that of propene. Therefore, benzene will be preferentially adsorbed in these zeolites. Zeolite catalysts suitable for benzene alkylation are MOR, Beta, zeolite Y and MCM-22. In order to understand the effect of the microporosity on the adsorption selectivity, in chapter 4 molecular simulations have been conducted for all-silica MOR, Beta, zeolite Y and MCM-22. The simulations show that for all four zeolites, the high selectivity towards benzene in equal molar benzene/propene mixtures can be obtained under various conditions. Simulation snapshots indicate that although the zeolites have different micropore topologies, the sizes of all the micropores are close to the kinetic diameter of benzene. In this way, a high adsorption selectivity of benzene is guaranteed. Therefore, potential zeolite catalysts for benzene alkylation need to have micropores of similar sizes as benzene.

Dealumination is an important treatment to improve the catalytic performance of H-MOR. As the dimensions of the zeolite micropores are the crucial factor for the high selectivity of benzene, the change of the microporosity during dealumination is a crucial issue. In chapter 5, a simulation method is developed to characterize the zeolite porosity in terms of the pore size distribution, the pore volume and the pore topology. This method is able to provide us with the high-resolution pore size distribution. In chapter 6 the dealumination process is modeled using Kinetic Monte Carlo simulations. The essential reactions of dealumination are identified as the removal of framework Al atoms and the migration of Si atoms, and the self-healing of the silanol vacancies. This

simulation scheme is justified by comparing to different experiments such as ^{29}Si NMR, XRD, N_2 physisorption and Non Local Density Function Theory (NLDFT) analysis using experimental Ar adsorption isotherms. The simulations indicate that the framework Al is extracted from the four-membered rings of the side pockets and the internal surface of the main channels. The void volumes of both regions can thus merge together to form large secondary pores. The size of the secondary pores is slightly larger than that of the main channels. However, the opening of the side pocket only take place locally, and they cannot form interconnected side channels for the transport of propene. In other words, the main channels are still separated by the eight-membered channels without interconnection. This observation conflicts with the concept of molecular traffic control postulated earlier.

MOR is a special zeolite compared to others such as the MFI-type zeolite. For instance, the synthesis of MOR requires a high Al content. By comparing to siliceous zeolites, the reason for this may be that MOR precursors can only be well-connected by the stabilization of Al atoms during the nucleation process, leading to a favorable Al-O-Si-O-Al linkage in the four-membered rings. Low Al concentrations during synthesis may cause a large fraction of stacking faults domains formed in MOR frameworks. These domains are constructed by MOR unit cells with mismatched four-membered rings.

Accordingly, the often observed disordered structure of the stacking faults is caused by the shift of MOR unit cells by half a unit cell along the z crystallographic axis. The stacking fault domains will be transformed into mesopores during dealumination. Based on the knowledge of the adsorption, diffusion and reaction of benzene and propene in MOR, several criteria can be proposed for the potential candidates for benzene alkylation:

- The zeolite framework should at least have one type of micropores of size $6 \sim 8$ Å, which matches the kinetic diameter of benzene or cumeme. Micropores larger than 8 Å may have a lower adsorption selectivity for benzene and cumene. Zeolites with a multi dimensional pore structure may also be suitable for benzene alkylation.

- The zeolite framework should have a low Al content, especially in four-membered rings. In this way, the zeolite is supposed to have a high siliceous structure with negligible crystalline impurities. In this case, blocking effects are minimized.

- The zeolite should have a small crystal size or it could be modified into small crystals without damaging the micropores. A high surface area is crucial for the accessibility of zeolites as well as the diffusivity of guest molecules.

Using the the IZA database of zeolite structures, another possible zeolite catalyst could be the MTW-type framework. ZSM-12 (MTW-type) has a one-dimensional structure consisting of straight channels of 6 Å. Since the secondary building units of ZSM-12 do not need a high Al composition for nucleation, a high siliceous structure can be synthesized easily without much crystalline impurities. In this way, aromatics are able to diffuse freely in the channels of ZSM-12. Compared to MOR, the narrow channels in ZSM-12 may suppress the formation of side products like multiple alkylated benzene. Compared to zeolite Beta which has been widely commercialized for cumene production, the quality of the final product is also expected to be high as ZSM-12 has an one-dimensional channel system without intersections which is actually present in zeolite Beta. Therefore, it is reasonable to speculate that ZSM-12 has a larger probability to lower the feed benzene/propene ratio than zeolite Beta and MOR. The additional effort can be made to enlarge the surface area of ZSM-12 by either synthesis or treatment such as acid leaching and base leaching.

Samenvatting

Dit proefschrift gaat over de toepassing van zeoliet katalyse voor de synthese van cumeen door middel van de alkylatie van benzeen met propeen. In het bijzonder wordt de toepassing van het zeoliet Mordeniet (*framework type*: MOR) onderzocht.

De eerste stap hiervoor is het begrijpen van het effect van *non-framework* kationen op de adsorptie en diffusie van geadsorbeerde moleculen in MOR. In hoofdstuk 2 wordt dit effect bestudeerd voor alkanen die geadsorbeerd zijn in Na-MOR. In dit hoofdstuk is het effect van de distributie van *framework* Al atomen onderzocht. Computer simulaties laten zien dat ongeveer één derde van de *framework* Al atomen zich bevinden in de zogenaamde *4-membered rings* van de *side-pockets*. De resterende Al atomen bevinden zich in de zogenaamde *main channels*. Deze distributie is in overeenstemming met andere simulaties en experimenten. Het adsorptie- en diffusiegedrag van alkanen is onderzocht voor Na-MOR structuren met verschillende Si/Al verhoudingen. De simulaties laten zien dat de adsorptie van alkanen sterk toeneemt voor een toenemende Al concentratie. Het aantal Al atomen in de *main channels* is direct gecorreleerd aan grootheden zoals de adsorptie isotherm, de Henry coëfficiënt, de diffusie coëfficiënt en het volume van de microporiën. Voor een gegeven Si/Al verhouding kan de adsorptie isotherm worden voorspeld voor elke willekeurige verhouding van het aantal Al in de *main channel* en het aantal Al in de *side pocket* (de zogenaamde M/S verhouding), uitgaande van twee gegeven referentie isothermen met een maximale Al belading in de *main channels* en *side pockets* respectievelijk. We verwachten dat dit ook toepasbaar is voor moleculen zoals benzeen en cumeen. De aanwezigheid van *non-framework* kationen (of Brønsted zure sites) resulteert in een toename van de adsorptie van moleculen. De maximale belading zal enigsinds afnemen door het ingenomen volume van de *non-framework* kationen. De diffusiecoëfficiënt van moleculen zoals benzeen en propeen zal dalen door de sterke interacties van deze moleculen met de kationen of Brønsted zure sites.

In hoofdstuk 3 wordt een nieuwe methode geïntroduceerd voor het uitrekenen van de adsorptiewarmte van geadsorbeerde moleculen in zeolieten met *non-framework* kationen. Deze methode is veel nauwkeuriger en efficiënter dat de conventionele *test-particle* methode van Widom en de conventionele methode gebaseerd op energieverschillen. Daarnaast laten we zien dat de Ewald sommatie vergeleken met de zogenaamde Wolf-methode superieur is voor de studie van het gedrag van geadsorbeerde polaire moleculen in zeolieten.

De adsorptieselectiviteit van benzeen in mengsels van benzeen en propeen kan worden toegeschreven aan de microporiën van het zeoliet. Als de grootte van de microporiën van het zeoliet ongeveer even groot zijn als de kinetische diameter van benzeen, zal de adsorptiewarmte van benzeen veel groter zijn dan die van propeen. Hierdoor zal benzeen bij voorkeur worden geadsorbeerd. Geschikte zeoliet katalysatoren voor de alkylering van benzeen zijn onder andere MOR, Beta, zeoliet Y en MCM-22. Om de invloed van de microporiën op de adsorptie selectiviteit te onderzoeken hebben we het adsorptiegedrag van benzeen en propeen onderzocht in bovengenoemde zeolieten. De simulaties laten zien dat voor al deze zeolieten een hoge selectiviteit voor benzeen kan worden bereikt. Snapshots van de simulaties laten zien dat ondanks de verschillen in topologie voor deze zeolieten de grootte van de microporiën steeds ongeveer even groot is als de grootte van een benzeen molecuul. Hierdoor wordt altijd een hoge adsorptie selectiviteit verkregen. Potentiële zeoliet katalysatoren voor de alkylering van benzeen dienen dus microporiën te hebben die ongeveer even groot zijn als een benzeen molecuul.

Dealuminering is belangrijke methode om de katalytische eigenschappen van een H-MOR zeoliet te verbeteren. Omdat de grootte van de microporiën van groot belang is voor de adsorptie van benzeen en propeen, is het belangrijk om de weten hoe de structuur van de microporiën verandert door dealuminering. In hoofdstuk 5 wordt een methode gepresenteerd om de porositeit

van een zeolietstructuur te karakteriseren door middel van de porie grootte verdeling en het porie volume. Hierdoor kunnen porie grootte verdelingen met een zeer hoge resolutie worden verkregen. In hoofdstuk 6 worden Kinetische Monte Carlo (KMC) simulaties gebruikt om de dealuminering te modelleren. De essentiële reacties tijdens dealuminering zijn: het verwijderen van *framework* Al atomen, en de *self-healing* van silanol groepen. Deze simulaties worden gevalideerd door een aantal experimentele technieken: ^{29}Si NMR, XRD, N_2 fysisorptie en Non Local Density Functional Theory (NLDFT) analyse van gemeten Ar fysisorptie experimenten. De simulaties laten zien dat *framework* Al uit de *side pockets* en *main channels* verwijderd wordt. Het vrije volume dat hierdoor ontstaat resulteert in een tweede type poriën. Echter, de *side pockets* worden uitsluitend van één kant opengebroken zodat de verschillende *main channels* niet met elkaar verbonden worden. Dit is in tegenspraak met het eerder gepostuleerde *molecular traffic control* mechanisme.

Vergeleken met andere zeolietstructuren is MOR een speciaal zeoliet. Bijvoorbeeld, bij de synthese van MOR is een hoge Al concentratie cruciaal, dit in tegenstelling tot bijvoorbeeld MFI. Een reden hiervoor kan zijn dat dit noodzakelijk is voor het onstaan van kleine MOR kernen die later uitgroeien tot een MOR kristal. Hierdoor kan een gunstige Al-O-Si-O-Al sequentie ontstaan in de *4-membered rings* van MOR. Lage Al concentraties kunnen mogelijk resulteren in een grote fractie aan zogenaamde *stacking fault domains*. Deze domeinen ontstaat door een mismatch van de *4-membered rings* bij naburige MOR eenheidscellen.

De waargenomen structuur van deze *stacking faults* wordt veroorzaakt door een verplaatsing van een MOR eenheidscel ter grootte van een halve eenheidscel langs de kristallografische z richting. Tijdens dealuminering zullen de *stacking fault domains* worden omgevormd tot mesoporiën. Gebaseerd op kennis van adsorptie, diffusie en reactie van benzeen en propeen in MOR kunnen enkele criteria worden geformuleerd voor potentiële zeoliet katalysatoren voor de alkylatie van benzeen in MOR:

- Het zeoliet dient ten minste één type microporiën te hebben in grootte van $6 \sim 8$ Å. Dit is ongeveer gelijk aan de grootte van een benzeen molecuul. Grotere microporiën zullen een lagere adsorptie selectiviteit hebben voor benzeen en cumeen. Zeolieten met meer typen poriën zijn mogelijk ook geschikt voor de alkylering van benzeen.

- Het zeoliet dient een lage Al concentratie te hebben, met name in de *4-membered rings*. Hierdoor zal het zeoliet relatief weinig onzuiverheden hebben, waardoor *blocking effects* geen rol spelen.

- De zeoliet kristallen dienen klein te zijn. Een groot oppervlak is belangrijk voor de toegankelijkheid van zeolieten.

Op basis hiervan en het raadplagen van de IZA database speculeren we dat MTW (ZSM-12) zeoliet een mogelijke kandidaat zou kunnen zijn. Dit zeoliet heeft een één dimensionale structuur bestaande uit rechte kanalen met een diameter van 6 Å. Omdat er voor de synthese van ZSM-12 geen hoge Al concentratie vereist is, is het eenvoudig om een kristal zonder veel defecten te synthetiseren. In vergelijking tot MOR verwachten we dat MTW bepaalde nevenreacties (zoals meervoudige alkylatie) zal onderdrukken. In tegenstelling tot de bekende katalysator zeoliet Beta bevat MTW slecht één dimensionale kanalen. Daarom verwachten we dat MTW te potentie heeft om in het uiteindelijke proces de benzeen/propeen verhouding in de voeding van de reactor zo dicht mogelijk tot de waarde 1 te brengen. Verdere studies kunnen erop gericht zijn om de toegankelijkheid van MTW voor kleine moleculen te optimaliseren.

Curriculum vitae

Name: Shuai Ban
Birth: 29 June 1980 in Henan, China

Education:

1993 - 1999 7th Middle school, Zhengzhou, China

1999 - 2003 Bachelor of Engineering
Beijing University of Aeronautics and Astronautics, Beijing, China
Major Flight Vehicle Design and Applied Mechanics

2003 - 2005 Master of Science
Royal Institute of Technology, Stockholm, Sweden
Major Applied mathematics and scientific computing
Project Pattern storage and recognition using ferrofluids

2005 - 2009 PhD Research
Utrecht University, Utrecht, Netherlands
Major Computational chemistry of catalysis
Project Process intensification in alkylation processes using zeolite catalysts with molecular traffic control
Supervisors Prof. dr. J.P.J.M. van der Eerden
Prof. dr. ir. K.P. de Jong
Dr. ir. T.J.H. Vlugt

Acknowledgements

First of all, I would like to thank my thesis supervisors Prof. dr. J.P.J.M. van der Eerden, Prof. dr. ir. K.P. de Jong and Dr. ir. T.J.H. Vlugt for their contributions to this thesis. Here I would like to specially thank Dr. ir. T.J.H. Vlugt for his hospitable and attentive supervision. I acknowledge ASPECT program, NWO for providing the funding of my PhD project.

Second, I would like to thank my wife Lin Shang who always support and encourage me during my stay in Netherlands. Without you, it is almost impossible for me to complete my PhD in four years. I would also like to thank my parents and parent-in-law for their considerate care when I am in China as well as in Netherlands.

Third, I would like to thank all people with whom I have collaborated: my project partners Dr. Petra de Jongn, Adri van Laak and Dr. Lei zhang who have provided me with many valuable experimental results and fruitful discussions. Prof. Freek Kapteijn and Johan van den Bergh for the joint research of molecular diffusion in zeolites. People from chemical industry including Garry Meima from Dow Chemical, Marcel Janssen from ExxonMobil Chemical and John Casci from Johnson Matthey. Last but not least, all my colleges from simulation groups in Utrecht University and Technical University of Delft.